TECHNISCHE UNIVERSITÄT MÜNCHEN
Physik-Department
Institut für Theoretische Physik
Lehrstuhl Univ.-Prof. Dr. Peter Vogl

Efficient calculation of dissipative quantum transport properties in semiconductor nanostructures

Peter Greck

Vollständiger Abdruck der von der Fakultät für Physik der Technischen Universität München zur Erlangung des akademischen Grades eines

Doktors der Naturwissenschaften (Dr. rer. nat.)

genehmigten Dissertation.

Vorsitzender:	Univ.-Prof. Jonathan J. Finley, Ph. D
Prüfer der Dissertation	1. Univ.-Prof. Dr. Peter Vogl
	2. Univ.-Prof. Paolo Lugli, Ph. D

Die Dissertation wurde am 06.09.2012 bei der Technischen Universität München eingereicht und durch die Fakultät für Physik am 26.11.2012 angenommen.

Algebra is a wonderful invention.
It enables fools to do physics,
without understanding.

— Lewis C. Epstein

It is well known that a software system
cannot be made reliable by testing.

— Richard C. Linger

Nothing is as practical as a good theory.

— Germund Dahlquist

ABSTRACT

We present a novel quantum transport method that follows the non-equilibrium Green's function (NEGF) framework but side steps any self-consistent calculation of lesser self-energies by replacing them by a quasi-equilibrium expression. We termed this method the multi-scattering Büttiker–Probe (MSB) method. It generalizes the so-called Büttiker–Probe model but takes into account all relevant individual scattering mechanisms. It is orders of magnitude more efficient than a fully self-consistent non-equilibrium Green's function calculation for realistic devices, yet accurately reproduces the results of the latter method as well as experimental data. This method is fairly easy to implement and opens the path towards realistic three-dimensional quantum transport calculations.

In this work, we review the fundamentals of the non-equilibrium Green's function formalism for quantum transport calculations. Then, we introduce our novel MSB method after briefly reviewing the original Büttiker–Probe model. Finally, we compare the results of the MSB method to NEGF calculations as well as to experimental data. In particular, we calculate quantum transport properties of quantum cascade lasers in the terahertz (THz) and the mid-infrared (MIR) spectral domain.

With a device optimization algorithm based upon the MSB method, we propose a novel THz quantum cascade laser design. It uses a two-well period with alternating barrier heights and complete carrier thermalization for the majority of the carriers within each period. We predict THz laser operation for temperatures up to 250 K implying a new temperature record.

ZUSAMMENFASSUNG

Wir stellen eine neue Quantentransport-Methode vor, die grundsätzlich dem Konzept der Nicht-Gleichgewicht-Green-Funktionen folgt. Dabei werden jegliche selbstkonsistente Berechnungen der sogenannten Kleiner-Selbstenergien umgangen und durch Quasigleichgewichts-Ausdrücke ersetzt. Wir haben diese Methode Mehrfach-Streu-Büttiker–Probe (MSB) Methode genannt und sie verallgemeinert das sogenannte Büttiker–Probe-Modell, wobei jedoch alle relevanten Streumechanismen berücksichtigt werden. Die MSB-Methode ist um Größenordnungen effizienter als eine vollständig in sich konsistente Nicht-Gleichgewicht-Green-Funktions-Berechnung für realistische Bauteile. Die Ergebnisse der MSB-Methode stimmen jedoch sowohl mit Nicht-Gleichgewichts-Green-Funktions-Berechnungen als auch mit Experimenten überein. Die MSB-Methode ist einfach zu implementieren und öffnet den Weg in Richtung realistischer, dreidimensionaler Quantentransport-Berechnungen.

In dieser Arbeit geben wir die Grundzüge des Konzeptes der Nicht-Gleichgewicht-Green-Funktionen wieder. Nachdem wir dann das originale Büttiker–Probe-Modell vorgestellt haben, präsentieren wir unsere neue MSB-Methode. Danach vergleichen wir die Ergebnisse der MSB-Methode mit Nicht-Gleichgewicht-Green-Funktions-Rechnungen sowie mit Experimenten. Insbesondere berechnen wir Quantentransport-Eigenschaften von Quanten-Kaskaden-Lasern im Terahertz- und mittleren Infrarot-Bereich.

Mit der Hilfe eines Algorithmus zur Bauteiloptimierung schlagen wir einen neuartigen Terahertz-Quanten-Kaskaden-Laser vor. Er besteht aus zwei Quantentöpfen pro Periode, hat unterschiedliche Barrierenhöhen und thermalisiert die überwiegende Mehrheit der Ladungsträger in jeder Periode. Nach unseren Berechnungen funktioniert dieser neuartige Laser bis zu Temperaturen von 250 K, was ein neuer Temperaturrekord wäre.

CONTENTS

α, β	summation indexes are typeset in Greek letters
A	spectral function, Fröhlich coupling constant
AP	acoustic phonon
B	scattering potential
C	time contour, set of all nodes within the contact block
CBR	contact block reduction
δ	Dirac's delta distribution
D_{Ph}	phonon Green's function
ε_0	electric vacuum permittivity, electric constant ($8.854\ \mathrm{CV^{-1}m^{-1}}$)
ε_s	relative electric permittivity at the low frequency limit
ε_∞	relative electric permittivity at the high frequency limit
η	phenomenological scattering parameter
e	elementary charge (1.602×10^{-19} C)
E_{AP}	energy of acoustic phonons
EMA	effective mass approximation
E_{OP}	energy of optical phonons
f	distribution function
$\mathcal{F}_j$	Fermi–Dirac integral of the order j
FDM	finite differences method
FEM	finite elements method
FIR	far infrared
G	Green's function
$\mathcal{H}$	Heisenberg picture
h	Planck's constant (4.135×10^{-15} eVs)
$\hbar$	Dirac's constant $\frac{h}{2\pi}$ (6.582×10^{-16} eVs)
I_{m}	momentum integral

IR	infrared
i	imaginary unit
j	current density
k_B	Boltzmann's constant (8.617×10^{-5} eV/K)
$k_\parallel$	in-plane wave vector, in-plane momentum
L	set of all leads
m_0	electron rest mass (9.109×10^{-31} kg)
MIR	mid-infrared
MSB	multi-scattering Büttiker–Probe method
n	carrier density
NEGF	non-equilibrium Green's function
OP	optical phonon
Φ	electrostatic Hartree potential
ϕ	spatial basis function
$\Psi_\mathcal{H}$	quantum field operator in the Heisenberg picture
P	set of all Büttiker–Probes
ω	frequency
QCL	quantum cascade laser
QDD	quantum drift–diffusion method
ρ	density of states
ρ_M	material density
$\mathcal{S}$	overlap matrix of basis functions
S	self-energy that describes the coupling to the leads
Σ	self-energy that describes scattering processes
σ	complex dynamical conductance
Θ	Heaviside's unit step function
$\mathcal{T}$	time-ordering operator
T	temperature, transmission function, transfer matrix
THz	terahertz
Tr	trace operator
δU	perturbation potential
V_D	scalar deformation potential
v_s	velocity of sound
W	coupling matrices between device and leads

INTRODUCTION

The general motivation for this work was the future design and fabrication of devices in the nanometer regime for which a detailed understanding of inelastic effects is crucial [Dan84; BK95]. Recently, a 22 nm transistor was presented and current research is exploring the scaling behaviors and limits of the next generation of even smaller transistors. Here, investigations aided by computational models, tools, and studies can support the understanding of nanoscale device physics. However, on this scale, a semi-classical or ballistic model is not sufficient to describe carrier dynamics neither qualitatively nor quantitatively. Nevertheless, the non-equilibrium Green's function (NEGF) formalism is a rigorous approach that captures the tight interplay between incoherent relaxation processes and quantum interference effects [Kub+09].

Unfortunately, the basic NEGF equations are complex, mathematically tough, and a quantitative implementation is still a highly challenging task, even with the recent advances of modern computer hardware [Zhe+06; Cau+11]. Furthermore, it is very difficult to develop approximations within the NEGF formalism which maintain charge and current conservation and obey Pauli's principle [KV11]. One example of such an approximation is the so-called contact block reduction (CBR) method that can be used to efficiently calculate quantum transport properties in the limit of ballistic transport [Mam+05].

In this work, we present a novel method to calculate stationary quantum transport properties that we term the multi-scattering Büttiker–Probe (MSB) model. It generalizes the so-called Büttiker–Probe model [But88b] and accounts for individual scattering mechanisms. Current conservation is ensured and the MSB method is orders of magnitude faster than the full NEGF approach. Additionally, the MSB method accurately reproduces the results of NEGF calculations and is consistent with experimental data. With this novel method it is possible to rapidly calculate observable quantities for realistic devices. Furthermore, it is feasible to sweep several device parameters like barrier thicknesses, alloy compositions, or doping concentrations to quickly find an optimized device design as we will demonstrate later for a novel THz quantum cascade laser (QCL) design in Chapter 9.

This thesis is organized in three parts. The first part covers the fundamentals of the non-equilibrium Green's function formalism. In Chapter 1 the Green's functions are defined and the stationary kinetic equations are derived. The choice of an appropriate basis representation is discussed and the relations to observables like carrier density, current density, and optical gain are presented. Finally, self-energies that describe carrier–phonon scattering processes are introduced and the effective mass approximation (EMA) is briefly reviewed. In Chapter 2 the boundary conditions for so-called open devices are discussed. In addition to the standard calculation we present an extended iterative solution that is exponentially faster than a straightforward iteration. The calculation of the electrostatic Hartree potential is discussed in Chapter 3. Here, the so-called predictor–corrector approach is presented for quantum transport calculations. In Chapter 4 we give an overview of the solution scheme of quantum transport calculations within the NEGF formalism. A flow chart illustrates the complex couplings of the involved equations. Finally, in Chapter 5 we present the so-called Büttiker–Probe model that serves as the basis for the novel MSB method. Here, we discuss the calculation of observable quantities that remain valid for the MSB model. Furthermore, we explain how current conservation is ensured and how the phenomenological scattering parameters can be related to the mean free path.

The second part of this thesis covers the novel multi-scattering Büttiker–Probe (MSB) model for quantum transport calculations that we have developed. In Chapter 6 we give a brief overview of the various existing methods of calculating quantum transport properties. We focus in particular on the efficiency of the individual methods in terms of computational costs and the timely calculation of transport properties. In Chapter 7 we present our novel MSB method. First, we derive the basic quantum transport equations within the MSB model. We discuss in detail the approximations to the scattering self-energies and their justifications. Afterwards, we introduce a novel type of Büttiker–Probes primarily for two-contact devices and we extend the predictor–corrector approach for the MSB method. Finally, we extend the MSB method for layered heterostructures to take full numerical advantage of the analytic k-space integration.

The third and final part covers the results and assessments of the MSB method. In Chapter 8 we apply the MSB method in the semi-classical limit and exemplarily calculate a resonant tunneling diode (RTD) as a prototypical quantum device. We also compare a three-dimensional calculation with a similar calculation for layered heterostructures. In Chapter 9 we calculate quantum cascade laser (QCL) devices with our novel MSB method and compare the results to NEGF calculations as well as experimental data. Finally, we propose a concrete THz QCL based on a two-well design with alternating barrier heights and complete carrier thermalization for the

majority of the carriers within each period. We predict THz laser operation for temperatures up to 250 K implying a new temperature record. Finally, in Chapter 10 we briefly summarize the achievements of this thesis.

Part I

NON-EQUILIBRIUM GREEN'S FUNCTION THEORY

1 FUNDAMENTALS

A detailed understanding of carrier dynamics is crucial for the design and improvement of modern semiconductor nano-devices. However, neither a classical or semi-classical nor a strictly coherent, ballistic quantum mechanical theory can capture the tight interplay between incoherent relaxation processes and quantum interference effects [Dan84; BK95; Kub+09].

A general and rigorous framework to capture all of these effects was developed in the 1960s by Schwinger [Sch61] and Keldysh [Kel65], and, independently, by Kadanoff and Baym [KB62]. Today, it is well established that this so-called non-equilibrium Green's function (NEGF) theory is among the most general schemes for the prediction of quantum transport properties [FJ92; Dat95; Lak+97; AG98; Wac02a]. It works within the effective mass approximation as well as within an atomistic tight-binding model, where it allows the inclusion of sophisticated band structure models. Furthermore, any type of scattering can be treated within the non-equilibrium Green's function formalism ranging from the simplest to the most advanced approximations. However, ballistic quantum transport is the most widespread from [AG98; Mar+07; Bir+09].

In this chapter, we briefly review the non-equilibrium Green's function formalism. We start with the definition of the Green's functions in the time domain and derive the equations of motion. Then, we discuss the transformation into a discrete basis, the stationary solution in the energy domain, and the calculation of observables such as carrier densities and current densities. Finally, we review the self-energies for carrier–carrier and carrier–phonon scattering.

1.1 DEFINITION

Calculating physical observables from a microscopic description of a system is a typical task in condensed matter physics. In this context various formulations of the Green's function theory exist, e. g. a zero temperature as well as a finite temperature formalism [KB62; HJ89; BF04]. In this work, we focus on a general non-equilibrium

finite temperature Green's function formalism which can also be applied in equilibrium as a limiting case. The following brief introduction to the non-equilibrium Green's functions formalism is based on the books by Hartmut Haug and Antti-Pekka Jauho [HJ89], David Ferry and Carlo Jacoboni [FJ92], and on the concise summary by Mathieu Luisier [Lui07].

The one-particle non-equilibrium Green's function G in the Heisenberg picture $\mathcal{H}$ is defined as

$$\begin{aligned} G(\mathbf{r},t,\mathbf{r}',t') &= -\frac{i}{\hbar}\left\langle \mathcal{T}\left\{\hat{\psi}_{\mathcal{H}}(\mathbf{r},t)\hat{\psi}^{\dagger}_{\mathcal{H}}(\mathbf{r}',t')\right\}\right\rangle \\ &= -\frac{i}{\hbar}\Bigg(\theta(t,t')\left\langle \hat{\psi}_{\mathcal{H}}(\mathbf{r},t)\hat{\psi}^{\dagger}_{\mathcal{H}}(\mathbf{r}',t')\right\rangle \\ &\qquad -\theta(t',t)\left\langle \hat{\psi}^{\dagger}_{\mathcal{H}}(\mathbf{r}',t')\hat{\psi}_{\mathcal{H}}(\mathbf{r},t)\right\rangle\Bigg), \end{aligned} \tag{1.1}$$

where $\hat{\psi}^{\dagger}_{\mathcal{H}}(\mathbf{r}',t')$ and $\hat{\psi}_{\mathcal{H}}(\mathbf{r},t)$ are quantum field operators. The operator $\hat{\psi}^{\dagger}_{\mathcal{H}}(\mathbf{r}',t')$ creates a particle at position $\mathbf{r}'$ and time t' whereas the operator $\hat{\psi}_{\mathcal{H}}(\mathbf{r},t)$ removes a particle at position $\mathbf{r}$ and time t. For fermionic particles they obey the usual anti-commutator relations

$$\begin{aligned} \left[\hat{\psi}_{\mathcal{H}}(\mathbf{r},t),\hat{\psi}^{\dagger}_{\mathcal{H}}(\mathbf{r}',t)\right]_{+} &= \delta(\mathbf{r}-\mathbf{r}'), \\ \left[\hat{\psi}_{\mathcal{H}}(\mathbf{r},t),\ \hat{\psi}_{\mathcal{H}}(\mathbf{r},t)\right]_{+} &= 0, \\ \left[\hat{\psi}^{\dagger}_{\mathcal{H}}(\mathbf{r},t),\ \hat{\psi}^{\dagger}_{\mathcal{H}}(\mathbf{r},t)\right]_{+} &= 0. \end{aligned}$$

Here, we restrict the Green's function G to spatial and time coordinates to keep the notation compact. However, the equations can easily be extended to other variables, e. g. spin, subband indexes, or atomic orbital indexes. To calculate the operator expectation values a general time contour C is introduced [Dan84] as depicted in Fig. 1.1. Note that all times on the contour C are real, i. e. $t,t' \in \mathbb{R}$, however an additional branch–label is attached to each time that uniquely assigns it to either the chronological branch C_c or the anti-chronological branch C_a. The operator $\mathcal{T}$ is the so-called time-ordering operator that reorders the operators along a contour C.

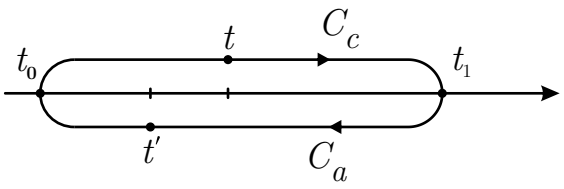

Figure 1.1: The time contour $C = C_c \cup C_a$ is the union of a chronological branch C_c from t_0 to t_1 and an anti-chronological branch C_a from t_1 to t_0. The two times t and t' are shown as example for the case where t' is later on the contour C but $t' < t$ holds. Note that the whole contour runs on the time axis. For clarity it is shown slightly away from the axis.

The function $\theta(t, t')$ is defined as

$$\theta(t,t') = \begin{cases} \Theta(t-t') & : t \text{ later on } C \text{ and } t > t' \text{ or} \\ & \quad t' \text{ later on } C \text{ and } t' > t \\ \Theta(t'-t) & : t \text{ later on } C \text{ and } t' > t \text{ or} \\ & \quad t' \text{ later on } C \text{ and } t > t' \end{cases},$$

where Θ is Heaviside's unit step function. Here, the expression "later on the contour C" can be illustrated as follows. Let the contour $C(s)$ be a parametrized curve that starts at time t_0 on the chronological branch C_c with $s = 0$. At the interconnect of the chronological and the anti-chronological branch at time t_1 in Fig. 1.1 the parameter equals $s = 0.5$. Finally, the contour C returns to the time t_0 on the anti-chronological branch C_a and the parameter equals $s = 1$. Thus, "t is later on the contour C" means $s(t) > s(t')$ which not necessarily means $t > t'$. The derivative of θ with respect to time t is given by

$$\frac{\mathrm{d}}{\mathrm{d}t}\theta(t,t') = -\frac{\mathrm{d}}{\mathrm{d}t'}\theta(t,t') = \vartheta(t,t') = \begin{cases} \delta(t'-t) & : t \text{ later on } C,\ t > t' \text{ or} \\ & \quad t' \text{ later on } C,\ t' > t \\ -\delta(t-t') & : t \text{ later on } C,\ t' > t \text{ or} \\ & \quad t' \text{ later on } C,\ t > t' \end{cases},$$

where δ is Dirac's δ-distribution.

The non-equilibrium Green's function $G(\mathbf{r}, t, \mathbf{r}', t')$ gives the correlation between the two positions $\mathbf{r}$ and $\mathbf{r}'$ and two times t and t'. If t is later on the contour C than

t', it describes the reaction to a particle that is created at position $\mathbf{r}'$ and time t' and annihilated at position $\mathbf{r}$ and time t. An analogous interpretation can be found if t' is later than t on the contour C.

The equations of motion of the non-equilibrium Green's function G describe its evolution in time. To derive these equations of motion, we start with the following derivative with respect to time t

$$\begin{aligned}
&\frac{\mathrm{d}}{\mathrm{d}t}\mathcal{T}\left\langle\hat{\psi}_{\mathcal{H}}(\mathbf{r},t)\hat{\psi}^{\dagger}_{\mathcal{H}}(\mathbf{r}',t')\right\rangle \\
&\quad=\mathcal{T}\left\langle\frac{\mathrm{d}}{\mathrm{d}t}\hat{\psi}_{\mathcal{H}}(\mathbf{r},t)\hat{\psi}^{\dagger}_{\mathcal{H}}(\mathbf{r}',t')\right\rangle+\vartheta(t,t')\left[\hat{\psi}_{\mathcal{H}}(\mathbf{r},t)\hat{\psi}^{\dagger}_{\mathcal{H}}(\mathbf{r}',t')\right]_{+} \\
&\quad=\mathcal{T}\left\langle\frac{\mathrm{d}}{\mathrm{d}t}\hat{\psi}_{\mathcal{H}}(\mathbf{r},t)\hat{\psi}^{\dagger}_{\mathcal{H}}(\mathbf{r}',t')\right\rangle+\vartheta(t,t')\delta(\mathbf{r}-\mathbf{r}').
\end{aligned}$$

The term proportional to $\vartheta(t,t')$ arises from the derivative of the time-ordering operator $\mathcal{T}$. The time evolution of an operator $\hat{P}$ in the Heisenberg picture can be calculated via Heisenberg's equations of motion

$$\frac{\mathrm{d}}{\mathrm{d}t}\hat{P}_{\mathcal{H}}=-\frac{i}{\hbar}\left[\hat{P}_{\mathcal{H}},\hat{H}\right].$$

Here, we introduce the Hamiltonian $\hat{H}$ that describes our system and consists of the non-interacting, one-particle part $\hat{H}_0$ that contains the kinetic energy and electrostatic potential, and an interaction part that accounts for all scattering mechanisms. Here, we consider an arbitrary interaction operator $\hat{V}$ that describes e. g. carrier–carrier interactions. Other scattering mechanisms like carrier–phonon interactions can be treated analogously. Thus, the Hamiltonian $\hat{H}$ in the quantum field operator representation reads

$$\begin{aligned}
\hat{H}&=\hat{H}_0+\hat{V} \\
&=\int\mathrm{d}\mathbf{r}\,\hat{\psi}^{\dagger}_{\mathcal{H}}(\mathbf{r},t)H_0(\mathbf{r})\hat{\psi}_{\mathcal{H}}(\mathbf{r},t) \\
&\quad+\frac{1}{2}\int\mathrm{d}\mathbf{r}\int\mathrm{d}\mathbf{r}'\hat{\psi}^{\dagger}_{\mathcal{H}}(\mathbf{r},t)\hat{\psi}^{\dagger}_{\mathcal{H}}(\mathbf{r}',t')V(\mathbf{r},t,\mathbf{r}',t')\hat{\psi}_{\mathcal{H}}(\mathbf{r}',t')\hat{\psi}_{\mathcal{H}}(\mathbf{r},t).
\end{aligned}\tag{1.2}$$

Now, the time evolution of the annihilation operator $\hat{\psi}_{\mathcal{H}}(\mathbf{r},t)$ is

$$i\hbar\frac{\mathrm{d}}{\mathrm{d}t}\hat{\psi}_{\mathcal{H}}(\mathbf{r},t)=H_0(\mathbf{r})\hat{\psi}_{\mathcal{H}}(\mathbf{r},t)+\int\mathrm{d}\mathbf{r}'\,V(\mathbf{r},t,\mathbf{r}',t')\hat{\psi}^{\dagger}_{\mathcal{H}}(\mathbf{r}',t')\hat{\psi}_{\mathcal{H}}(\mathbf{r}',t')\hat{\psi}_{\mathcal{H}}(\mathbf{r},t).$$

If we multiply this equation with the creation operator $\hat{\psi}^\dagger_{\mathcal{H}}(\mathbf{r}', t')$, apply the time-order operator $\mathcal{T}$, add the term $\vartheta(t, t')\,\delta(\mathbf{r} - \mathbf{r}')$ on both sides, and build the expectation value of the resulting expression, we arrive at the equation of motion for the non-equilibrium Green's function $G(\mathbf{r}, t, \mathbf{r}', t')$. To keep the notation clean and compact, we introduce the following abbreviations,

$$\begin{aligned} \mathbf{1} &\equiv (\mathbf{r}_1, t_1), \\ \delta(\mathbf{1}, \mathbf{2}) &\equiv \vartheta(t_1, t_2)\,\delta(\mathbf{r}_1 - \mathbf{r}_2), \\ \int \mathrm{d}\mathbf{1} &\equiv \int \mathrm{d}\mathbf{r}_1 \oint_C \mathrm{d}t_1, \end{aligned}$$

where the time-integration $\oint_C$ is along the chronological as well as the anti-chronological part of the contour $C = C_c \cup C_a$.

Altogether, the equation of motion for the non-equilibrium Green's function $G(\mathbf{r}_1, t_1, \mathbf{r}_2, t_2) = G(\mathbf{1}, \mathbf{2})$ with respect to the time t reads

$$\left(i\hbar \frac{\mathrm{d}}{\mathrm{d}t_1} - H_0(\mathbf{r}_1) \right) G(\mathbf{1}, \mathbf{1}') = \delta(\mathbf{1}, \mathbf{1}') - i\hbar \int \mathrm{d}\mathbf{2}\, V(\mathbf{1}, \mathbf{2})\, G^{(2)}(\mathbf{1}, \mathbf{2}, \mathbf{1}', \mathbf{2}), \tag{1.3}$$

where $G^{(2)}$ is the two-particle Green's function defined by

$$G^{(2)}(\mathbf{1}, \mathbf{2}, \mathbf{1}', \mathbf{2}') = \frac{1}{\hbar^2} \left\langle T \left\{ \hat{\psi}_{\mathcal{H}}(\mathbf{1}) \hat{\psi}_{\mathcal{H}}(\mathbf{2}) \hat{\psi}^\dagger_{\mathcal{H}}(\mathbf{2}') \hat{\psi}^\dagger_{\mathcal{H}}(\mathbf{1}') \right\} \right\rangle .$$

Analogously, the equation of motion for $G(\mathbf{1}, \mathbf{1}')$ with respect to time t' can be derived.

The equation of motion for the one-particle Green's function G in Eq. (1.3) induces an infinite hierarchy of equations since the time-evolution of G requires the knowledge of the two-particle Green's function $G^{(2)}$. However, the equation of motion for the two-particle Green's function requires the knowledge of the three-particle Green's function $G^{(3)}$ and so on. To truncate this infinite series of recursion, we can approximate the two-particle Green's function and introduce the so-called self-energy $\Sigma(\mathbf{1}, \mathbf{2})$ in Eq. (1.3) on the right-hand-side as follows

$$\left(i\hbar \frac{\mathrm{d}}{\mathrm{d}t_1} - H_0(\mathbf{r}_1) \right) G(\mathbf{1}, \mathbf{1}') = \delta(\mathbf{1}\mathbf{1}') + \int \mathrm{d}\mathbf{2}\, \Sigma(\mathbf{1}, \mathbf{2}) G(\mathbf{2}, \mathbf{1}'). \tag{1.4}$$

This self-energy Σ as approximation for the two-particle Green's function $G^{(2)}$ is the result of the application of Feynman's diagrams [Mat67], Wick's decomposition [FW71], or the application of functional derivatives [BK95]. Any of the aforementioned techniques allow the approximation of the self-energy Σ to any desired complexity, e. g. Hartree–Fock [Dan84] or second-order Born [Mah90].

1.2 PIECEWISE DEFINED GREEN'S FUNCTIONS

The equations of motion for the non-equilibrium Green's function G include integrals $\oint_C$ over the time contour C. However, it is not straightforward to keep track of the times t and t' on the chronological branch C_c and the anti-chronological branch C_a. Nevertheless, we can set the initial time t_0 on the contour C in Fig. 1.1 to $t_0 \to -\infty$, if we do not consider any initial correlations explicitly [Hal75; KT82]. Furthermore, we can extend the contour C beyond the largest time and let $t_1 \to \infty$, since the time-evolution operator is unitary. Thus, we finally get the so-called Keldysh–Contour C_K [Kel65] that is shown in Fig. 1.2. On the Keldysh–Contour, we can split the contour-ordered Green's function G and work with four piecewise defined Green's functions, since this is more convenient for quantum transport problems. The four piecewise defined Green's functions read

$$G(\mathbf{1},\mathbf{1}') = \begin{cases} G^c(\mathbf{1},\mathbf{1}') & : \quad t,t' \in C_c, \\ G^a(\mathbf{1},\mathbf{1}') & : \quad t,t' \in C_a, \\ G^<(\mathbf{1},\mathbf{1}') & : \quad t \in C_c \text{ and } t' \in C_a, \\ G^>(\mathbf{1},\mathbf{1}') & : \quad t \in C_a \text{ and } t' \in C_c, \end{cases} \tag{1.5}$$

where the chronological branch C_c and the anti-chronological branch C_a lie on the Keldysh–Contour C_K. The chronologically time-ordered Green's function G^c and the anti-chronologically time-ordered Green's function G^a read

$$G^c(\mathbf{1},\mathbf{1}') = -\frac{i}{\hbar}\left\langle \mathcal{T}^c\left\{\hat{\psi}^\dagger_{\mathcal{H}}(\mathbf{1})\hat{\psi}_{\mathcal{H}}(\mathbf{1}')\right\}\right\rangle,$$
$$G^a(\mathbf{1},\mathbf{1}') = -\frac{i}{\hbar}\left\langle \mathcal{T}^a\left\{\hat{\psi}^\dagger_{\mathcal{H}}(\mathbf{1})\hat{\psi}_{\mathcal{H}}(\mathbf{1}')\right\}\right\rangle,$$

where $\mathcal{T}^c$ is the chronological time-ordering operator that always moves the operators with the earlier time arguments to the right and $\mathcal{T}^a$ is the anti-chronological time-

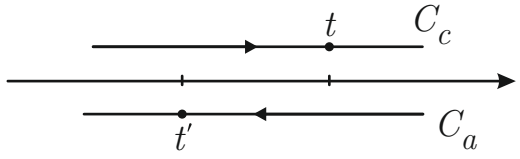

Figure 1.2: The Keldysh–Contour $C_K = C_c \cup C_a$ where the initial time $t_1 \to -\infty$ and the largest time $t_1 \to \infty$. As an example two times t and t' are shown where t' is later on C_K but $t' < t$. Note that both branches C_c and C_a lie on the time axis.

ordering operator that always moves the operators with the later time arguments to the right. The lesser Green's function $G^<$ and the greater Green's function $G^>$ read

$$G^<(\mathbf{1},\mathbf{1}') = +\frac{i}{\hbar}\left\langle \hat{\psi}^\dagger_{\mathcal{H}}(\mathbf{1}')\hat{\psi}_{\mathcal{H}}(\mathbf{1})\right\rangle,$$
$$G^>(\mathbf{1},\mathbf{1}') = -\frac{i}{\hbar}\left\langle \hat{\psi}_{\mathcal{H}}(\mathbf{1})\hat{\psi}^\dagger_{\mathcal{H}}(\mathbf{1}')\right\rangle.$$

Note that no time-ordering operator is required for the lesser and greater Green's functions since the two times t and t' are located on different branches and thus the time-ordering on the contour is already well-defined.

For quantum transport calculations the two Green's functions $G^>$ and $G^<$ are directly related to observable quantities. However, instead of working with the chronological and anti-chronological Green's functions, it is more convenient to introduce the retarded Green's function G^R and the advanced Green's function G^A, since their physical interpretation is more straightforward. They are defined as

$$G^R(\mathbf{1},\mathbf{1}') = G^c(\mathbf{1},\mathbf{1}') - G^<(\mathbf{1},\mathbf{1}'),$$
$$G^A(\mathbf{1},\mathbf{1}') = G^c(\mathbf{1},\mathbf{1}') - G^>(\mathbf{1},\mathbf{1}').$$

All these newly introduced Green's functions are not linearly independent but they are connected via the following relations [Dan84]

$$G^c(\mathbf{1},\mathbf{1}') + G^a(\mathbf{1},\mathbf{1}') = G^>(\mathbf{1},\mathbf{1}') - G^<(\mathbf{1},\mathbf{1}'),$$
$$G^R(\mathbf{1},\mathbf{1}') - G^A(\mathbf{1},\mathbf{1}') = G^>(\mathbf{1},\mathbf{1}') - G^<(\mathbf{1},\mathbf{1}'). \tag{1.6}$$

Thus, three different piecewise defined Green's functions are sufficient to completely characterize a non-equilibrium quantum system. Analogously to the Green's functions, we can define piecewise self-energies, the retarded self-energy Σ^R, the advanced self-energy Σ^A, the lesser self-energy $\Sigma^<$, and the greater self-energy $\Sigma^>$. For these self-energies, an equivalent relation to Eq. (1.6) holds [Dan84]

$$\Sigma^R(\mathbf{1},\mathbf{1}') - \Sigma^A(\mathbf{1},\mathbf{1}') = \Sigma^>(\mathbf{1},\mathbf{1}') - \Sigma^<(\mathbf{1},\mathbf{1}').$$

1.3 LANGRETH'S THEOREM

In the equation of motion for the Green's function in Eq. (1.4) there are several product terms of Green's functions and self-energies. One accruing term is e. g. a time convolution of the following structure

$$F(t,t') = \int \mathrm{d}\tau\, A(t,\tau)B(\tau,t'), \tag{1.7}$$

where the integral over τ runs over the whole contour C_K as depicted in Fig. 1.2. Since we want to work with the piecewise defined Green's functions, we have to evaluate the product in Eq. (1.7) for the retarded, advanced, greater, and lesser part. Let us assume we want to calculate $F^<$, i. e. t is on the chronological branch C_c and t' is on the anti-chronological branch C_a. With the definition of the Green's function in Eq. (1.1) and the definition of the piecewise defined Green's functions in Eq. (1.5), we can write the functions A and B as follows

$$A(t\,,\tau) = \theta(t\,,\tau)A^>(t\,,\tau) + \theta(\tau,t\,)A^<(t\,,\tau),$$
$$B(\tau,t') = \theta(\tau,t')B^>(\tau,t') + \theta(t',\tau)B^<(\tau,t').$$

Inserting these expressions into Eq. (1.7), we get product terms of Green's functions and Heaviside's functions. This is in principle a deformation and an appropriate splitting of the time contour. A detailed proof and derivation of Langreth's theorem is given e. g. by Haug and Jauho in Ref. [HJ89]. The evaluation of the arising products leads to the following compact result [HJ89; Lui07]

$$F^<(t,t') = \int_{-\infty}^{+\infty} \mathrm{d}\tau \left(A^R(t,\tau)B^<(\tau,t') + A^<(t,\tau)B^A(\tau,t') \right). \tag{1.8}$$

With the same procedure, we can evaluate the retarded and advanced functions and we get

$$F^{R/A}(t,t') = \int_{t'}^{t} \mathrm{d}\tau\; A^{R/A}(t,\tau)B^{R/A}(\tau,t'). \tag{1.9}$$

Note that the integration does not include the whole contour due to the various Heaviside's functions and the different restricted domains of the piecewise defined Green's functions and self-energies.

Another type of possible terms are direct products of the form

$$F(t,t') = A(t,t')\; B(t,t'),$$

where t and t' lie on the contour C_K. When the two time parameters are located on different branches of the contour, it directly follows that

$$C^\lessgtr(t,t') = A^\lessgtr(t,t')\; B^\lessgtr(t,t'). \tag{1.10}$$

The treatment of the retarded and advanced Green's functions of direct product terms is a bit more demanding, however, the derivation is straightforward [Dan84]. After lengthy calculations, the retarded and advanced functions read

$$C^{R/A}(t,t') = A^{R/A}(t,t')B^{R/A}(t,t') + A^{R/A}(t,t')B^{\lessgtr}(t,t') + A^{\lessgtr}(t,t')B^{R/A}(t,t'). \tag{1.11}$$

These direct product terms are especially useful to derive the scattering self-energies, as discussed in Sec. 1.9.2.

Finally, we can rewrite the equations of motion for the non-equilibrium Green's function $G(\mathbf{1},\mathbf{1}')$ with the help of the convolution terms. For the retarded and advanced part they read as follows

$$\left(i\hbar\frac{\mathrm{d}}{\mathrm{d}t_1} - H_0(\mathbf{r}_1)\right) G^{R/A}(\mathbf{1},\mathbf{1}') = \delta(\mathbf{1}\mathbf{1}') + \int\mathrm{d}\mathbf{2}\, \Sigma^{R/A}(\mathbf{1},\mathbf{2})G^{R/A}(\mathbf{2},\mathbf{1}'), \tag{1.12}$$

whereas the equation of motion for the lesser part reads

$$\left(i\hbar\frac{\mathrm{d}}{\mathrm{d}t_1} - H_0(\mathbf{r}_1)\right) G^{<}(\mathbf{1},\mathbf{1}') = \int\mathrm{d}\mathbf{2}\, \Big(\Sigma^{R}(\mathbf{1},\mathbf{2})G^{<}(\mathbf{2},\mathbf{1}') + \Sigma^{<}(\mathbf{1},\mathbf{2})G^{A}(\mathbf{2},\mathbf{1}')\Big). \tag{1.13}$$

The equation of motion for the retarded and advanced Green's function in Eq. (1.12) is a recursive equation. However, we can rewrite this equation and obtain the following form that is known as Dyson's equation

$$\int\mathrm{d}\mathbf{2}\, \left(\Big(i\hbar\frac{\mathrm{d}}{\mathrm{d}t_1} - H_0(\mathbf{r}_1)\Big)\delta(\mathbf{1},\mathbf{2}) - \Sigma^{R}(\mathbf{1},\mathbf{2})\right) G^{R}(\mathbf{2},\mathbf{1}') = \delta(\mathbf{1},\mathbf{1}'). \tag{1.14}$$

In a similar way, the equation of motion for the lesser Green's function in Eq. (1.13) also states a recursive equation. With the help of Dyson's equation in Eq. (1.14), we obtain the following form that is known as Keldysh's equation

$$G^{<}(\mathbf{1},\mathbf{1}') = \int\mathrm{d}\mathbf{2}\int\mathrm{d}\mathbf{3}\, G^{R}(\mathbf{1},\mathbf{2})\, \Sigma^{<}(\mathbf{2},\mathbf{3})\, G^{A}(\mathbf{3},\mathbf{1}'). \tag{1.15}$$

In principle, the equations for the retarded and advanced Green's functions can be solved independently from the lesser Green's function. However, scattering mechanisms lead in general to a coupling of the retarded and advanced self-energies with the retarded, advanced, and lesser Green's functions. Within such a coupled system, the solution of Dyson's equation (1.14) and Keldysh's equation (1.15) is very difficult and cumbersome to find.

1.4 STATIONARY KINETIC EQUATIONS

Under steady-state conditions, i. e. the non-equilibrium system has reached a stationary solution, the Green's functions and self-energies do not depend on two times t and t' but solely on the time difference $\tau = t - t'$. Thus, we can Fourier transform the time difference coordinate τ into the energy domain

$$G(\mathbf{r}, \mathbf{r}', E) = \int \mathrm{d}\tau \, \exp\left(\frac{iE\tau}{\hbar}\right) G(\mathbf{r}, \mathbf{r}', \tau).$$

The inverse Fourier transformation is defined as

$$G(\mathbf{r}, \mathbf{r}, \tau) = \frac{1}{2\pi\hbar} \int \mathrm{d}E \, \exp\left(\frac{-iE\tau}{\hbar}\right) G(\mathbf{r}, \mathbf{r}', E).$$

The stationary self-energies Σ also depend on the time difference τ only. Thus, the Fourier transformed steady-state Dyson equation reads

$$\int \mathrm{d}\mathbf{r}_1 \left(\Big(E - H_0(\mathbf{r})\Big)\delta(\mathbf{r} - \mathbf{r}_1) - \Sigma^R(\mathbf{r}, \mathbf{r}_1, E) \right) G^R(\mathbf{r}_1, \mathbf{r}', E) = \delta(\mathbf{r} - \mathbf{r}'), \quad (1.16)$$

and the Fourier transformed steady-state Keldysh equation reads

$$G^<(\mathbf{r}, \mathbf{r}', E) = \int \mathrm{d}\mathbf{r}_1 \int \mathrm{d}\mathbf{r}_2 \, G^R(\mathbf{r}, \mathbf{r}_1, E) \, \Sigma^<(\mathbf{r}_1, \mathbf{r}_2, E) \, G^A(\mathbf{r}_2, \mathbf{r}', E). \quad (1.17)$$

Under steady-state conditions the following very useful relation for the advanced Green's function holds [Dat95]

$$G^A(\mathbf{r}, \mathbf{r}', E) = \Big(G^R(\mathbf{r}, \mathbf{r}', E)\Big)^\dagger. \quad (1.18)$$

1.5 FLUCTUATION–DISSIPATION THEOREM

The individual piecewise defined Green's functions are not independent but they are linked via Eq. (1.6). This equation holds in the equilibrium case as well as in the non-equilibrium case. However, for a fermionic system in equilibrium, an even more fundamental relation between the lesser and greater Green's function holds [Dan84; Lui07]

$$G^>(\mathbf{r}, \mathbf{r}', E) = -\exp\left(\frac{E - \mu}{k_B T}\right) G^<(\mathbf{r}, \mathbf{r}', E), \quad (1.19)$$

where μ is the chemical potential of the system, k_B is Boltzmann's constant, and T is the temperature of system. Combining Eq. (1.6) and Eq. (1.19), we get the following useful relation for equilibrium systems that is known as fluctuation–dissipation theorem

$$G^<(\mathbf{r}, \mathbf{r}', E) = i\, f(E)\, A(\mathbf{r}, \mathbf{r}', E), \tag{1.20}$$

where f is the Fermi distribution and A is the so-called spectral function or auto-correlation function

$$A(\mathbf{r}, \mathbf{r}', E) = i\Big(G^R(\mathbf{r}, \mathbf{r}', E) - G^{R\dagger}(\mathbf{r}, \mathbf{r}', E)\Big). \tag{1.21}$$

1.6 TRANSFORMATION INTO A DISCRETE BASIS

The non-equilibrium Green's function G and thus all piecewise defined Green's functions and self-energies depend on two continuous spatial variables $\mathbf{r}$ and $\mathbf{r}'$ due to the quantum field operators $\hat{\psi}_{\mathcal{H}}(\mathbf{r}, t)$ and $\hat{\psi}^\dagger_{\mathcal{H}}(\mathbf{r}', t')$. As we already mentioned, we dispensed with the explicit naming of any further variables and indexes to keep the notation compact. Furthermore, the actual parameters depend on the physical model and e. g. on the geometry of the system. However, regardless of the actual parameters of the quantum field operators, they can be expressed as a linear combination of spatial basis functions $\phi_n(\mathbf{r})$. Here, the index n accounts for all additional parameters. These functions $\phi_n(\mathbf{r})$ constitute a complete basis of the single-particle Hilbert space $\mathcal{H}$. To avoid mathematical and numerical indefiniteness and problems with convergence, we assume the Hilbert space $\mathcal{H}$ to be finite dimensional. From a fundamental point of view, this assumption seems unsatisfactorily, but in practical applications it will always hold [Thy06].

Note that throughout this work, we use Greek letters to indicate summation indexes, whereas Roman letters are used for all other indexes. The quantum field operators in the basis $\phi_n(\mathbf{r})$ read

$$\hat{\psi}_{\mathcal{H}}(\mathbf{r}, t) = \sum_\alpha \hat{c}_\alpha(t)\phi_\alpha(\mathbf{r}),$$
$$\hat{\psi}^\dagger_{\mathcal{H}}(\mathbf{r}, t) = \sum_\alpha \hat{c}^\dagger_\alpha(t)\phi^*_\alpha(\mathbf{r}),$$

where the creation operator $\hat{c}^\dagger_n$ creates a particle in state n and the annihilation operator $\hat{c}_n$ removes a particle in state n. Note that the basis functions $\phi_n(\mathbf{r})$ need not necessarily be orthonormal. Therefore, the overlap matrix $\mathcal{S}$ is defined as

$$\mathcal{S}_{nm} = \int \mathrm{d}\mathbf{r}\; \phi_n(\mathbf{r})\phi^*_m(\mathbf{r}). \tag{1.22}$$

Hence, to any one-particle operator $\hat{P}$ we can associate the following matrix

$$P_{nm} = \int \mathrm{d}\mathbf{r}_1 \int \mathrm{d}\mathbf{r}_2 \sum_{\alpha,\beta} \mathcal{S}^{-1}_{n\alpha} \phi^*_\alpha(\mathbf{r}_1)\, \hat{P}(\mathbf{r}_1, \mathbf{r}_2)\, \phi_\beta(\mathbf{r}_2) \mathcal{S}^{-1}_{\beta m}. \tag{1.23}$$

In particular, the basis-transformed Hamiltonian $H_0(\mathbf{r})$ reads

$$H_{nm} = \int \mathrm{d}\mathbf{r} \sum_{\alpha,\beta} \mathcal{S}^{-1}_{n\alpha} \phi^*_\alpha(\mathbf{r})\, H_0(\mathbf{r})\, \phi_\beta(\mathbf{r}) \mathcal{S}^{-1}_{\beta m}.$$

The inverse basis-transformation is quite obvious and thus, as an example, the Green's function G can be expressed as

$$G(\mathbf{r}, \mathbf{r}', E) = \sum_{\alpha,\beta} \phi_\alpha(\mathbf{r})\, G_{nm}(E)\, \phi^*_\beta(\mathbf{r}').$$

Using the transformation in Eq. (1.23), we can rewrite Eq. (1.16) and we obtain the following matrix form of Dyson's equation

$$\sum_\alpha \Big(E\mathcal{S}_{n\alpha} - H_{n\alpha} - \Sigma^R_{n\alpha}(E) \Big) G^R_{\alpha m} = \delta_{nm}, \tag{1.24}$$

where δ_{nm} is Kronecker's delta. The basis-transformed version of Keldysh's equation reads

$$G^<_{nm}(E) = \sum_{\alpha,\beta} G^R_{n\alpha}(E)\, \Sigma^R_{\alpha\beta}(E)\, G^{R\dagger}_{\beta m}(E). \tag{1.25}$$

1.7 CHOICE OF BASIS REPRESENTATION

There are various different representations of Green's functions that can be found in literature. A suitable choice of the basis functions $\phi_n(\mathbf{r})$ depends on the system of interest and its geometry. Most basis representations are chosen to fit an actual device geometry or take advantage of specific device properties. For layered heterostructures like quantum cascade lasers e. g. Wannier or Wannier–Stark functions are very well suited for quantum transport calculations [Lee+06].

However, in this work we are interested in a very high degree of flexibility. Thus, we choose a real-space representation of the Green's functions to be able to handle arbitrary device geometries. Throughout this work, we only consider the envelope of the wave functions and we assume the lattice vector to be continuous on the

nanometer length scales of our interest. This is reasonable since the inter-atomic distances are at least one order of magnitude smaller [YC01].

In the following sections we briefly introduce common methods to discretize the partial differential equations within the non-equilibrium Green's function formalism in real space. These are the finite differences method and the finite element method. Finally, we present an optimized real space basis for layered heterostructures.

1.7.1 *General Real-Space Basis Representation*

First, we give a brief overview of the finite differences method (FEM). The construction of the finite difference methods for partial differential equations is quite intuitive. First, we consider a rectangular tensor grid in real-space where the grid points are labeled $\mathbf{r}_n$. Here, we will use a uniform grid spacing Δ in all three spatial dimensions. Note, that an adaption to a non-uniform rectilinear tensor grid is straightforward. Then, we use finite differences to approximate the derivatives. Thus, the first derivative along the x-direction of a function F can be approximated with either the so-called forward difference

$$\frac{\partial F(\mathbf{r}_n)}{\partial x} = \frac{F(\mathbf{r}_n + \Delta\mathbf{x}) - F(\mathbf{r}_n)}{\Delta} + \mathcal{O}(\Delta),$$

or with the so-called backward difference

$$\frac{\partial F(\mathbf{r}_n)}{\partial x} = \frac{F(\mathbf{r}_n) - F(\mathbf{r}_n - \Delta\mathbf{x})}{\Delta} + \mathcal{O}(\Delta), \tag{1.26}$$

where $\mathbf{x}$ is a unit vector in x-direction and $F(\mathbf{r}_n \pm \Delta\mathbf{x}) = F(\mathbf{r}_{m\pm})$ with the appropriate neighboring grid points $\mathbf{r}_{m\pm}$. Note that a combination of the forward and backward difference reduces the truncation error by one order of magnitude

$$\frac{\partial F(\mathbf{r}_n)}{\partial x} = \frac{F(\mathbf{r}_n + \Delta\mathbf{x}) - F(\mathbf{r}_n - \Delta\mathbf{x})}{2\Delta} + \mathcal{O}(\Delta^2).$$

This is the so-called central difference. Note that such a discretization of first derivatives is not unique and prone to unphysical oscillatory solutions. To avoid these unphysical so-called ghost states an up-winding scheme or an extended forward-backward-differencing scheme has to be applied [And04; And09]. Applying the finite differences scheme again, we can approximate the second derivative of a function F along the x-direction as follows

$$\frac{\partial^2 F(\mathbf{r}_n)}{\partial x^2} = \frac{F(\mathbf{r}_n + \Delta\mathbf{x}) - 2F(\mathbf{r}_n) + F(\mathbf{r}_n - \Delta\mathbf{x})}{\Delta^2} + \mathcal{O}(\Delta^2).$$

Note that derivatives along the y- and z-direction as well as mixed derivatives can be approximated with an analogous scheme. The finite differences method has to be extended to be flux conserving in the presence of material discontinuities as they occur in semiconductor nanostructures. All details of the so-called box discretization method are given by Till Andlauer in Ref. [And04]. The elements $\phi_n(\mathbf{r})$ of the discrete basis defined in Sec. 1.6 within a finite differences method read

$$\phi_n(\mathbf{r}) = \begin{cases} \dfrac{1}{\sqrt{\Delta^3}} & \mathbf{r} \in R_\Delta(\mathbf{r}_n) \\ 0 & \text{elsewhere} \end{cases},$$

where $R_\Delta(\mathbf{r}_n) = \{\mathbf{r} : \|\mathbf{r} - \mathbf{r}_n\|_\infty < \frac{\Delta}{2}\}$ is the rectangular region around the center $\mathbf{r}_n$ with extent Δ in all three spatial directions. Note that these basis functions are orthonormal and thus, the overlap matrix $\mathcal{S}$ that is defined in Eq. (1.22) is consequently the unit matrix. Finally, the matrix that can be associated with an operator P that was defined in Eq. (1.23) has the following simple form within the finite differences method

$$P_{nm} = \Delta^{-3} \int\limits_{R_\Delta(\mathbf{r}_n)} \mathrm{d}\mathbf{r}_1 \int\limits_{R_\Delta(\mathbf{r}_m)} \mathrm{d}\mathbf{r}_2 \, \hat{P}(\mathbf{r}_1, \mathbf{r}_2) \overset{\Delta \to 0}{=} \Delta^3 \hat{P}(\mathbf{r}_n, \mathbf{r}_m),$$

where the last equality holds in the limit of a small grid spacing.

Besides the finite differences method, the finite element method (FEM) is also a popular approach to the numerical solution of partial differential equations. There are many publications about it in numerical analysis literature. Also, much has been written about the theory and the practice of the various finite element methods, their connection with variational principles, their convergence, and their stability. A very good and instructive introduction to the finite element method is given by e. g. Larry Segerlind in Ref. [Seg84]. Further readings are e. g. Ref. [JH92] and Ref. [Pre89]. Details on the finite element method regarding quantum mechanical calculations and especially the elimination of the so-called spurious solutions and the preservation of symmetry properties are given by Thomas Eißfeller in Ref. [Eiß12].

1.7.2 *Special Real-Space Basis for Layered Heterostructures*

For layered heterostructures there exist very custom-tailored bases to efficiently calculate quantum transport properties for particular types of devices, e.g. Wannier or Wannier-Stark functions for quantum cascade lasers [Wac02b; Lee+06]. However, in this work we want to retain the full flexibility of arbitrary device geometries and

thus, we work within a real-space basis. Nevertheless, we can take the advantage of the fact that the individual layers of layered heterostructures are homogeneous. Due to this homogeneity, the assumption of plane waves with lateral momentum $\mathbf{k}_\parallel$ is justified. Thus, the envelope of the wave functions reads [Kub10]

$$\hat{\psi}(\mathbf{r},t) = \frac{\exp(i\mathbf{k}_\parallel \mathbf{r}_\parallel)}{\sqrt{A}} \hat{\psi}(z,t),$$

where A is the area of the lateral component, z is the growth direction of the structure, and $\mathbf{r}_\parallel = (x,y)^T$ is the position vector within a layer. For the quantum field operator $\hat{\psi}(z,t)$ we can choose a one-dimensional real-space representation as described in the previous section. Within this so-called quasi-one-dimensional basis Dyson's equation for the stationary case reads

$$\int \mathrm{d}z_1 \Big(\big(E - H_0(z,k_\parallel)\big)\delta(z-z_1) - \Sigma^R(z,z_1,k_\parallel,E) \Big) \times G^R(z_1,z',k_\parallel,E) = \delta(z-z'), \tag{1.27}$$

whereas Keldysh's equation for the stationary case reads

$$G^<(z,z',k_\parallel,E) = \int \mathrm{d}z_1 \int \mathrm{d}z_2 \, G^R(z,z_1,k_\parallel,E) \, \Sigma^<(z_1,z_2,k_\parallel,E) \, G^{R\dagger}(z_2,z',k_\parallel,E).$$

Note that the Green's functions and self-energies do not depend on the direction of the lateral momentum $\mathbf{k}_\parallel$ but only the absolute value $k_\parallel = \left|\mathbf{k}_\parallel\right|$ due to symmetry reasons. This simplifies the numerical effort remarkably and thus, quantum transport calculations for at least small layered devices become feasible.

1.8 RELATIONS TO OBSERVABLES

Under steady-state conditions, the retarded Green's function G^R and the lesser Green's function $G^<$ are sufficient to completely describe a non-equilibrium system. This is due to the fact that the advanced Green's function G^A is related to G^R via Eq. (1.18). Within the non-equilibrium Green's function formalism, G^R characterizes the width and energy of the scattering states, whereas the $G^<$ characterizes the state occupancy. Thus, observable quantities such as charge and current densities are directly connected to $G^<$. In this section, we discuss the most important observables and their relation to the Green's functions.

1.8.1 *Local Density of States*

The spectral function A was defined in Eq. (1.21). It can be viewed as a generalized density of states since it gives information about the location, energy, and type of states regardless of their occupation. The local density of states ρ is given by the diagonal elements of the spectral function A. It reads

$$\rho(\mathbf{r}, E) = \frac{1}{2\pi} A(\mathbf{r}, \mathbf{r}, E) = -\frac{1}{\pi} \mathrm{Im}\, G^R(\mathbf{r}, \mathbf{r}, E). \tag{1.28}$$

The last equality is obtained with the definition of the spectral function in Eq. (1.21). Within the general basis representation $\phi_n(\mathbf{r})$ the local density of states ρ reads

$$\rho(\mathbf{r}, E) = -\frac{1}{\pi} \mathrm{Im} \sum_{\alpha,\beta} \phi_\alpha(\mathbf{r}) G^R_{\alpha\beta}(E) \phi^*_\beta(\mathbf{r}).$$

1.8.2 *Carrier Density*

The carrier density is given by [FJ92; Dat95]

$$n(\mathbf{r}, t) = \left\langle \hat{\psi}^\dagger_{\mathcal{H}}(\mathbf{r}, t) \hat{\psi}_{\mathcal{H}}(\mathbf{r}, t) \right\rangle = -i\hbar\, G^<(\mathbf{r}, t, \mathbf{r}, t), \tag{1.29}$$

where the last equality is obtained by combining Eq. (1.1) and Eq. (1.5). The energy-resolved steady-state carrier density within the general basis representation $\phi_n(\mathbf{r})$ reads

$$n(\mathbf{r}, E) = \frac{-i}{2\pi} \sum_{\alpha,\beta} \phi_\alpha(\mathbf{r}) G^<_{\alpha\beta}(E) \phi^*_\beta(\mathbf{r}).$$

It gives information about the spatial and energy-resolved location of resonant states and their occupation as well as the confinement of carriers in the resonant states. Finally, the total, energy-integrated carrier density reads

$$n(\mathbf{r}) = \int \mathrm{d}E\, n(\mathbf{r}, E). \tag{1.30}$$

1.8.3 *Current Density*

To derive the current density, we use the conservation law for quantum mechanical variables [KB62]. The continuity equation links the carrier density with the current density

$$e \frac{\mathrm{d}}{\mathrm{d}t} n(\mathbf{r}, t) + \nabla\, \mathbf{j}(\mathbf{r}, t) = 0, \tag{1.31}$$

where e is the charge of the carriers. With the help of Eq. (1.13) we can express the time-derivative of the carrier density as follows

$$\begin{aligned}\frac{\mathrm{d}}{\mathrm{d}t_1}n(\mathbf{r}_1,t_1) &= -\lim_{t_2\to t_1} i\hbar\left(\frac{\mathrm{d}}{\mathrm{d}t_1}+\frac{\mathrm{d}}{\mathrm{d}t_2}\right)G^<(\mathbf{r}_1,t_1,\mathbf{r}_1,t_2)\\ &= -\lim_{\mathbf{r}_2\to\mathbf{r}_1}\Big(H_0(\mathbf{r}_1)-H_0(\mathbf{r}_2)\Big)G^<(\mathbf{r}_1,t_1,\mathbf{r}_2,t_1)+R(\mathbf{1}),\end{aligned} \tag{1.32}$$

where

$$\begin{aligned}R(\mathbf{1}) = \int\mathrm{d}\mathbf{3}\Big(&\Sigma^R(\mathbf{1},\mathbf{3})G^<(\mathbf{3},\mathbf{1})+\Sigma^<(\mathbf{1},\mathbf{3})G^A(\mathbf{3},\mathbf{1})\\ &-G^R(\mathbf{1},\mathbf{3})\Sigma^<(\mathbf{3},\mathbf{1})-G^<(\mathbf{1},\mathbf{3})\Sigma^A(\mathbf{3},\mathbf{1}).\end{aligned}$$

This term R must be zero to obey particle, momentum, and energy conservation laws [KB62]. However, note that this term does not automatically vanish. Instead, approximations to the scattering self-energies easily break conservation laws [Kub10; KV11], as discussed in Chapter 4. Comparing Eq. (1.32) with the continuity equation in Eq. (1.31), we can define the divergence of the current density as follows

$$\nabla\mathbf{j}(\mathbf{r},t) = -e\lim_{\mathbf{r}'\to\mathbf{r}}\Big(H_0(\mathbf{r}')-H_0(\mathbf{r})\Big)G^<(\mathbf{r},t,\mathbf{r}',t). \tag{1.33}$$

For a non-interacting Hamiltonian H_0 that is quadratic in momentum operators, e. g.

$$H_0(\mathbf{r}) = -\frac{\hbar^2}{2m}\nabla_{\mathbf{r}}^2+V(\mathbf{r}), \tag{1.34}$$

where m is the mass of the particles and $V(\mathbf{r})$ is the electrostatic potential, we can express the current density $\mathbf{j}$ as follows [Dat95]

$$\mathbf{j}(\mathbf{r},t) = \frac{e\hbar^2}{2m}\lim_{\mathbf{r}'\to\mathbf{r}}\Big(\nabla_{\mathbf{r}'}-\nabla_{\mathbf{r}}\Big)G^<(\mathbf{r},t,\mathbf{r}',t).$$

Note that the contributions of the electrostatic potential $V(\mathbf{r})$ cancel out. Thus, the energy-resolved steady-state current density within the general basis representation $\phi_n(\mathbf{r})$ reads

$$\mathbf{j}(\mathbf{r},E) = \frac{e\hbar}{4\pi m}\Big(\big(\nabla\phi_\alpha(\mathbf{r})\big)\phi_\beta^*(\mathbf{r})-\phi_\alpha(\mathbf{r})\big(\nabla\phi_\beta^*(\mathbf{r})\big)\Big)G^<_{\alpha\beta}(E), \tag{1.35}$$

and the total, energy-integrated current density reads

$$\mathbf{j}(\mathbf{r}) = \int\mathrm{d}E\,\mathbf{j}(\mathbf{r},E).$$

Another way to define the current density is via the commutator of the Hamiltonian and the polarization operator [Mah90]. This leads to the following useful form of the current density that reads in the general basis representation $\phi_n(\mathbf{r})$ as follows

$$\mathbf{j}_{nm}(E) = \frac{e}{h}\sum_{\alpha\beta}\Big(H_{n\alpha}\mathbf{r}_{\alpha\beta} - \mathbf{r}_{n\alpha}H_{\alpha\beta}\Big)G^{<}_{\beta m}(E), \tag{1.36}$$

where $\mathbf{r}_{nm}$ is the position operator

$$\mathbf{r}_{nm} = \int \mathrm{d}\mathbf{r}\ \sum_{\alpha,\beta}\mathcal{S}^{-1}_{n\alpha}\phi^{*}_{\alpha}(\mathbf{r})\ \mathbf{r}\ \phi_{\beta}(\mathbf{r})\mathcal{S}^{-1}_{\beta m}.$$

Hence, the total, spatially resolved, energy-integrated current reads

$$\mathbf{j}(\mathbf{r}) = \int \mathrm{d}E \sum_{\alpha,\beta}\phi_{\alpha}(\mathbf{r})\,\mathbf{j}_{\alpha\beta}(E)\,\phi^{*}_{\beta}(\mathbf{r}). \tag{1.37}$$

1.8.4 *Optical Gain*

In this section, we present the calculation of optical gain in current-driven semiconductor heterostructures within the framework of non-equilibrium Green's functions. Here, we follow Andreas Wacker in Ref. [Wac02a], where a detailed derivation can be found.

From standard electrodynamics [Jac98] the material gain γ can be calculated from the complex dynamical conductance σ [Wac02a]. Thus, the gain γ reads

$$\gamma(\mathbf{r},\omega) \approx -\frac{\mathrm{Re}\,\sigma(\mathbf{r},\omega)}{c\,\varepsilon_0}\left(\varepsilon_{\infty} - \frac{\mathrm{Im}\,\sigma(\mathbf{r},\omega)}{\varepsilon_0\omega}\right)^{-1/2},$$

where ω is the photon frequency, c is the speed of light, ε_0 is the electric vacuum permittivity, and ε_{∞} is the relative electric permittivity at the high frequency limit. The complex conductivity σ is calculated in the non-equilibrium Green's function transport theory in the presence of alternating electric fields as follows. After a self-consistent solution of the stationary transport equations is found, i. e. Dyson's equation in Eq. (1.14) and Keldysh's equation in Eq. (1.15) are solved, an additional weak radiation field F is taken into account. The corresponding time dependent perturbation potential δU reads

$$\delta U(t) = \frac{1}{2\pi}\int \mathrm{d}\omega\, e^{-i\omega t}\,\delta U(\omega).$$

Since we use a dipole approximation, i. e. we assume the photon wavelength to be large compared to the extent of our system, any k-dependent terms can be neglected. Furthermore, we neglect any higher-order term in the radiation field since it is assumed to be weak. Hence, the perturbation potential in the Lorentz gauge reads as follows [Wac02a]

$$\delta U(\omega) = -e\, F(\omega)\, \mathbf{r},$$

where F is the external radiation field. The resulting perturbation of the current density $\delta\mathbf{j}$ gives the conductivity via the relation

$$\sigma(\mathbf{r}, \omega) = \frac{\delta\mathbf{j}(\mathbf{r}, \omega)\, \mathbf{r}_\omega}{F(\omega)},$$

where $\mathbf{r}_\omega$ is the propagation direction of the photons. In order to calculate the perturbation of the current density $\delta\mathbf{j}$ as linear response of the system, the kinetic equations in Eq. (1.14) and Eq. (1.15) are linearized around the stationary, non-equilibrium solution. Thus, the perturbed Green's functions $\tilde{G}$ and the perturbed self-energies $\tilde{\Sigma}$ read

$$\tilde{G}(\mathbf{1}, \mathbf{2}) = G(\mathbf{1}, \mathbf{2}) + \delta G(\mathbf{1}, \mathbf{2}),$$
$$\tilde{\Sigma}(\mathbf{1}, \mathbf{2}) = \Sigma(\mathbf{1}, \mathbf{2}) + \delta\Sigma(\mathbf{1}, \mathbf{2}).$$

Since we are considering scattering effects, the perturbations of the Green's functions δG do explicitly depend on two times [Wac02a] and we have to Fourier transform with respect to both times

$$\delta G(\mathbf{r}_1, t_1, \mathbf{r}_2, t_2) = \frac{1}{4\pi^2\hbar} \int \mathrm{d}\omega\, e^{-i\omega t_1} \int \mathrm{d}E\, e^{-iE(t_1 - t_2)/\hbar}\, \delta G(\mathbf{r}_1, \mathbf{r}_2, \omega, E),$$

whereas the same Fourier transformation is used for the self-energies. The perturbations $\delta\Sigma$ depend on the perturbations of the Green's functions δG and vice versa. Thus, they have to be calculated in a self-consistent manner. The perturbations of the retarded and advanced Green's functions are determined by

$$\delta G^{R/A}(\omega, E) = G^{R/A}(E + \hbar\omega)\Big(\delta U(\omega) + \delta\Sigma^{R/A}(\omega, E)\Big) G^{R/A}(E),$$

whilst the perturbation of the lesser Green's function reads

$$\begin{aligned}
\delta G^{<}(\omega, E) = {} & G^R(E + \hbar\omega)\, \delta U(\omega)\, G^{<}(E) + G^{<}(E + \hbar\omega)\, \delta U(\omega)\, G^A(E) \\
& + G^R(E + \hbar\omega)\, \delta\Sigma^R(\omega, E)\, G^{<}(E) \\
& + G^R(E + \hbar\omega)\, \delta\Sigma^{<}(\omega, E)\, G^A(E) \\
& + G^{<}(E + \hbar\omega)\, \delta\Sigma^A(\omega, E)\, G^A(E).
\end{aligned}$$

Note that we omitted the spatial arguments and integrals for a more compact presentation. A detailed derivation of these equations can be found in Ref. [Wac02a] and Ref. [Kub10]. It is important to be aware of the fact that $\delta G^A \neq \delta G^{R\dagger}$ since the perturbations depend on two times explicitly. Once a self-consistent solution for the perturbations of the Green's functions and self-energies is found, we can calculate the perturbation of the current density with Eq. (1.36) and Eq. (1.37). Hence the perturbation of the current density $\delta\mathbf{j}$ in the general basis representation $\phi_n(\mathbf{r})$ reads

$$\delta\mathbf{j}_{nm}(\omega) = \frac{e}{h}\int \mathrm{d}E \sum_{\alpha\beta}\Big(\Big(\delta U_{n\alpha}(\omega)\mathbf{r}_{\alpha\beta} - \mathbf{r}_{n\alpha}\delta U_{\alpha\beta}(\omega)\Big)G^<_{\beta m}(E) + \Big(H_{n\alpha}\mathbf{r}_{\alpha\beta} - \mathbf{r}_{n\alpha}H_{\alpha\beta}\Big)\delta G^<_{\beta m}(E)\Big).$$

The spatial representation $\delta\mathbf{j}(\mathbf{r},\omega)$ is obtained with Eq. (1.37).

1.9 SELF-ENERGY EXAMPLES

The exact evaluation of the self-energies Σ requires the solution of the infinite hierarchy of equations in Eq. (1.3). Thus, we have to rely on approximation schemes to calculate real systems. A natural approach is to retain the single-particle picture and to assume that each particle moves in a potential that arises from all other particles. As a first-order approximation, we can keep first-order contributions to the self-energy Σ only. However, this includes already the summation over an infinite class of Feynman's diagrams [Dan84]. Thus, any higher-order approximations for the self-energies also lead to an infinite hierarchy of equations.

Taking into account only first-order contributions for the self-energies is known as the self-consistent first-order Born approximation. The term self-consistent means that the Green's functions determine the self-energies and at the same time the self-energies determine the Green's functions. This self-consistent approximation conserves macroscopic conservation laws such as e. g. particle number conservation and current conservation [KB62].

1.9.1 *Carrier–Carrier interaction*

A generic scattering Hamiltonian $\hat{V}$ was introduced in Eq. (1.2). The Hamiltonian $\hat{V}_\mathrm{C}$ for carrier–carrier interaction is of a similar form and reads

$$\hat{V}_\mathrm{C}(t) = \frac{1}{2}\int\mathrm{d}\mathbf{r}_1\int\mathrm{d}\mathbf{r}_2\, \hat{\psi}^\dagger_{\mathcal{H}}(\mathbf{r}_1,t)\hat{\psi}^\dagger_{\mathcal{H}}(\mathbf{r}_2,t)V_\mathrm{Cou}(\mathbf{r}_1-\mathbf{r}_2)\hat{\psi}_{\mathcal{H}}(\mathbf{r}_1,t)\hat{\psi}_{\mathcal{H}}(\mathbf{r}_2,t).$$

Here, V_{Cou} is the Coulomb potential

$$V_{\mathrm{Cou}}(\mathbf{r}) = -\frac{e}{4\pi\varepsilon_s\varepsilon_0\ |\mathbf{r}|},$$

where e is the charge of the carriers, ε_0 is the electric vacuum permittivity, and ε_{s} is the static relative permittivity at low frequencies. This Hamiltonian leads to an infinite hierarchy of Green's functions as described in Eq. (1.3). The first three terms are known as Hartree, Fock, and direct collision terms [BK95], where the latter two terms can be described as screened Coulomb interaction [Mat67; BK95; Kub10]. The Hartree term is instantaneous and can be written as a Hartree potential Φ that is the solution of Poisson's equation [Lui07]. Thus, the Hamiltonian describing the Hartree potential reads

$$\begin{aligned} V_{\mathrm{C}}^{\mathrm{Har}}(\mathbf{r},t) &= -i\hbar\int \mathrm{d}\mathbf{r}'\, V(\mathbf{r}-\mathbf{r}')G^{<}(\mathbf{r}',t,\mathbf{r}',t) \\ &= -e\int \mathrm{d}\mathbf{r}'\, \frac{n(\mathbf{r}',t)}{4\pi\varepsilon_s\varepsilon_0\,|\mathbf{r}-\mathbf{r}'|} \\ &= -e\,\Phi(\mathbf{r},t) \end{aligned}$$

Here, we used Eq. (1.29) to substitute the carrier density n. A detailed description for the solution of Poisson's equation is given in Chapter 3.

1.9.2 *Carrier–Phonon interaction*

The Hamiltonian $\hat{V}_{\mathrm{Ph}}$ that describes carrier–phonon interactions can be written as [Mah90]

$$\hat{V}_{\mathrm{Ph}}(t) = \int \mathrm{d}\mathbf{r}\, \hat{\psi}^{\dagger}_{\mathcal{H}}(\mathbf{r},t)\sum_{\mathbf{q}} \exp(i\mathbf{q}\mathbf{r})A(\mathbf{q})\left(\hat{a}_{\mathbf{q}}(t)+\hat{a}^{\dagger}_{-\mathbf{q}}(t)\right)\hat{\psi}_{\mathcal{H}}(\mathbf{r},t), \tag{1.38}$$

where $\hat{a}^{\dagger}_{\mathbf{q}}$ is the creation operator for a phonon in state $\mathbf{q}$ at time t and $\hat{a}_{\mathbf{q}}$ is the annihilation operator for a phonon in state $\mathbf{q}$ and time t. The factor A is the Fröhlich coupling constant for carrier–phonon interactions. Note that different kinds of phonons have different coupling constants $A(\mathbf{q})$.

We can write the carrier–phonon Hamiltonian in Eq. (1.38) as a perturbation series. The zero-order term gives the non-interacting phonon Green's function $D_{\mathbf{q}}$. Analogously to the electron–electron interaction, the two lowest-order terms are referred to as Hartree and Fock term. However, the first-order Hartree term vanishes because it contains only single terms of creation and annihilation operators [Mah90].

For the same reason, all odd-order terms vanish since their time-ordered expectation values contain an odd number of creation and annihilation operators [Pou07]. Thus, only even-order terms contribute to the perturbation expansion. With the usual commutation rules for bosons [Mah90] and using Wick's decomposition [FW71], we can write the lowest, second-order carrier–phonon self-energy as [LD92; Wac02b; SW02]

$$\Sigma_{\mathrm{Ph}}(\mathbf{1},\mathbf{2}) = i\hbar \sum_{\mathbf{q}} |A(\mathbf{q})|^2 \, e^{i\mathbf{q}(\mathbf{r}_1-\mathbf{r}_2)} \, D_{\mathbf{q}}(t_1,t_2) \, G(\mathbf{1},\mathbf{2}),$$

with the free, non-interacting phonon Green's function $D_{\mathbf{q}}$, that reads

$$D_{\mathbf{q}}(t,t') = -\frac{i}{\hbar} \left\langle T\left\{ \hat{a}_{\mathbf{q}}(t)\hat{a}^{\dagger}_{\mathbf{q}}(t') + \hat{a}^{\dagger}_{-\mathbf{q}}(t)\hat{a}_{-\mathbf{q}}(t') \right\} \right\rangle .$$

We can derive the retarded and lesser carrier–phonon self-energies with Langreth's theorem from Eq. (1.10) and Eq. (1.11). The steady-state equations are obtained with a Fourier transformation. Thus, the retarded self-energy reads

$$\begin{aligned}\Sigma^{R}_{\mathrm{Ph}}(\mathbf{r}_1,\mathbf{r}_2,E) = \frac{i}{2\pi} \sum_{\mathbf{q}} |A(\mathbf{q})|^2 \, e^{i\mathbf{q}(\mathbf{r}_1-\mathbf{r}_2)} \int \mathrm{d}E' \Big(& D^{R}_{\mathbf{q}}(E') \, G^{<}(\mathbf{r}_1,\mathbf{r}_2,E-E') \\ & + \Big(D^{R}_{\mathbf{q}}(E') + D^{<}_{\mathbf{q}}(E') \Big) G^{R}(\mathbf{r}_1,\mathbf{r}_2,E-E') \Big),\end{aligned}$$

whereas the lesser self-energy reads

$$\Sigma^{<}_{\mathrm{Ph}}(\mathbf{r}_1,\mathbf{r}_2,E) = \frac{i}{2\pi} \sum_{\mathbf{q}} |A(\mathbf{q})|^2 \, e^{i\mathbf{q}(\mathbf{r}_1-\mathbf{r}_2)} \int \mathrm{d}E' \, D^{<}_{\mathbf{q}}(E') \, G^{<}(\mathbf{r}_1,\mathbf{r}_2,E-E').$$

For a self-consistent solution of the carrier-phonon self-energies, Dyson's equation for the phonon Green's function $D_{\mathbf{q}}$ has to be solved. Especially, when the system is far away from equilibrium the carriers strongly interact with the phonons [Lug+87; RSE04] and thus, the explicit calculation of the phonon Green's functions is crucial [Laz+05; Asa08]. However, a heat up of the phonon bath can be successfully modeled by an increased lattice temperature [Vit+05; Wil+03]. Thus, a more convenient approach in terms of numerical efficiency is to assume the phonon bath to be in thermal equilibrium. Hence, we can write the free phonon Green's function as [Kub10]

$$\begin{aligned} D^{R}_{\mathbf{q}}(E) &= \Big(E - E_{\mathbf{q}} - i\eta \Big)^{-1} - \Big(E - E_{\mathbf{q}} + i\eta \Big)^{-1}, \\ D^{<}_{\mathbf{q}}(E) &= -2i\pi \Big((N_{\mathbf{q}}+1) \, \delta(E+E_{\mathbf{q}}) - N_{\mathbf{q}} \, \delta(E-E_{\mathbf{q}}) \Big), \end{aligned}$$

where η is an infinitesimal small, positive constant, $N_{\mathbf{q}}$ is the Bose distribution for the phonons and $E_{\mathbf{q}} = \hbar\omega(\mathbf{q})$ is the energy of a phonon with frequency $\omega(\mathbf{q})$. Finally, with the help of the residue theorem and the following identity

$$\frac{1}{x - i\eta} = -i\pi\,\delta(x) + \mathcal{P}\frac{1}{x},$$

where $\mathcal{P}$ is the principle part, we can write the steady-state retarded and advanced phonon self-energy as

$$\begin{aligned}\Sigma^{R/A}_{\mathrm{Ph}}(\mathbf{r}_1, \mathbf{r}_2, E) = \sum_{\mathbf{q}} |A(\mathbf{q})|^2 \exp\Big(i\mathbf{q}(\mathbf{r}_1 - \mathbf{r}_2)\Big) \\ \times \Bigg((1 + N_{\mathbf{q}}) G^{R/A}(\mathbf{r}_1, \mathbf{r}_2, E - E_{\mathbf{q}}) + N_{\mathbf{q}} G^{R/A}(\mathbf{r}_1, \mathbf{r}_2, E + E_{\mathbf{q}}) \\ + \frac{1}{2}\Big(G^{<}(\mathbf{r}_1, \mathbf{r}_2, E - E_{\mathbf{q}}) - G^{<}(\mathbf{r}_1, \mathbf{r}_2, E + E_{\mathbf{q}}) \Big) \\ + i\mathcal{P}\int \frac{dE'}{2\pi} \frac{G^{<}(\mathbf{r}_1, \mathbf{r}_2, E - E')}{E' - E_{\mathbf{q}}} - \frac{G^{<}(\mathbf{r}_1, \mathbf{r}_2, E - E')}{E' + E_{\mathbf{q}}} \Bigg),\end{aligned} \tag{1.39}$$

and the steady-state lesser phonon self-energy reads

$$\begin{aligned}\Sigma^{<}_{\mathrm{Ph}}(\mathbf{r}_1, \mathbf{r}_2, E) = \sum_{\mathbf{q}} |A(\mathbf{q})|^2 \exp\Big(i\mathbf{q}(\mathbf{r}_1 - \mathbf{r}_2)\Big) \\ \times \Big(N_{\mathbf{q}} G^{<}(\mathbf{r}_1, \mathbf{r}_2, E - E_{\mathbf{q}}) + (1 + N_{\mathbf{q}}) G^{<}(\mathbf{r}_1, \mathbf{r}_2, E + E_{\mathbf{q}}) \Big).\end{aligned} \tag{1.40}$$

Note, that the principle part integral in Eq. (1.39) is in general very small and due to its imaginary prefactor it introduces only a very small shift of resonant phonon states but does not alter the scattering rates significantly [Fre10; Kub10]. Thus, to reduce the numerical effort, this principle part integral is often neglected [LD92; LW02; Kub10].

1.9.2.1 *Optical phonon interaction*

The scattering on lattice vibrations of polar materials was studied by H. Fröhlich in Ref. [Frö54]. A detailed derivation of the Fröhlich coupling constant A_{OP} for optical phonon scattering can be found e. g. in Ref. [Rid82] and Ref. [Mah90] as well as in the original work of H. Fröhlich [Frö54]. The result for the longitudinal polar optical phonon coupling constant reads

$$|A_{\mathrm{OP}}(\mathbf{q})|^2 = \frac{e^2 E_{\mathrm{OP}}(\mathbf{q})}{2\varepsilon_0} \left(\frac{1}{\varepsilon_\infty} - \frac{1}{\varepsilon_s}\right) \left(\frac{\mathbf{q}}{\mathbf{q}^2 + \xi^{-2}}\right)^2,$$

where e is the charge of the carriers, ξ is the Debye screening length, ε_0 is the electric vacuum permittivity, ε_∞ is the relative electric permittivity at the high frequency limit, ε_s is the relative static low frequency permittivity, and E_{OP} is the energy of the optical phonons.

We have to apply further numerical approximations to be able to calculate the self-consistent optical phonon self-energy within the non-equilibrium Green's function formalism on state-of-the-art hardware [Kub10]. Thus, we approximate the dispersion relation of the optical phonons $E_{\mathrm{OP}}(\mathbf{q}) = E_{\mathrm{OP}}$ as well as the phonon distribution $N_{\mathbf{q}} = N_{\mathrm{OP}}$ at a given temperature T to be constant [Kub10]

$$N_{\mathrm{OP}} = \left(\exp\left(\frac{E_{\mathrm{OP}}}{k_B T}\right) - 1\right)^{-1},$$

where k_B is Boltzmann's constant.

1.9.2.2 *Acoustic phonon interaction*

We assume that the influence of the geometry of the system on the acoustic phonons is negligible. Especially, we neglect any effects of phonon confinement, because it can be shown that these effects are small unless the extent of the system comes to the atomic length scale, e. g. in carbon–nanotubes or molecules [MA89; GBK08]. Thus, we assume thermally distributed bulk phonons [Kub10]. With the deformation potential method [BS50], we can derive the Fröhlich coupling constant for acoustic phonon scattering. It reads [Lak+97; Kub10]

$$|A_{\mathrm{AP}}(\mathbf{q})|^2 = \frac{\hbar^2 V_D^2\, \mathbf{q}^2}{2\rho_M E_{\mathrm{AP}}(\mathbf{q})},$$

where V_D is the scalar deformation potential, ρ_M is the density of the material, and E_{AP} is the energy of acoustic phonons. Unlike the carrier–optical-phonon scattering self-energy, the self-energy for the carrier–acoustic-phonon scattering can be simplified efficiently due to the low acoustic phonon energies. A first step is to linearize the acoustic phonon dispersion [JL89]

$$E_{\mathrm{AP}}(\mathbf{q}) = \hbar\omega(\mathbf{q}) \approx v_s \left|\mathbf{q}\right|,$$

where v_s is the velocity of sound in the material. However, this still leads to a very high computational burden since the full three-dimensional integral over the phonon wave vector $\mathbf{q}$ has to be carried out. Hence, a very common approach is to assume

the phonon energy to be small and therefore to ignore the acoustic phonon energies at all [JR83; Lak+97]

$$E \pm E_{\mathrm{AP}}(\mathbf{q}) \approx E.$$

Furthermore, we employ the equipartition approximation [Rid82] and assume high temperatures $k_B T \gg E_{\mathrm{AP}}(\mathbf{q})$, so that the Bose distribution can be approximated by [Kub10]

$$N_{\mathbf{q}} \approx N_{\mathbf{q}} + 1 \approx \frac{k_B T}{\hbar v_s \left|\mathbf{q}\right|}.$$

With these approximations, the retarded and lesser phonon self-energies in Eq. (1.39) and Eq. (1.40) read [Lak+97; Kub10]

$$\Sigma^{R/<}_{\mathrm{AP}}(\mathbf{r}_1, \mathbf{r}_2, E) = \frac{V_D^2 k_B T}{\rho_M v_s^2} \delta(\mathbf{r}_1 - \mathbf{r}_2)\, G^{R/<}(\mathbf{r}_1, \mathbf{r}_2, E). \tag{1.41}$$

This approximation to the scattering self-energy describes only elastic scattering processes. However, such an elastic approximation misses an important physical aspect. Scattering on acoustic phonons provides a way for arbitrary small energy relaxation processes. In particular, when the energy is too small to emit optical phonons, an elastic approximation may underestimate the thermalization of carriers. To remedy this lack of carrier thermalization, we follow Tillmann Kubis in Ref. [Kub10] and replace the Green's functions in Eq. (1.41) with an energy-averaged Green's function over the acoustic phonon range. Finally, the approximated carrier–acoustic-phonon self-energy reads

$$\Sigma^{R/<}_{\mathrm{AP}}(\mathbf{r}_1, \mathbf{r}_2, E) = \frac{V_D^2 k_B T}{2\rho_M v_s^2 E_{\mathrm{AP}}} \delta(\mathbf{r}_1 - \mathbf{r}_2) \int_{E-E_{\mathrm{AP}}}^{E+E_{\mathrm{AP}}} \mathrm{d}E'\, G^{R/<}(\mathbf{r}_1, \mathbf{r}_2, E'), \tag{1.42}$$

where $E_{\mathrm{AP}} = \hbar\omega_D$ is the maximum acoustic phonon energy and ω_D is the Debye frequency.

1.10 THE EFFECTIVE MASS APPROXIMATION

In this section, we present a brief introduction to the effective mass approximation (EMA) which is the underlying model for the calculations throughout this work. Originally, the effective mass approximation was developed by Joaquin Mazdak

Luttinger and Walter Kohn to describe the motion of carriers in the presence of weak perturbations [LK55]. However, due to the growing interest in quantum well structures, the effective mass approximation was refined and adopted for the regime of strong perturbations by Michael Burt [Bur92].

One crucial assumption within the effective mass approximation is that many-body interactions of the carriers are negligible and thus, their motion can be described by a one-particle Hamiltonian. The second cornerstone of the effective mass approximation is the fact that the carriers in a crystal react to electric and magnetic fields almost as if they were particles with a direction-dependent mass, the so-called effective mass. Thus, in general the effective mass is not a scalar but can be expressed as a tensor. Now, the basic idea is that the dispersion relation around a local extrema at $\mathbf{k}_0$ can be approximated to be parabolic by the following series expansion

$$E(\mathbf{k}) = E(\mathbf{k}_0) + \frac{\hbar^2}{2m^*}(\mathbf{k} - \mathbf{k}_0)^2 + \mathcal{O}\Big((\mathbf{k} - \mathbf{k}_0)^3\Big),$$

where E is the energy, $\mathbf{k}$ is the wave vector that is often slackly called momentum, and m^* is the effective mass tensor. In general, the effective mass tensor is of the following form

$$\left(\frac{1}{m^*}\right)_{ij} = \frac{1}{\hbar^2}\frac{\partial^2 E(\mathbf{k})}{\partial k_i \partial k_j},$$

where $\mathbf{k} = (k_x, k_y, k_z)^T$ and consequently $i, j \in \{x, y, z\}$. This implies that the acceleration of carriers within an electric field is not necessarily along the corresponding field vector. Since the dispersion relation is assumed to be parabolic the effective mass approximation is most useful to describe systems where the important and interesting physics takes place at local extrema. Such systems are e. g. semiconductors, where the carrier dynamics can be described at a local minimum of the conduction band as well as a local maximum of the valence bands.

2 OPEN-DEVICE BOUNDARY CONDITIONS

The quantum transport problem can be seen as a carrier scattering problem between reservoirs. Hence, the system of interest must be treated as an open quantum system. A common approach is to divide the quantum system into a device region and several lead regions [Dat95]. The leads are assumed to be homogeneous and in equilibrium and consequently, all relevant scattering processes are assumed to happen inside the device. The device is assumed to have a finite extent in at least one spatial dimension. The other dimensions can be either finite or infinite due to periodic boundary conditions or a mode space description. The leads are assumed to be semi-infinite and connected to a finite dimension of the device as depicted in Fig. 2.1. The interface between the device and the leads is the so-called contact block.

However, even if the actual device region has a finite extent, the total system including the leads is still infinite and a direct solution of the Green's functions involves infinite matrices. In order to solve the quantum transport equations the effects of the coupling to the semi-infinite leads can be folded into the device region and described via a so-called contact self-energy [Dat95]. This additional self-energy incorporates the transitions between the device and the leads. Therewith, the solution of the Green's functions involves only finite matrices of the size of the actual device region.

2.1 SELF-ENERGIES FOR SEMI-INFINITE LEADS

In this section we derive the contact self-energies based on the pioneering approach of Supriyo Datta in Ref. [Dat95]. We start with the discrete form of Dyson's equation from Eq. (1.24) in a symbolic matrix notation. For a clear and compact notation, we

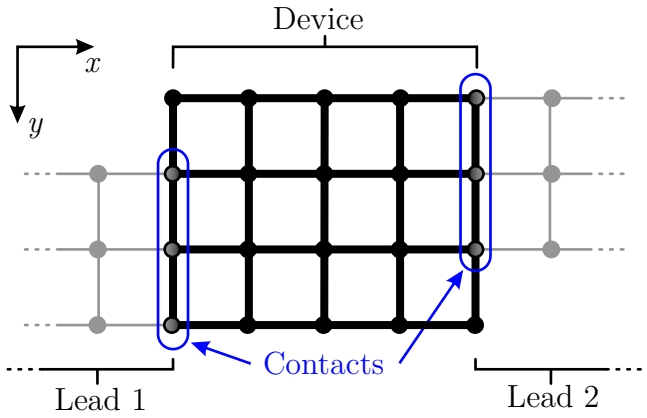

Figure 2.1: Schematic sketch of a two-dimensional device. Each node on the discrete lattice represents a basis function $\phi_n(\mathbf{r})$ as introduced in Sec. 1.6. The actual finite device is drawn bold and black. The semi-infinite leads are labeled with "Lead 1" and "Lead 2". They are shown in gray and the corresponding contact blocks are marked in blue.

omit the matrix indexes. Thus, the symbolic matrix equation reads

$$\begin{pmatrix} E\mathcal{S} - H_L - \Sigma_L^R(E) & -W_{LD}(E) \\ -W_{DL}(E) & E\mathcal{S} - H_D - \Sigma_D^R(E) \end{pmatrix} \begin{pmatrix} G_L^R(E) & G_{LD}^R(E) \\ G_{DL}^R(E) & G_D^R(E) \end{pmatrix} = \mathbb{1}, \tag{2.1}$$

where the coupling matrices are $W_{LD}(E) = H_{LD} + \Sigma_{LD}^R(E)$ and $W_{DL}(E) = H_{DL} + \Sigma_{DL}^R(E)$. The self-energy Σ^R includes all scattering processes. The device region is labeled with "D", the lead is labeled with "L", and the coupling matrices between the lead and the device are labeled with "LD" and "DL", respectively. Note that all matrices with a label "L" are semi-infinite. Here, as a template pattern, we assume only one lead. However, the treatment of further leads is strictly analogous.

First, we introduce the semi-infinite retarded Green's function g_L^R of the semi-infinite lead as follows

$$\Big(E\mathcal{S} - H_L - \Sigma_L^R(E)\Big) g_L^R(E) = \mathbb{1}. \tag{2.2}$$

Note that the Hamiltonian H_L as well as the self-energy Σ_L^R consist of homogeneous contact block layers along the semi-infinite dimension of the lead. This is due to the fact that the lead is assumed to be homogeneous and all relevant processes happen inside the device. In Fig. 2.1 the semi-infinite dimension of the leads is the x-direction.

Now, we insert Eq. (2.2) into the system of equations stated by Eq. (2.1). Solving the resulting system of equations for the device Green's function G_D^R leads to the following equation

$$\Big(E\mathcal{S} - H_D - \Sigma_D^R(E) - S^R(E)\Big)G_D^R(E) = \mathbb{1}, \tag{2.3}$$

where the additional boundary self-energy S^R is defined as

$$S^R(E) = W_{DL}(E)\, g_L^R(E)\, W_{LD}(E).$$

Note that due to the rectangular structure of the coupling matrices W_{LD} and W_{DL}, the matrix of the contact self-energy S^R is of the same size as the device related matrices labeled with "D".

With the help of the fluctuation–dissipation theorem from Eq. (1.20) and Eq. (1.21), we are able to calculate the lesser self-energy $S^<$ of the contacts. The application of the fluctuation–dissipation theorem is well justified, since we assume the leads to be in equilibrium. Thus, the lesser contact self-energy reads

$$S^<(E) = i\, f(E)\Big(S^R(E) - S^{R\dagger}(E)\Big), \tag{2.4}$$

where f is the distribution function of the lead.

The structure of the contact self-energies S is mainly sparse if we only consider nearest-neighbor couplings. Furthermore, due to this sparsity structure, we only need to calculate the surface Green's function $g_{L,0}^R$ of the semi-infinite lead. Here, the notation $g_{L,i}^R$ denotes the i^{th} layer of the semi-infinite lead. Since the leads are homogeneous, the surface Green's functions $g_{L,i}^R$ are translationally invariant. Hence, we can set up a recursive equation for $g_{L,0}^R$ similar to Eq. (2.3) [Ven+02]. Thus, the defining equation for the surface Green's function of a lead reads

$$\Big(E\mathcal{S} - H_{L,0} - \Sigma_{L,0}^R(E) - W_{DL,0}(E)\, g_{L,0}^R(E)\, W_{LD,0}(E)\Big)g_{L,0}^R(E) = \mathbb{1}. \tag{2.5}$$

Note that in general the scattering self-energies are not restricted to nearest-neighbor couplings. However, the arguments leading to Eq. (2.5) still remain valid if we consider blocks of layers instead of single layers only. Therefore, each block of layers consists of k layers if we consider k-nearest-neighbor couplings.

The recursive nature of Eq. (2.5) requires an iterative solution scheme. However, a straight forward iteration of Eq. (2.5) is extremely slow convergent [DWS79; LJ81a; LJ81b], especially when the energy E is near singularities. In the next section we present an extended iterative solution scheme that enhances the convergence exponentially [SSR84; SSR85]. Note that an analytic solution for Eq. (2.5) exists for one-dimensional leads with nearest-neighbor coupling and next-nearest-neighbor coupling [Gre08].

2.2 EXTENDED ITERATIVE SOLUTION SCHEME

In this section we present an extended iterative solution scheme for the surface Green's functions of the leads and the contact self-energies. Here, we follow the derivation of M. Pilar Lopez Sancho, Jose Maria Lopez Sancho, and Jaime Rubio in Ref. [SSR84] and Ref. [SSR85] for the calculation of transfer matrices. After n iteration steps already 2^n layers are taken into account instead of only n layers through the direct iteration of Eq. (2.5). This quick, iterative scheme is also known as Sancho–Rubio scheme. Throughout this section, we omit the energy parameter E, the label "L" indicating the lead, and the superscript R indicating the retarded Green's function. Thus, we use the following abbreviations to keep the notation compact

$$\begin{aligned} g(i) &\equiv g^R_{L,i}(E), \\ B &\equiv E\mathcal{S} - H_{L,0} - \Sigma^R_{L,0}(E), \\ W &\equiv W_{DL,0}(E), \\ \tilde{W} &\equiv W_{LD,0}(E), \end{aligned}$$

with the block–layer notation introduced in the previous section. Note that B, W, and $\tilde{W}$ do not need any layer index, since they are the same for each layer due to the homogeneity of the lead.

Similar to Eq. (2.1), we can express the defining equation for the total lead Green's function g^R_L in Eq. (2.2) as symbolic matrix equation. We consider the resulting system of equations in a block–layer notation and therefore, the chain of equations reads

$$\begin{aligned} B\, g(0) &= \mathbb{1} + W\, g(1), \\ B\, g(1) &= W\, g(0) + \tilde{W}\, g(2), \\ &\vdots \\ B\, g(n) &= W\, g(n-1) + \tilde{W}\, g(n+1), \end{aligned} \tag{2.6}$$

where $g(0)$ denotes the surface Green's function of the lead. For $n \geq 1$ these equations can be rewritten as

$$\begin{aligned} g(n) &= B^{-1}\Big(W\, g(n-1) + \tilde{W}\, g(n+1)\Big) \\ &= t_0\, g(n-1) + \tilde{t}_0\, g(n+1), \end{aligned} \tag{2.7}$$

where the abbreviations t_0 and $\tilde{t}_0$ were introduced as follows

$$t_0 = B^{-1}\, W,$$
$$\tilde{t}_0 = B^{-1}\, \tilde{W}.$$

If we apply Eq. (2.7) again to $g(n-1)$ and $g(n+1)$ then Eq. (2.7) becomes

$$g(n) = t_0\Big(t_0\, g(n-2) + \tilde{t}_0\, g(n)\Big) + \tilde{t}_0\Big(t_0\, g(n) + \tilde{t}_0\, g(n+2)\Big). \tag{2.8}$$

By solving Eq. (2.8) for $g(n)$ and recursively defining the t_i and $\tilde{t}_i$ for $i \geq 1$ as follows

$$t_i = (\mathbb{1} - t_{i-1}\tilde{t}_{i-1} - \tilde{t}_{i-1}t_{i-1})^{-1}\, t_{i-1}^2,$$
$$\tilde{t}_i = (\mathbb{1} - t_{i-1}\tilde{t}_{i-1} - \tilde{t}_{i-1}t_{i-1})^{-1}\, \tilde{t}_{i-1}^2,$$

we arrive at the general form of Eq. (2.8) that reads

$$g(n) = t_i\, g(n - 2^i) + \tilde{t}_i\, g(n + 2^i).$$

This procedure of reinserting Eq. (2.8) into itself can be repeated until $n = 2^i$. Thus, we obtain the following chain of equations

$$\begin{aligned}
g(1) &= t_0\, g(0) + \tilde{t}_0\, g(2)\\
g(2) &= t_1\, g(0) + \tilde{t}_1\, g(4)\\
g(4) &= t_2\, g(0) + \tilde{t}_2\, g(8)\\
&\vdots\\
g(2^n) &= t_n\, g(0) + \tilde{t}_n\, g(2^{n+1}).
\end{aligned}$$

Therewith, we can especially express $g(1)$ as

$$g(1) = (t_0 + \tilde{t}_0\, t_1 + \cdots + \tilde{t}_0 \ldots \tilde{t}_{n-1}\, t_n) g(0) + \tilde{t}_n\, g(2^{n+1}).$$

Now, we can find an upper bound for n with $|\tilde{t}_n| < \epsilon$ where ϵ is an arbitrarily small number. Thus, the transfer matrix T can be identified with

$$T = t_0 + \lim_{n\to\infty} \sum_{k=1}^{n} t_n \left(\prod_{l=0}^{k} \tilde{t} \right), \tag{2.9}$$

and the following relation holds

$$g(1) = T\, g(0). \tag{2.10}$$

The n^{th} term of Eq. (2.9) gets vanishingly small very rapidly since it incorporates the effects of 2^n layers and thus it is of order 2^{n+1} in $\tilde{W}$. By inserting Eq. (2.10) into Eq. (2.6) and comparing the result to the defining equation of the surface Green's function in Eq. (2.5), we finally obtain

$$S^R = W\,T.$$

Note that within the Sancho–Rubio iteration scheme about six to eight iterations are needed to get a numerically converged result. Near singularities the number of iterations roughly doubles.

3 CALCULATION OF THE HARTREE POTENTIAL

A proper treatment of the carrier–carrier interaction is crucial for the qualitative as well as quantitative prediction of device characteristics [Zah+04]. The perturbation series expansion of the carrier–carrier interaction yields as lowest order term the so-called Hartree potential, as we discussed in Sec. 1.9.1. This Hartree potential can be modeled by a mean field potential $\Phi(\mathbf{r})$ that is the solution of Poisson's equation

$$\varepsilon_0 \nabla \varepsilon_s(\mathbf{r}) \nabla \Phi(\mathbf{r}) = -e\Big(n(\mathbf{r}) - N(\mathbf{r})\Big),$$

where e is the charge of the carriers, ε_0 is the electric vacuum permittivity, ε_s is the static relative permittivity at low frequencies, and n is the carrier density that can be calculated with Eq. (1.30) within the non-equilibrium Green's function formalism. The quantity N accounts for all other, static carrier densities within the device and reads

$$N(\mathbf{r}) = N_\mathrm{D}(\mathbf{r}) - N_\mathrm{A}(\mathbf{r}) + N_\mathrm{P}(\mathbf{r}) + N_\mathrm{C}(\mathbf{r}),$$

where N_D is the ionized donor density, N_A is the ionized acceptor density, N_P is the polarization charge density, and N_C is the density of surface, volume, and additional fixed charges. We will not go into the details of the calculation of N. A comprehensive presentation and discussion of the various models to calculate the different contributions to N can be found in the theses of Tobias Zibold [Zib07] and Stefan Birner [Bir11].

The unique solution of Poisson's equation requires the specification of boundary conditions. In general, the boundary conditions have the following form

$$c_1(\mathbf{r})\ \Phi(\mathbf{r})\Big|_{\mathbf{r}\in D_\mathrm{S}} + c_2(\mathbf{r})\ \nabla_\mathrm{S}\ \Phi(\mathbf{r})\Big|_{\mathbf{r}\in D_\mathrm{S}} = f(\mathbf{r}),$$

where D_S denotes the boundary of the device and ∇_S denotes the directional derivative in the direction normal to the surface D_S that conventionally points outwards. The

quantity f is a given function on the boundary, and c_1 and c_2 are variable coefficients or constants. Two important types of boundary conditions are the so-called Dirichlet boundary condition where $c_2(\mathbf{r}) = 0$ and the so-called Neumann boundary condition where $c_1(\mathbf{r}) = 0$. A third possibility is that Dirichlet conditions hold on part of the boundary and Neumann conditions hold on the remainder. Note that indeed mixed boundary conditions where c_1 and c_2 are both nonzero are also possible.

Within the non-equilibrium Green's function quantum transport framework the Hartree potential Φ determines the Green's functions and thus the carrier density n, whilst at the same time the carrier density determines the Hartree potential via the Poisson's equation. Hence, Poisson's equation and the quantum transport properties have to be solved in an iterative way. However, a direct iteration is not stable and computationally very demanding since during every iteration step all quantum transport equations have to be solved [Tre+97]. Therefore, different solution strategies to stabilize and speed up the iterative solution were invented, e. g. mixing schemes [Pul80].

In this work, we use the so-called predictor–corrector approach [Tre+97]. The predictor–corrector approach is a fast and robust iterative method to obtain a self-consistent solution to the coupled system of quantum transport equations and Poisson's equation [Lak+97]. The main idea behind the predictor–corrector approach is based on first order quantum mechanical perturbation theory. Essentially, we assume that to first order the wave functions and thus the local density of states do not depend on small changes of the Hartree potential Φ. Thus, the changes $\delta\Phi_i$ in consecutive iteration steps i are interpreted as perturbations of energy levels only. Since the relation of n and Φ is governed by a system of integro-differential equations, the crucial part of the predictor–corrector approach is the approximation of the carrier density $n[\Phi]$. This approximation is the so-called predictor density, and it is used to implement an iteration scheme for the self-consistent solution of the Hartree potential. The following semi-classical predictor density was proposed in Ref. [Lak+97]

$$n[\Phi_i](\mathbf{r}) = \left(\frac{m^\star\, k_B T}{2\pi\hbar^2}\right)^{3/2} \mathcal{F}_{1/2}\left(\frac{E_\mathrm{c}(\mathbf{r}) - e\Phi_i(\mathbf{r})}{k_B T}\right), \tag{3.1}$$

where $m^\star$ is the effective mass of the carriers, k_B is Boltzmann's constant, T is the temperature, $\mathcal{F}_j$ is the Fermi–Dirac integral of order j, and E_c is a constant that is a priori unknown and has to be calculated during the outer iteration steps as explained below.

Within the first step of the predictor–corrector scheme, all quantum transport equations have to be solved within the non-equilibrium Green's function framework

using an initial guess for the Hartree potential Φ_0. Then, the constant E_c is calculated by inverting Eq. (3.1) and inserting the previously calculated initial carrier density $n[\Phi_0]$. Now, with the semi-classical approximation of the carrier density n from Eq. (3.1), Poisson's equation becomes a concrete nonlinear equation. It can be solved by minimizing the following functional F with a Newton–Raphson method

$$F_i(\mathbf{r}) = \nabla\varepsilon_0\varepsilon(\mathbf{r})\nabla\Phi_i(\mathbf{r}) + e\Big(n[\Phi_i](\mathbf{r}) - N(\mathbf{r})\Big).$$

For the Newton–Raphson iteration cycle, the corresponding Jacobian J reads

$$J_i(\mathbf{r},\mathbf{r}') = \frac{\partial F_i(\mathbf{r})}{\partial\Phi_i(\mathbf{r}')}. \tag{3.2}$$

Therewith, the new predictor potential $\phi_{i+1}(\mathbf{r})$ can be calculated with

$$\Phi_{i+1}(\mathbf{r}) = \Phi_i(\mathbf{r}) - \int\mathrm{d}\mathbf{r}\; J_i^{-1}(\mathbf{r},\mathbf{r}')\; F_i(\mathbf{r}').$$

Note, that a direct inversion of the Jacobian J is not absolutely necessary. Instead, advanced schemes like the conjugate-gradient (CG) method, its variants like the composite-step-conjugate-gradient (CSCG) method or the biconjugate-gradient (BiCG) method, or e. g. the generalized-minimal-residual (GMRES) method can be used to calculate the predictor potential Φ_{i+1} in each step.

This Newton–Raphson iteration is the so-called inner iteration or predictor iteration, because the dependence of the carrier density n on the potential Φ is approximated with Eq. (3.1). Once the predictor iterations are converged, the new potential Φ is used to calculate the Green's functions and quantum transport properties within the non-equilibrium Green's function formalism again. This step is the so-called corrector step, since the quantum transport equations are solved exactly. After each corrector step the inner predictor iteration cycle is carried out again. This procedure is repeated until the potential Φ and the density n within the corrector steps are converged. A schematic overview of the complete predictor–corrector approach is shown in Fig. 3.1. Note that the converged result of the predictor–corrector scheme is independent of the actual predictor density. However, the number of corrector steps needed to achieve a converged result strongly depends on the choice of an appropriate functional for the predictor density. Indeed, if the predictor density is not well-chosen, a damping factor has to be introduced for the iteration cycle to ensure at least slow convergence.

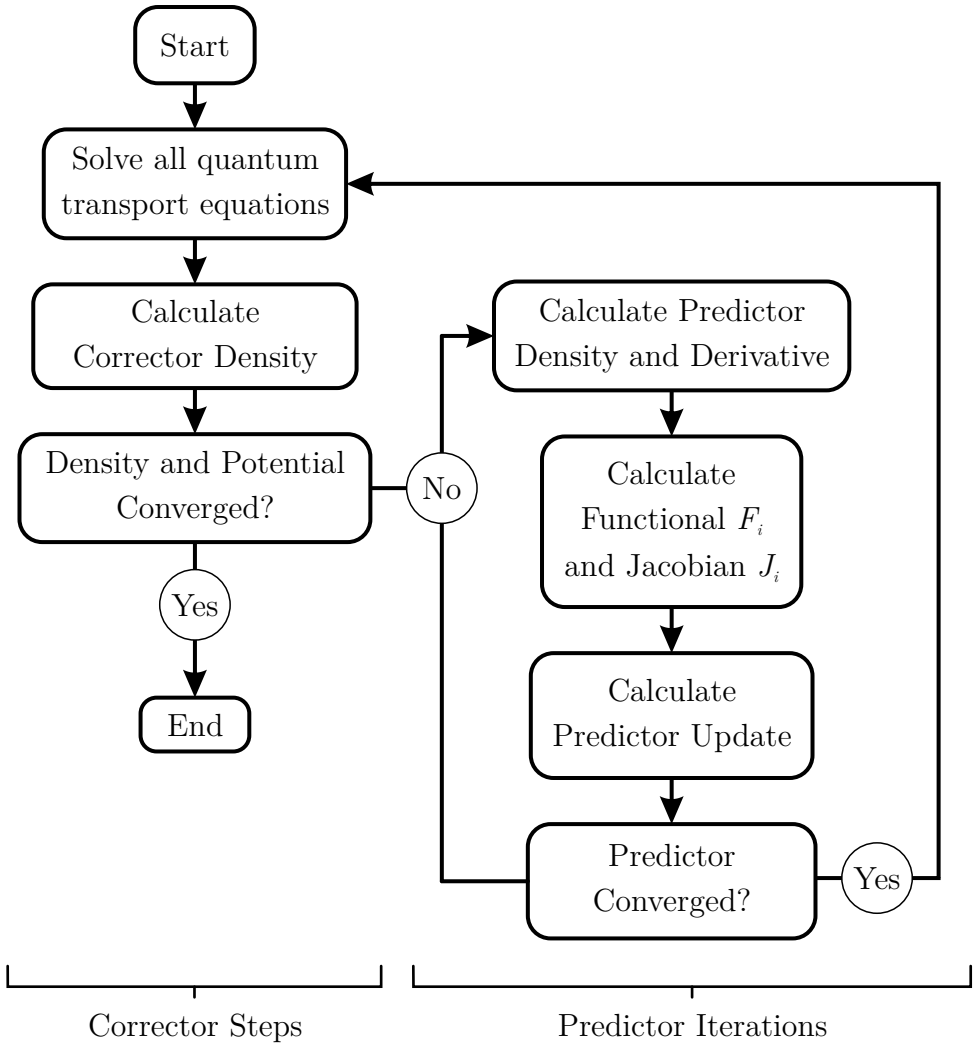

Figure 3.1: Schematic overview of the predictor–corrector approach. In each so-called corrector step all quantum transport equations are solved. During the subsequent predictor iterations an approximation for the carrier density is used to calculate the predictor potential. This procedure is repeated until the carrier density and the potential within the corrector steps has converged.

4 SOLUTION SCHEME OF QUANTUM TRANSPORT EQUATIONS

In this chapter we give a recapitulatory overview of all relevant equations involved in the non-equilibrium Green's function formalism for quantum transport calculations. Especially, we focus on the dependencies and interconnections of the Green's functions and self-energies.

As already pointed out in Chapter 1, the general and rigorous framework of the non-equilibrium Green's function theory can capture the tight interplay between incoherent relaxation processes and quantum interference effects [Kub+09]. Today, it is well established that the non-equilibrium Green's function theory is among the most general schemes for the prediction of quantum transport properties [FJ92; Dat95; Lak+97; AG98; Wac02a].

Unfortunately, the fundamental underlying equations are complex, mathematically tough, and a quantitative implementation is still a highly challenging task, even with the recent advances of modern computer hardware [Cau+11; Zhe+06]. Furthermore, it is very difficult to develop approximations within the non-equilibrium Green's function formalism which maintain charge and current conservation and obey Pauli's principle [KV11]. To obey current conservation laws, e. g. the term R in Eq. (1.32) must vanish exactly. However, R couples the retarded and lesser Green's functions $G^{R,<}$ with the retarded and lesser self-energies $\Sigma^{R,<}$. Thus, any approximation to only one of the aforementioned functions immediately violates current conservation.

However, note that we already employed approximations to derive e. g. the phonon self-energies in Eq. (1.39) and Eq. (1.40). Among these approximations is the assumption that the phonons remain in thermal equilibrium and thus, the phonon Green's function need not to be solved separately. Also, individual approximations such as the high temperature approximation for the acoustic phonon self-energy can be made for specific scattering self-energies. However, a first-order Born or a single Born approximation of the self-energies already violates conservation laws [Kub10]. Hence, the self-energies have to be calculated at least in the self-consistent Born approximation. Furthermore, the tight coupling of the individual integro-differential

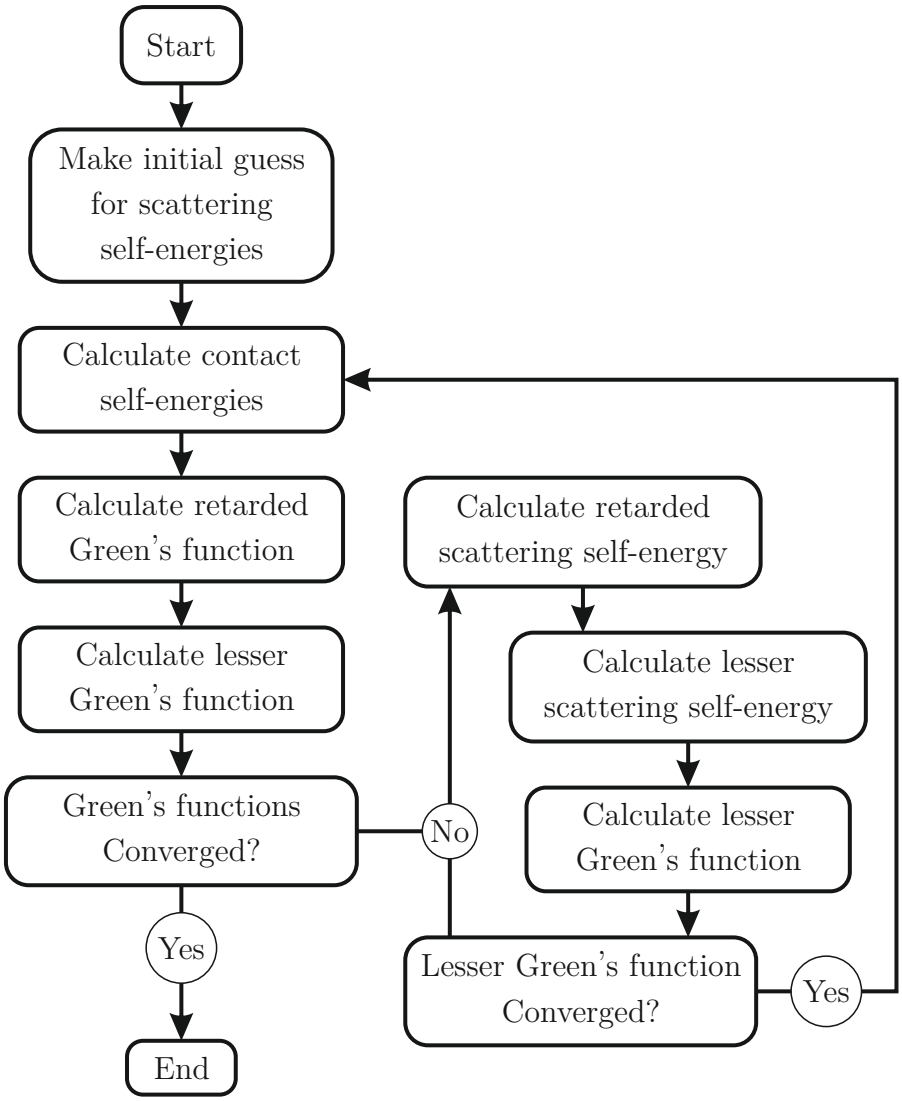

Figure 4.1: Schematic overview of the non-equilibrium Green's function scheme. A direct iteration of all equations converges very slowly since the Green's functions and self-energies are tightly coupled. Better convergence is achieved by iterating the lesser Green's function and lesser self-energy separately. Note that this whole non-equilibrium Green's function scheme is only one part, labeled "Solve quantum transport equations", in the predictor–corrector approach shown in Fig. 3.1.

equations for the Green's functions and scattering self-energies cannot be approximated easily. A straightforward decoupling of these equations immediately leads to a violation of conservation laws [KV11].

The solution scheme for the four coupled integro-differential equations, namely the retarded and lesser Green's functions and the retarded and lesser scattering self-energies, is shown in Fig. 4.1. Additionally, the retarded contact self-energy has to be solved in general for every individual lead that is attached to the device. A summary of the relevant equations using a symbolic matrix notation reads

$$\begin{aligned} G^R &= \big(E\mathcal{S} - H - e\Phi - S^R - \Sigma^R\big)^{-1}, \\ G^< &= G^R\Big(S^< + \Sigma^<\Big)G^{R\dagger}, \\ \Sigma^R &= S^R + G^R D^R + G^R D^< + G^< D^R, \\ \Sigma^< &= S^< + G^< D^<, \end{aligned} \tag{4.1}$$

where $\mathcal{S}$ is the overlap matrix of the basis functions, H is the device Hamiltonian, Φ is the Hartree potential, and Σ^R and $\Sigma^<$ represent the retarded and lesser total scattering self-energy, respectively. The contact self-energies S^R and $S^<$ represent the coupling between leads and the device as discussed in Chapter 2. In a general basis representation $\phi_n(\mathbf{r})$, the defining equation for the retarded contact self-energy reads

$$\sum_{\alpha\in C}\Big(E\mathcal{S}_{n\alpha} - H_{n\alpha} - e\Phi_{n\alpha} - \Sigma^R_{n\alpha}(E) - S^R_{n\alpha}(E)\Big)g^R_{\alpha m}(E) = \delta_{nm} \qquad \forall\, n,m \in C,$$

where C is the set of all nodes that are lying within the contact regions. In Fig. 2.1 the nodes representing the basis functions and the contact regions are depicted schematically. The retarded contact self-energy can be calculated with

$$S^R_{nm}(E) = \sum_{\alpha,\beta} W_{n\alpha}(E)\, g^R_{\alpha\beta}(E)\, W^\dagger_{\beta m}(E),$$

where $W = W_{DL} = W^\dagger_{LD}$ is the coupling matrix between the leads and the device, and g^R is the surface Green's function for the leads. The lesser contact Green's function can be calculated via the fluctuation–dissipation theorem as follows

$$S^<_{nm}(E) = i\, f(E)\Big(S^R_{nm}(E) - S^{R\dagger}_{nm}(E)\Big).$$

The retarded Green's function of the device is defined by the following equation

$$\sum_{\alpha\in D}\Big(E\mathcal{S}_{n\alpha} - H_{n\alpha} - S^R_{n\alpha}(E) - \Sigma^R_{n\alpha}(E)\Big)G^R_{\alpha m} = \delta_{nm} \qquad \forall\, n,m \in D,$$

where D is the set of all nodes within the device region, in analogy to the set C. The lesser Green's function of the device can be calculated with

$$G^<_{nm}(E) = \sum_{\alpha,\beta} G^R_{n\alpha}\Big(S^<_{\alpha\beta}(E) + \Sigma^<_{\alpha\beta}(E)\Big)G^{R\dagger}_{\beta m}.$$

The scattering self-energies Σ^R and $\Sigma^<$ are built up from the sum of all environmental Green's functions D^R and $D^<$ that account for the various scattering mechanisms. For example, the environmental Green's functions D_{Ph} for carrier–phonon scattering are discussed in Sec. 1.9.2.

Note that the four coupled equations in Eq. (4.1) cannot be solved within a direct and robust scheme for realistic devices. In general, during the iterative solution of this tightly coupled system of equations, large damping constants have to be used to grant at least slow convergence. The separate iteration of the lesser branch as shown in Fig. 4.1 results in a slightly improved convergence performance.

5 THE BÜTTIKER–PROBE SCATTERING MODEL

The non-equilibrium Green's function formalism provides a rigorous framework to capture the tight interplay between incoherent relaxation processes and quantum interference effects. Especially, within the NEGF theory the scattering self-energies $\Sigma^{R/A}$ and $\Sigma^{\lessgtr}$ can be calculated from first principles. Thus, the effects of different scattering mechanisms can be investigated qualitatively as well as quantitatively. However, as outlined in Sec. 4, the non-equilibrium Green's function formalism involves tightly coupled integro-differential equations and their numerical treatment is very cumbersome.

In this chapter, we review and discuss the so-called Büttiker-Probe scattering model. It is based on the pioneering work of Markus Büttiker in the 1980s [But86b; But88a]. Until today, the Büttiker–Probe model is widely used for quantum transport calculations [Dat00; Ven+02; Ren+03; Ven+03; IMO07]. The key idea behind this scattering model is an external perturbation of the system. For example, this can be an additional electrode in contact with the device. The effect of this external perturbation on the charge carriers is similar to scattering with phonons. Thus, it seems natural that phonon scattering can be modeled by connecting virtual floating contacts to the device. These floating contacts are the so-called Büttiker–Probes. Within the non-equilibrium Green's function formalism, these probes can be treated in the same way as real contacts, e. g. source and drain. However, the crucial and important difference to real contacts is that the virtual contacts must not carry any current, i. e. the current between the device and all probes must vanish. The physical motivation for this boundary condition is straightforward. Scattering of carriers leads to a redistribution of their energy and momentum while charge and current conservation laws must remain valid. The chemical potential of every additional virtual contact that is attached to the device introduces an additional degree of freedom to the system. These virtual chemical potentials are not determined a priori. Hence, they can be calculated in such a way that current conservation is fulfilled. Thus, scattering events can be viewed as absorption of charge carriers into the

probes and a reinjection of equilibrated charge carriers back into the device. The Büttiker–Probes are assumed to be in a thermodynamic equilibrium, analogously to the real contacts. This is physically motivated by the fact that scattering turns a distorted system back to equilibrium.

To introduce the Büttiker–Probe formalism, we first briefly review the ballistic transport theory within the non-equilibrium Green's function formalism. Thereafter, we present the Büttiker–Probe model and discuss its simplifications and approximations compared to the full non-equilibrium Green's function theory.

5.1 INTRODUCTION TO BALLISTIC TRANSPORT

A system shows ballistic, non-ohmic behavior if its extent is smaller than the characteristic lengths that govern scattering processes. These lengths are on the one hand the mean free path and on the other hand the phase-relaxation length of the carriers [Dat95]. In systems that are smaller than the mean free path, the conductance approaches a classical, ballistic limiting value. However, interference-related effects become important not until the extent of the system becomes smaller than the phase-relaxation length. The order of the mean free path as well as the phase-relaxation length comes to several µm in present day high-mobility semiconductor heterostructures such as modulation doped GaAs/AlGaAs heterojunctions or quantum wells. Thus, ballistic and near-ballistic transport plays an important role in many mesoscopic transport experiments.

A useful theoretical approach to describe ballistic mesoscopic transport was given by Rolf Landauer in the 1980s [Lan88; Lan92]. The generalization of this formalism to multi-terminal devices that eventually led to the Büttiker–Probe model was proposed by Markus Büttiker [Büt86a; Büt88b]. This ballistic transport theory is generally referred to as the Landauer–Büttiker formalism.

Within the non-equilibrium Green's function theory the ballistic limit can be achieved by neglecting all scattering self-energies. This immediately reduces the mathematical and computational effort to calculate the Green's functions tremendously. The retarded Green's function G^R and the lesser Green's function $G^<$ are decoupled since no tedious calculation of the self-energies is required. Thus, within the ballistic limit no self-consistent calculation is required except for the contact self-energies. The numerical calculation of non-equilibrium transport properties in the ballistic limit can even be further simplified. It turns out that is sufficient to calculate the retarded Green's functions G^R_L, G^R_{DL}, and G^R_{LD} from Eq. (2.1) within the contact blocks to describe the ballistic properties of the whole device [Mam+05]. This method is the so-called contact-block-reduction (CBR) method [MSV03; MMV04]. A review

and introduction to the CBR method was given by Stefan Birner in Ref. [Bir+09]. It includes a detailed discussion of the method and its numerical implementation as well as the presentation of numerical results. Note that we do not present and use the CBR method here, since the reduction to the contact block is not possible within the Büttiker–Probe scattering model.

In Chapter 2 we derived the equations that determine the self-energies that describe the coupling of the device to a semi-infinite lead. In general, a finite-dimensional device under non-equilibrium conditions couples to several leads, e. g. to the so-called source and drain. Thus, the total contact self-energy S^R that contains the coupling to all leads is the sum of all individual contact self-energies and reads

$$S^R_{nm}(E) = \sum_{\lambda \in L} S^{R,\lambda}_{nm}(E) \qquad \forall\, n, m \in C, \tag{5.1}$$

where L is the set of all leads and C is the set of all nodes within the contact regions that was introduced in Chapter 2. Since this is the only self-energy that is taken into account, the retarded Green's function of the device is defined by the following equation

$$\sum_{\alpha \in D} \Big(E\mathcal{S}_{n\alpha} - H_{n\alpha} - e\Phi_{n\alpha} - S^R_{n\alpha}(E) \Big) G^R_{\alpha m} = \delta_{nm} \qquad \forall\, n, m \in D, \tag{5.2}$$

where $\mathcal{S}$ is the overlap matrix of the basis functions, H is the non-interacting Hamiltonian that describes the system, Φ is the electrostatic Hartree potential, and D is the set of all nodes within the device region. Note that the inclusion of the Hartree potential Φ does not lead to energy relaxing scattering processes [Dat95]. This is due to the fact that the lowest-order Hartree approximation for the carrier–carrier interaction does not contribute to the lesser and greater self-energies, as discussed in Sec. 1.9.1.

The spectral function associated with the system was defined in Eq. (1.21) and reads

$$\begin{aligned} A_{nm}(E) &= i\Big(G^R_{nm}(E) - G^{R\dagger}_{nm}(E) \Big) \\ &= i \sum_{\alpha,\beta} G^R_{n\alpha}(E) \Big(S^R_{\alpha\beta}(E) - S^{R\dagger}_{\alpha\beta}(E) \Big) G^{R\dagger}_{\beta m}(E), \end{aligned} \tag{5.3}$$

where we used Eq. (5.2) to transform the first line into the second one. By defining the so-called broadening function Γ, we can write the spectral function as follows [Dat95; Dat05]

$$A_{nm}(E) = \sum_{\alpha,\beta} G^R_{n\alpha}(E)\, \Gamma_{\alpha\beta}(E)\, G^{R\dagger}_{\beta m}(E),$$

where the broadening function Γ consequently reads

$$\Gamma_{nm}(E) = i\Big(S^{R}_{nm}(E) - S^{R\dagger}_{nm}(E)\Big). \tag{5.4}$$

With Eq. (5.1) we can assign an individual broadening function to every lead that is attached to the device as follows

$$\Gamma^{\lambda}_{nm}(E) = i\Big(S^{R,\lambda}_{nm}(E) - \Big(S^{R,\lambda}_{nm}(E)\Big)^{\dagger}\Big) \qquad \forall\, \lambda \in L.$$

Analogously, we can define a spectral function with respect to every individual lead by

$$A^{\lambda}_{nm}(E) = \sum_{\alpha,\beta} G^{R}_{n\alpha}(E)\, \Gamma^{\lambda}_{\alpha\beta}(E)\, G^{R\dagger}_{\beta m}(E) \qquad \forall\, \lambda \in L.$$

The fundamental assumption for the leads is that they are and remain in thermal equilibrium, as discussed in Chapter 2. Thus, we can use the fluctuation–dissipation theorem from Eq. (1.20) and therewith, the carrier density from Eq. (1.30) can be calculated within the ballistic quantum transport model as follows

$$n(\mathbf{r}, E) = \frac{1}{2\pi} \sum_{\lambda\in L} \sum_{\alpha,\beta} \phi_{\alpha}(\mathbf{r})\phi^{*}_{\beta}(\mathbf{r})\; f_{\lambda}(E) A^{\lambda}_{\alpha\beta}(E), \tag{5.5}$$

where f_λ is the distribution function of the lead labeled with "λ". The ballistic current that flows through a contact region into a lead can be calculated with the so-called Landauer formula or Landauer–Büttiker formula. Generally, it involves integration over all quantum numbers that characterize the lead states and has been given in its most general form by Aldo Di Carlo, Peter Vogl, and Walter Pötz in Ref. [DCVP94]. Within the non-equilibrium Green's function formalism the Landauer–Büttiker formula can be derived from Eq. (1.33) [Dat95]. Therefore, we first define a general current operator C as follows

$$C(\mathbf{r}, \mathbf{r}', E) = \frac{e}{h}\Big(H_0(\mathbf{r})G^{<}(\mathbf{r}, \mathbf{r}', E) - G^{<}(\mathbf{r}, \mathbf{r}', E)H_0(\mathbf{r}')\Big),$$

where the diagonal elements $C(\mathbf{r}, \mathbf{r}, E) = \nabla j(\mathbf{r}, E)$ correspond to the divergence of the current density from Eq. (1.33). Now, we can rewrite the operator C with Eq. (5.2), Eq. (2.4), and Eq. (1.25) to the following form

$$C = G^{R}S^{<} - S^{<}G^{R\dagger} - S^{R}G^{<} + G^{<}S^{R\dagger},$$

where we omitted the spatial arguments as well as the energy for a cleaner notation. The total current flow through the surface of the device, i. e. through all contact regions, is given by the trace of the current operator [Dat95]

$$\int \mathrm{d}E \int \mathrm{d}\mathbf{r}\, \nabla j(\mathbf{r}, E) = \int \mathrm{d}E\, \mathrm{Tr}\, C(E).$$

The trace of the current operator $\mathrm{Tr}\, C$ can be expressed with Eq. (5.3) and Eq. (5.4) as follows

$$\mathrm{Tr}\, C(E) = \frac{e}{h} \sum_{\alpha,\beta} \Big(S^{<}_{\alpha\beta} A_{\beta\alpha} - \Gamma_{\alpha\beta} G^{<}_{\beta\alpha} \Big).$$

Recalling the definition of the spectral function in Eq. (5.3), the lesser contact self-energy in Eq. (2.4), and the broadening function in Eq. (5.4), we can write the current flowing through the contact region labeled with "c" as follows [Dat95]

$$j_c = \frac{e}{h} \int \mathrm{d}E \sum_{\lambda \in L} \Big(T_{\lambda c}(E) f_\lambda(E) - T_{c\lambda} f_c(E) \Big), \tag{5.6}$$

where T is the so-called transmission function between two leads $\lambda_1 \neq \lambda_2$ and reads

$$T_{\lambda_1 \lambda_2}(E) = \sum_{\alpha,\beta,\mu,\nu} \Gamma^{\lambda_1}_{\alpha\mu}(E)\, G^{R}_{\mu\beta}(E) \Gamma^{\lambda_2}_{\beta\nu}(E)\, G^{R\dagger}_{\nu\alpha}(E).$$

Note that the sum of all currents flowing through the contact regions vanishes

$$\sum_{\lambda \in L} j_\lambda = 0.$$

This equation is automatically obeyed because particle and current conservation laws guarantee in the absence of any scattering mechanisms that there is neither a net carrier generation nor annihilation.

5.2 DISSIPATIVE TRANSPORT WITH BÜTTIKER–PROBES

In the ballistic limit of the non-equilibrium Green's function theory, the carriers do not have the possibility to redistribute their energy and momentum due to scattering events. The basic but seminal idea of Markus Büttiker was to attach an additional virtual contact to the device in analogy to a voltage probe. This additional virtual floating contact acts as an external perturbation of the system, that removes, thermalizes, and reinjects carriers. Thus, it mimics the effects of

scattering via phonons. This Büttiker–Probe model is truly an extremely simple way of taking scattering effects into account. However, this simple model already captures some of the important features of dissipative quantum transport. Furthermore, the Büttiker–Probes can be treated in the same way as real contacts and thus, there are no coupled integro-differential equations to be solved. This lowers the numerical complexity of the Büttiker–Probe model extremely compared to the self-consistent non-equilibrium Green's function method.

Within the Büttiker–Probe model, scattering and particularly the scattering strength is modeled by a phenomenological scattering parameter. The retarded Büttiker–Probe self-energy B^R arising from all probes is the sum of the self-energies of all individual probes

$$B^R(\mathbf{r}, E) = \sum_{\kappa \in P} B^{R,\kappa}(E)\, \delta(\mathbf{r} - \mathbf{r}_\kappa), \tag{5.7}$$

where P is the set of all probes, $B^{R,p}$ is the scattering self-energy for probe p, and $\mathbf{r}_p$ is the position of probe p. A simple yet often used model for the probe self-energy is the relation to a phenomenological scattering parameter as follows

$$B^{R,p}(E) = -\, i\eta_p, \tag{5.8}$$

where η_p is a phenomenological parameter, e. g. $\eta_p = \hbar\tau_p^{-1}$ with τ_p being a spatially varying and thus material dependent scattering time. Note that this is only one out of many possibilities for the scattering self-energy within the Büttiker–Probe model. In Sec. 5.3 we present a model that relates the mean free path to the scattering self-energy. The defining equation for retarded Green's function within the Büttiker-Probe model now reads

$$\sum_\alpha \Big(E\mathcal{S}_{n\alpha} - H_{n\alpha} - e\Phi_{n\alpha} - S^R_{n\alpha}(E) - B^R_{n\alpha}(E) \Big) G^R_{\alpha m} = \delta_{nm} \qquad \forall\, n, m \in D,$$

where $\mathcal{S}$ is the overlap matrix of the basis functions, H is the non-interacting Hamiltonian that describes the system, Φ is the electrostatic Hartree potential, S^R is the self-energy arising from the contacts, and D is the set of all nodes within the device region. Analogously to the real contacts, we can assign a broadening function to every individual probe

$$\Gamma^p_{nm}(E) = i\Big(B^{R,p}_{nm}(E) - \big(B^{R,p}_{nm}(E) \big)^\dagger \Big) \qquad \forall\, n, m \in D,\ \forall\, p \in P.$$

Therewith, we can define the spectral function with respect to every individual probe as follows

$$A^p_{nm}(E) = \sum_{\alpha,\beta} G^R_{n\alpha}(E)\,\Gamma^p_{\alpha\beta}(E)\,G^{R\dagger}_{\beta m}(E) \qquad \forall\, n,m \in D,\ \forall\, p \in P. \tag{5.9}$$

Hence, the carrier density within the Büttiker–Probe model consists of the coherent, ballistic contributions from the real contacts and the non-coherent contributions from the virtual floating probes. It reads as follows

$$n(\mathbf{r},E) = \frac{1}{2\pi}\sum_{\alpha,\beta}\phi_\alpha(\mathbf{r})\left(\sum_{\lambda\in L} f_\lambda(E)A^\lambda_{\alpha\beta}(E) + \sum_{\kappa\in P} f_\kappa(E)A^\kappa_{\alpha\beta}(E)\right)\phi^*_\beta(\mathbf{r}), \tag{5.10}$$

where f_λ are the distribution functions of the real contacts as introduced in Eq. (5.5) and f_κ are the distribution functions of the virtual floating contacts. Associated with each probe p, there is a local chemical potential $\mu(\mathbf{r}_p) \equiv \mu_p$. Analogously to the carrier density, the current flowing through a contact region has an additional non-coherent component arising from the probes. The current density at lead c can be calculated with

$$\begin{aligned} j_c(E) = \frac{e}{h}\Bigg(&\sum_{\lambda\in L}\Big(T_{\lambda c}(E)f_\lambda(E) - T_{c\lambda}f_c(E)\Big) \\ &+ \sum_{\kappa\in P}\Big(T_{\kappa c}(E)f_\kappa(E) - T_{c\kappa}f_c(E)\Big)\Bigg). \end{aligned} \tag{5.11}$$

Note that the spatially resolved current density across the device can still be calculated with Eq. (1.35). Since the fluctuation–dissipation theorem also holds for the Büttiker–Probes, the lesser Green's function $G^<$ can be calculated with Eq. (1.20). Thus, the current density across the device reads

$$\begin{aligned} \mathbf{j}(\mathbf{r},E) = \frac{i\,e\hbar}{4\pi m}\sum_{\alpha\beta}&\Big(\big(\nabla\phi_\alpha(\mathbf{r})\big)\phi^*_\beta(\mathbf{r}) - \phi_\alpha(\mathbf{r})\big(\nabla\phi^*_\beta(\mathbf{r})\big)\Big) \\ &\times\left(\sum_{\lambda\in L} f_\lambda(E)A^\lambda_{\alpha\beta}(E) + \sum_{\kappa\in P} f_\kappa(E)A^\kappa_{\alpha\beta}(E)\right). \end{aligned} \tag{5.12}$$

Within the Büttiker–Probe formalism, the virtual floating probes are treated in exactly the same way as the real contacts. However, unlike the real contacts the probes do not have a well-defined chemical potential. The chemical potentials of the

probes are not fixed by device geometry nor by the applied bias voltage. Instead, these additional degrees of freedom have to be calculated in such a way that current conservation holds. Otherwise, an inflow or outflow of carriers at the probes can occur. To ensure current conservation, the net-current j_p at every probe must vanish

$$\int \mathrm{d}E\, j_p(E) \stackrel{!}{=} 0 \qquad \forall\, p \in P. \tag{5.13}$$

These constraints give a system of nonlinear equations for all virtual chemical potentials μ_p of the probes. In order to calculate the chemical potentials an iterative solution scheme, e. g. the Newton–Raphson method, has to be applied. The functional F that has to be minimized reads

$$F_p^{(i)} = \int \mathrm{d}E\, j_p[\mu_1^{(i)}, \ldots, \mu_{p-1}^{(i)}, \mu_{p+1}^{(i)}, \ldots](E) \qquad \forall\, p \in P,$$

where the virtual chemical potentials during the i^{th} iteration step are labeled $\mu_p^{(i)}$ for all $p \in P$. The corresponding Jacobian matrix within the i^{th} step of the iterative solution procedure can be calculated from Eq. (5.11) as follows

$$J_{pq}^{(i)} = \frac{\partial F_p^{(i)}}{\partial \mu_q^{(i)}} = \begin{cases} -\dfrac{e}{h} \displaystyle\int \mathrm{d}E\, \frac{\partial f_q(E)}{\partial \mu_q^{(i)}} \sum_{\nu \in L \cup P} T_{p\nu}(E) & \text{for } p = q \\[2ex] \dfrac{e}{h} \displaystyle\int \mathrm{d}E\, \frac{\partial f_q(E)}{\partial \mu_p^{(i)}} T_{qp}(E) & \text{for } p \neq q \end{cases},$$

Within each step, the new chemical potentials of the probes can be calculated with

$$\mu_p^{(i+1)} = \mu_p^{(i)} - \sum_{\kappa \in P} \left(J_{p\kappa}^{(i)}\right)^{-1} F_\kappa^{(i)}. \tag{5.14}$$

This procedure is continued until the constraints in Eq. (5.13) are satisfied. Note that the convergence behavior of this system of nonlinear equations can change dramatically depending on the device geometry, the position of the Büttiker-Probes, and the applied bias voltage of the real contacts. Especially, the initial values of the chemical potentials must be well-chosen. Otherwise, the nonlinear system may not converge at all.

5.3 RELATION TO THE MEAN FREE PATH

In this section we present a simple model that relates the phenomenological scattering parameter with the mean free path of the carriers. Therefore, we consider a one-dimensional lattice that is depicted schematically in Fig. 5.1. Since the Büttiker–Probes can be viewed as additional floating contacts, we can assume the scattering

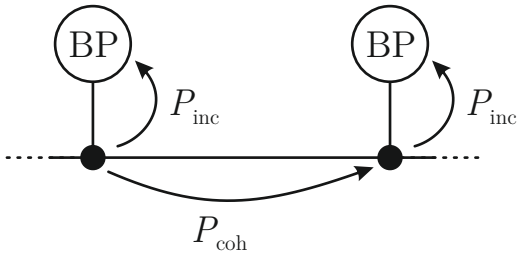

Figure 5.1: Schematic drawing of a one-dimensional lattice where a Büttiker-Probe labeled "BP" is attached to each node, indicated by a full black circle. P_{coh} is the probability that a carrier is transmitted coherently from one node to the next, i. e. without being scattered. The probability that the transport is incoherent is P_{inc}.

self-energy of the probes to be of the following form

$$B^{R,p}(E) = \eta\, S^R(E),$$

where η is a dimensionless scattering parameter and S^R is a self-energy that describes the coupling to a one-dimensional lead. Thus, the probabilities P_{coh} for coherent transport and P_{inc} for incoherent transport are given by

$$P_{\mathrm{coh}} = \frac{1}{1+\eta}, \qquad P_{\mathrm{inc}} = \frac{\eta}{1+\eta}.$$

In the limit $\eta \to 0$ the transport is fully coherent and thus the ballistic limit is reached, since the probability for a scattering event is zero. On the other hand, the limit $\eta \to \infty$ is the diffusive limit, since the probability for coherent transport is zero. Now, we consider N consecutive nodes where a probe is attached to each node. The probability $P_{\mathrm{coh}}(N)$ of a carrier to coherently traverse all N nodes without being scattered can be calculated as

$$P_{\mathrm{coh}}(N) = \left(1 - P_{\mathrm{inc}}\right)^N = \left(\frac{1}{1+\eta}\right)^N. \tag{5.15}$$

If we assume a constant lattice spacing Δ between the nodes, we can define the mean free path $R_{\mathrm{m}} = \Delta\, N_{\mathrm{m}}$ in such a way that the following relation holds

$$P_{\mathrm{coh}}(N_{\mathrm{m}}) = \frac{1}{e}, \tag{5.16}$$

where e is Euler's number. With Eq. (5.15) together with Eq. (5.16), we get the relation between the mean free path R_m and the dimensionless scattering parameter η as follows

$$R_\mathrm{m} = \frac{\Delta}{\ln(1+\eta)} \approx \frac{\Delta}{\eta} \qquad \Leftrightarrow \qquad \eta = e^{\Delta/R_\mathrm{m}} - 1 \approx \frac{\Delta}{R_\mathrm{m}}. \tag{5.17}$$

The simple first-order approximations are valid for near ballistic transport where $\eta \ll 1$ holds. Numerically, we find exact agreement with Eq. (5.17) for a one-dimensional lattice. For the quasi-one-dimensional quantum wire, the agreement is not exact, but reasonable, with a weak dependence on the energy and the wire subband.

5.4 SUMMARY AND ASSESSMENT

In this chapter we introduced and reviewed the so-called Büttiker–Probe model that is based on the analogy of scattering and an external perturbation. It uses a phenomenological parameter to describe scattering via floating virtual contacts. The Büttiker–Probe model provides a link between purely ballistic quantum transport and drift–diffusion like transport. Its main advantage is the low cost in terms of computational effort that comes form the decoupling of the Green's functions while only one self-consistency loop for the chemical potentials is needed. However, the Büttiker–Probe model suffers from some serious disadvantages. The main disadvantage is that it does not capture effects of different scattering mechanisms, but takes a scattering probability or a mean free path as input parameter. Thus, neither the importance nor the quantitative effects of individual scattering mechanisms can be estimated within the Büttiker–Probe model. Nevertheless, it provides a numerically easy way to get some insight to the principle physics of near ballistic devices.

In the next part, we present a novel method for quantum transport calculations that is based on the Büttiker–Probe model, but incorporates the scattering self-energies of the non-equilibrium Green's function theory. Therewith, it is possible to make quantitative calculations whilst principally retaining the numerical efficiency of the Büttiker–Probe model.

Part II

NOVEL METHOD FOR QUANTUM TRANSPORT CALCULATIONS

6 EXISTING METHODS FOR TRANSPORT CALCULATIONS

In this chapter, we give a brief overview of the various existing methods to calculate quantum transport properties. After shortly reviewing the semi-classical and quantum ballistic methods, we present some established techniques to calculate dissipative quantum transport. In particular, we focus on the efficiency of the individual methods in terms of computational costs and the timely calculation of transport properties.

During the rise of the semiconductor technology it was sufficient to estimate the electrical characteristics with some simple analytic models [GS04]. The use of several simplifying approximations still captured the underlying basic physical foundation of carrier transport. Mainly due to the seminal work of Scharfetter and Gummel [SG69], computer programs could be used to get a deeper insight to device physics as well as to design novel scaled-down device types. Thus, not only global quantities but also the internal distribution of device-related physical quantities were accessible.

Since then it was sufficient to describe the current within the device by the electric field and the carrier density gradient. It was natural to neglect the quantum mechanical nature of the carriers and describe the device by Boltzmann's transport equation. The assumption of a cold Maxwell distribution and the restriction to second moments led to the so-called drift–diffusion formalism [GS04]. The drift–diffusion model was and is still a very successful method to calculate semiconductor device properties, since an efficient and robust implementation within a device simulator is possible. Even two-dimensional and three-dimensional structures can be studied with a moderate computational burden [Sab+02; Tre+06].

However, the ongoing decrease in size of semiconductor devices made it necessary to take quantum mechanical effects into account. A direct approach to get access to ballistic quantum transport properties is to calculate the S-matrix via Schrödinger's equation. Thereby, a widely used method is the so-called transfer matrix method [SC83] that was generalized to multi-dimensional systems by Frensley [Fre90] and Lent [LK90], and to multi-band Hamiltonians by Ting [TYM92]. A prerequisite for the transfer matrix method is, however, that scattering boundary conditions

are imposed e. g. by the so-called quantum transmitting boundary method [LK90]. Unfortunately, these boundary conditions implicate a huge computational burden. Thus, these methods are still limited to low-dimensional devices and mostly single-band calculations.

A popular all-inclusive device simulation software suite is e. g. the next**nano** software package [Tre+06; Bir+07]. This simulation tool focuses on quantum mechanical properties such as the global electronic structure, optical properties, and the effects of electric and magnetic fields for virtually any geometry and combination of semiconducting materials. The calculation of carrier dynamics provides results for the limiting cases of highly diffusive transport within a quantum drift–diffusion (QDD) model, or purely ballistic quantum-mechanical transport within the contact block reduction (CBR) method.

However, neither of these two limiting cases can treat scattering and quantum interference effects on an equal footing. For this so-called dissipative quantum transport regime where the tight interplay between incoherent energy relaxation processes and quantum interference effects is crucial, the following well-established techniques have been developed. These methods can be characterized by the underlying functions on which they are based, namely among others the density matrix $\rho(\mathbf{r}, t, \mathbf{r}', t')$, the Wigner function $f_{\mathrm{W}}(\mathbf{r}, \mathbf{p}, t)$, and the non-equilibrium Green's function $G(\mathbf{r}, t, \mathbf{r}', t')$, where $\mathbf{r}$ is the spatial position, $\mathbf{p}$ is the momentum, and t is the time parameter. Thereby, the fundamental equations of motion for all three approaches are equivalent in a formal way. In this work, we concentrate on the non-equilibrium Green's function approach, since it is a well developed theory and provides a consistent and complete way of describing dissipative quantum transport properties of semiconductor nanostructures. However, the resulting coupled integro-differential equations, that are discussed in detail in Chapter 4, are almost always far too complex for realistic devices to be treated in a direct numerical fashion. For example, the Green's functions $G(\mathbf{r}, t, \mathbf{r}', t')$ depend on four variables, two spatial coordinates $\mathbf{r}$ and $\mathbf{r}'$, and two times t and t'. For a numerical calculation all parameters have to be discretized, as discussed in Sec. 1.6. If we assume a very moderate number of 100 nodes for each spatial dimension, $N_x = N_y = N_z = 100$, as well as for each temporal parameter $N_t = 100$, the total number of degrees of freedom N is

$$N = \left(N_x \cdot N_y \cdot N_z \cdot N_t\right)^2 = 10^{16}.$$

Even in the case of stationary transport problems, where we have to deal only with one energy parameter instead of two time parameters, the total number of unknowns is still $N = 10^{14}$. To illustrate this extraordinary large number in terms of memory

consumption, the needed storage capacity for one Green's function would be about 1455 terabytes. Bearing in mind that the usual storage capacity of a single hard disk nowadays is about 1 terabyte, it becomes obvious that not only the self-consistent iterative calculation but even the storage of the discretized Green's functions is far beyond the computational possibilities of a state-of-the-art workstation. Thus, if at all, a general three-dimensional approach within a fully self-consistent non-equilibrium Green's function formalism can only be realized on a super-compute-cluster.

On the other hand, if it is possible to make use of special device characteristics, as for example layered heterostructures, we can lower the computational effort tremendously. Hence, we consider stationary transport for a layered heterostructure and employ the quasi-one-dimensional basis that is discussed in Sec. 1.6. Thus, the total number of unknowns reduces to

$$N = N_z^2 \cdot N_k \cdot N_E = 10^8.$$

Here, we assumed again 100 grid nodes for the growth direction $N_z = 100$ as well as for the energy and lateral momentum domains $N_k = N_E = 100$. Therefore, the needed storage space reduces to about 1.5 gigabytes per Green's function. However, note that as few as 100 grid nodes especially for the energy and momentum domain is extremely coarse. Even higher numerical resolutions require very advanced adaptive discretization schemes to get a converged solution [Kub10]. Although the memory consumption is numerically tractable, the computation time is still a limiting factor since it is of the order of days.

Altogether, the calculation of dissipative quantum transport properties is still a challenging task, despite the fact that there was a great variety of different methods developed in the past decades. Even for layered heterostructures that can be discretized within a quasi-one-dimensional basis, the calculation within a fully self-consistent non-equilibrium Green's functions method is limited to some small selected devices due to excessive memory consumption and immense calculation times.

Although there are models for specific devices that utilize certain device peculiarities, a calculation method especially for engineering applications should be general purpose and not limited to specific geometries or particular classes of devices [GS04]. The fear of losing physical details sometimes leads to the utilization of complicated and numerically very demanding approaches. However, physical models must be simple and efficient whilst at the same time they must retain as much accuracy as possible. In applications, timely results and the possibility to vary parameters quickly are in most cases preferable than over-accurate details [GS04]. In the next chapters

where we present a novel method for quantum transport calculations that is based on a simplified version of the fully self-consistent non-equilibrium Green's function method. This novel method enables applications to quickly sweep several parameters and thus, it can be used in rapid device design processes.

7 THE NOVEL MULTI-SCATTERING BÜTTIKER–PROBE METHOD

In this chapter, we present a novel method to efficiently calculate stationary quantum transport properties in the dissipative regime. We termed this method the multi-scattering Büttiker–Probe (MSB) method. It generalizes the Büttiker–Probe model that is reviewed in Chapter 5 and accounts for relevant individual scattering mechanisms analogously to the self-consistent non-equilibrium Green's functions formalism. Since the MSB method is based on the Büttiker–Probe approach, current conservation is ensured by the same means. Thus, this novel method is orders of magnitude more efficient than a fully self-consistent non-equilibrium Green's function calculation for realistic devices, yet accurately reproduces the results of the latter method. Furthermore, this method is fairly easy to implement and opens the path towards realistic three-dimensional quantum transport calculations.

This chapter is organized as follows. In Sec. 7.1, we present the basic idea of the novel multi-scattering Büttiker–Probe method. Then, in Sec. 7.2, we introduce a novel type of Büttiker–Probes especially for devices with only two current-carrying contacts that bypasses the iterative solution for the virtual chemical potentials. Such devices are e. g. quantum cascade lasers or MOSFETs, if the small gate-leakage currents are neglected. In Sec. 7.3, we show that the MSB method can be easily incorporated within a predictor–corrector scheme for an efficient and robust solution of Poisson's equation. Finally, in Sec. 7.4, we present the extension of the MSB method to layered heterostructures as a fast and robust way to efficiently calculate dissipative quantum transport properties.

7.1 BASIC IDEA OF THE MSB METHOD

This novel method combines the self-consistent non-equilibrium Green's function method, that was introduced in Chapter 1 and Chapter 4, and the phenomenological Büttiker–Probe scattering model that was discussed in Chapter 5. The self-consistent non-equilibrium Green's function formalism provides clear prescripts to calculate

quantum transport properties whilst the tight interplay between incoherent relaxation processes and quantum interference effects is respected from first principles. However, as discussed in Chapter 4, this formalism requires several coupled integro-differential equations for the Green's functions and self-energies that have to be treated in a self-consistent iterative numerical manner. On the other hand, the phenomenological Büttiker–Probe model that was presented in Chapter 5 is striking for its numerical simplicity. The novel multi-scattering Büttiker–Probe model relies on the basic idea of scattering via virtual floating contacts. It uses virtual floating contacts as external perturbation to mimic the effects of scattering via phonons. However, instead of a phenomenological scattering parameter, the scattering potentials associated with every probe is derived within the non-equilibrium Green's function formalism.

For the derivation of the scattering potentials for the MSB method, we start with the retarded self-energy Σ^R_{AP} for the carrier–acoustic-phonon scattering from Eq. (1.42). It reads

$$\Sigma^R_{\mathrm{AP}}(\mathbf{r}_1,\mathbf{r}_2,E) = \frac{V_D^2 k_B T}{2\rho_M v_s^2 E_{\mathrm{AP}}}\delta(\mathbf{r}_1-\mathbf{r}_2)\int\limits_{E-E_{\mathrm{AP}}}^{E+E_{\mathrm{AP}}} \mathrm{d}E'\, G^R(\mathbf{r}_1,\mathbf{r}_2,E'),$$

where V_D is the scalar deformation potential, ρ_M is the density of the material, v_s is the velocity of sound in the material, and E_{AP} is the energy of acoustic phonons. Note that here we have already employed several approximations such as Fröhlich like coupling mechanism within an equipartition assumption for high temperatures, as discussed in Sec. 1.9.2. Now, we compare this phonon self-energy to the scattering potential of the Büttiker–Probe model, introduced in Eq. (5.7) and Eq. (5.8). It reads

$$B^R(\mathbf{r},E) = \sum_{\kappa\in P} B^{R,\kappa}(E)\,\delta(\mathbf{r}-\mathbf{r}_\kappa),$$

with the single probe scattering strength

$$B^{R,p}(E) = -\,i\eta.$$

If we assume the retarded scattering self-energy of the acoustic phonons (AP) to be represented by the scattering potential of the Büttiker–Probes, $B^R_{\mathrm{AP}}(\mathbf{r},E) \equiv \Sigma^R_{\mathrm{AP}}(\mathbf{r},\mathbf{r},E)$, we can identify the scattering strength of a single probe with the following expression

$$B^R_{\mathrm{AP}}(p,E) = \frac{V_D^2 k_B T}{2\rho_M v_s^2 E_{\mathrm{AP}}}\int\limits_{E-E_{\mathrm{AP}}}^{E+E_{\mathrm{AP}}} \mathrm{d}E'\, G^R(\mathbf{r}_p,\mathbf{r}_p,E').$$

Finally, with the relation of the retarded Green's function to the spectral function and density of states in Eq. (1.28), the scattering strength of a single probe that models carrier–acoustic-phonon scattering reads

$$B^R_{\mathrm{AP}}(p,E) = -i\frac{\pi V_D^2 k_B T}{2\rho_M v_s^2 E_{\mathrm{AP}}} \int\limits_{E-E_{\mathrm{AP}}}^{E+E_{\mathrm{AP}}} \mathrm{d}E'\, \rho(\mathbf{r}_p, E'), \tag{7.1}$$

where ρ is the energy-resolved local density of states.

For the derivation of the scattering potential describing scattering with optical-phonons (OP), we start with the self-energy Σ^R_{OP} derived in Sec. 1.9.2. It reads

$$\begin{aligned}\Sigma^R_{\mathrm{OP}}(\mathbf{r}_1,\mathbf{r}_2,E) = {}& \frac{e^2 E_{\mathrm{OP}}}{2\varepsilon_0}\left(\varepsilon_\infty^{-1} - \varepsilon_s^{-1}\right) \sum_{\mathbf{q}} \left(\frac{\mathbf{q}}{\mathbf{q}^2+\xi^{-2}}\right)^2 e^{i\mathbf{q}(\mathbf{r}_1-\mathbf{r}_2)} \\ & \times \Bigg((1+N_{\mathrm{OP}})\, G^R(\mathbf{r}_1,\mathbf{r}_2,E-E_{\mathrm{OP}}) + N_{\mathrm{OP}}\, G^R(\mathbf{r}_1,\mathbf{r}_2,E+E_{\mathrm{OP}}) \\ & + \frac{1}{2}\Big(G^<(\mathbf{r}_1,\mathbf{r}_2,E-E_{\mathrm{OP}}) - G^<(\mathbf{r}_1,\mathbf{r}_2,E+E_{\mathrm{OP}}) \Big) \Bigg),\end{aligned} \tag{7.2}$$

where e is the charge of the carriers, ξ is the Debye screening length, ε_0 is the electric vacuum permittivity, ε_∞ is the relative electric permittivity at the high frequency limit, ε_s is the relative static low frequency permittivity, and E_{OP} is the energy of the optical phonons. Here, we already made an often used approximation and neglected the small principle part integral [LD92; LW02; Kub10], as discussed in Sec. 1.9.2. However, we cannot employ an equipartition approximation in general, due to the remarkably higher energies of the optical phonons in contrast to the acoustic phonons. Thus, we cannot linearize the Bose distribution. Nevertheless, in the case of the optical phonons the high temperature approximation is not crucial, since we already assume dispersionless optical phonons.

The next step in the derivation of the probe scattering potential B^R_{OP} for the optical phonons is to evaluate the summation over the momentum $\mathbf{q}$. Since we assumed dispersionless optical phonons, we can extract the momentum integral I_{m} that reads as follows

$$I_{\mathrm{m}}(\mathbf{r},\mathbf{r}',\xi) = \sum_{\mathbf{q}} \frac{\mathbf{q}^2 e^{i\mathbf{q}(\mathbf{r}-\mathbf{r}')}}{\left(\mathbf{q}^2+\xi^{-2}\right)^2} \approx \frac{1}{(2\pi)^3}\int \mathrm{d}\mathbf{q} \frac{\mathbf{q}^2 e^{i\mathbf{q}(\mathbf{r}-\mathbf{r}')}}{\left(\mathbf{q}^2+\xi^{-2}\right)^2}. \tag{7.3}$$

A numerical calculation of I_{m} for GaAs and a typical screening length $\xi = 5$ nm is plotted in Fig. 7.1. The narrow peak around $|\mathbf{r}-\mathbf{r}'| \approx 0$ motivates the assumption

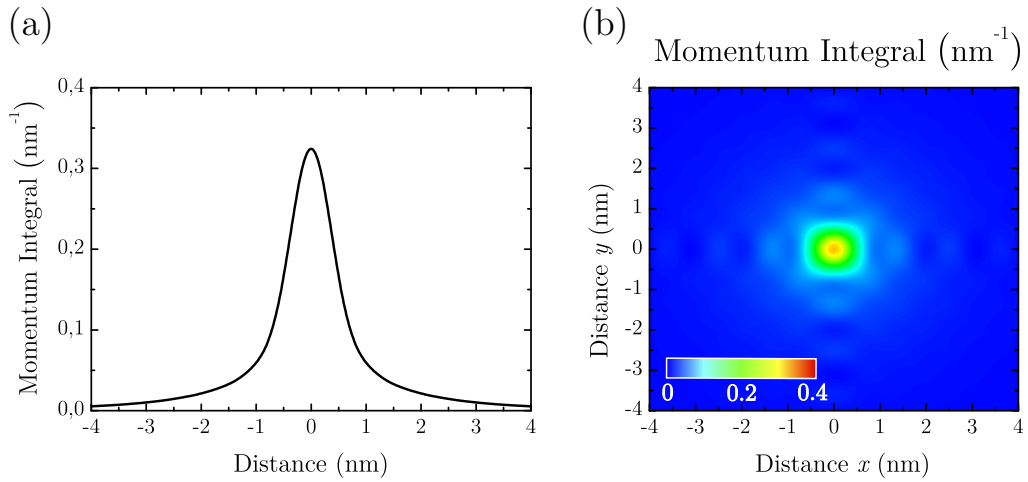

Figure 7.1: (a) Calculated phonon momentum integral I_{m} as a function of the distance s along the path $\mathbf{r}(s) = s(1,1,1)^T$. (b) Calculated phonon momentum integral I_{m} as a function x and y with $\mathbf{r}(x,y) = (x,y,0)^T$. Note that the integral is symmetric for all three spatial directions. This calculation is for GaAs with a typical screening length $\xi = 5$ nm.

that the self-energy Σ^R_{OP} can be approximated as a local scattering potential. Such an assumption of a spatial diagonal self-energy is often used to reduce the tremendous numerical workload [JPM06; YKD07]. Furthermore, we approximate the Brillouin zone of a zincblende face centered cubic (fcc) crystal by a sphere. Hence, we can employ a Taylor series expansion of the momentum integral I_{m} assuming the parameter a/ξ to be small, where a is the lattice constant of the material. Thus, the approximated momentum integral I_{m} reads

$$I_{\mathrm{m}}(\xi) \equiv I_{\mathrm{m}}(\mathbf{r},\mathbf{r},\xi) \approx \frac{1}{6.43a} - \frac{1}{8.57\xi} + \frac{a}{127\xi^2} - \ldots, \tag{7.4}$$

The validity of this approximation is shown in Fig. 7.2. The full integral was calculated for the fcc crystal of GaAs. We find excellent agreement of the approximation from Eq. (7.4) and the exact result.

Now, we compare once more the phonon self-energy Σ^R_{OP} to the scattering potential of the Büttiker–Probe model, introduced in Eq. (5.7) and Eq. (5.8). Here, we identify again the retarded Green's function G^R with the density of states ρ. Additionally, we use the definition of the carrier density in Eq. (1.29) to replace the lesser Green's function with the carrier density n. Thus, the probe scattering potential for the

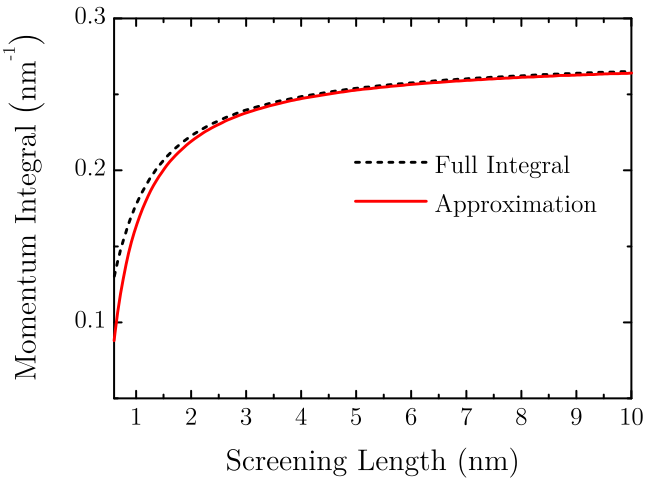

Figure 7.2: Calculated phonon momentum integral I_m from Eq. (7.3) and approximated momentum integral from Eq. (7.4) as a function of the Debye screening length ξ. The calculation was done for GaAs and we find an excellent agreement of the approximation and the full integral for $\xi \gtrapprox 1$ nm.

carrier-optical-phonon scattering reads

$$\begin{aligned} B^{R,p}_{\mathrm{OP}}(E) = -i\frac{\pi e^2 E_{\mathrm{OP}}}{2\varepsilon_0}\left(\varepsilon_\infty^{-1} - \varepsilon_s^{-1}\right) I_\mathrm{m}(\xi) \\ \times \Big((1+N_{\mathrm{OP}})\,\rho(\mathbf{r}_p, E-E_{\mathrm{OP}}) + N_{\mathrm{OP}}\,\rho(\mathbf{r}_p, E+E_{\mathrm{OP}}) \\ + n(\mathbf{r}_p, E-E_{\mathrm{OP}}) - n(\mathbf{r}_p, E+E_{\mathrm{OP}}) \Big). \end{aligned} \tag{7.5}$$

As discussed in Sec. 5.2, the lesser probe self-energies and lesser Green's function can be calculated with the fluctuation–dissipation theorem since the individual probes are assumed to be in equilibrium. Hence, the carrier and current densities can be calculated with the spectral function from Eq. (5.9) associated with every probe after the chemical potentials of the probes are calculated.

However, we have introduced a dependency of the scattering potential of the probes on the Green's function in Eq. (7.1) and Eq. (7.5), since the local density of states as well as the carrier density is directly related to the retarded Green's function. This system of equations requires in principle a self-consistent iterative solution. But in contrast to the fully self-consistent non-equilibrium Green's function approach the MSB method has the following advantages.

First, within the MSB method only two equations for the retarded functions are coupled and have to be solved in an iterative self-consistent manner, whereas the NEGF formalism couples at least four integro-differential equations for the retarded and lesser functions. Thus, the numerical iterative solution of the coupled equations within the MSB method is far more robust and the speed of convergence of the iteration sequence is increased tremendously. We can further enhance the robustness and the speed of convergence if we decouple the retarded and lesser Green's function by neglecting the last line in Eq. (7.5). In contrast to the fully self-consistent NEGF formalism, this decoupling within the MSB method does not violate Pauli's principle, since the probes are assumed to be in a local equilibrium. Secondly, current conservation and Pauli's principle are inherently guaranteed during every step of the iterative solution scheme within the MSB model. This is due to the fact that a chemical potential is explicitly calculated for each probe. Therefore, even in a non-self-consistent Born approximation, current conservation is not violated, in contrast to the NEGF formalism. Note, that the initial value of the local density of states ρ and the density n and thus the initial value of the probe self-energy B^R can be calculated within another formalism, e.g. by a Schrödinger solver.

Thirdly, only the diagonal part of the Green's functions is required during the iteration for a self-consistent solution. The diagonal part of the retarded Green's function G^R gives the local density of states ρ and the diagonal part of the lesser Green's function $G^<$ gives the carrier density n. However, the diagonal part of both Green's functions can be calculated very efficiently, e. g. with the fast-inverse-using-nested-dissection (FIND) algorithm [Li+08; LD12].

In summary, we have presented a novel method to calculate dissipative quantum transport that we termed the multi-scattering Büttiker–Probe (MSB) method. It is based on the so-called Büttiker–Probe scattering model but the treatment of individual scattering mechanisms is retained from the NEGF formalism. The mathematical complexity was reduced to two coupled equations and therefore, quantum transport calculation within the MSB method are far more robust and can be calculated very efficiently. Moreover, current conservation and Pauli's principle are inherently guaranteed.

7.2 NOVEL TYPE OF PROBES FOR TWO-CONTACT DEVICES

In this section, we present a novel type of Büttiker–Probes that side-steps the complex and error prone solution of the nonlinear system of equations for the virtual chemical potential μ_p. As discussed in Sec. 5.2, the convergence behavior strongly depends among other things on the device geometry and the applied bias voltage of the

real contacts. Furthermore, the initial values of the chemical potentials must be well-chosen to achieve convergence at all. Our novel Büttiker–Probe type is especially suited for so-called two-contact devices. A two-contact device is comprised of only two current-carrying contacts that are called "source" and "drain" in the following. Such devices are e. g. a quantum cascade laser (QCL), a resonant tunneling diode (RTD), a *nin*-resistor, or a metal-oxide-semiconductor field-effect transistor (MOSFET), if the small gate-leakage currents are neglected.

The underlying concept of the novel probes is as follows. For two-contact devices, we can assume that the distribution function of each probe is a linear combination of the source and drain distributions, f_S and f_D, respectively. Hence, the distribution function for probe p reads

$$f_p(E) = c_p f_S(E) + (1 - c_p) f_D(E) \qquad \forall\, p \in P, \tag{7.6}$$

where $c_p \in [0, 1]$ are the coefficients for the weighted average of the distribution functions at every probe p. The assumption of a linear combination of the source and drain distribution is reasonable because the carriers inside a two-contact device originate either from the source or drain and also leave through the source or drain. Since both leads are assumed to be in equilibrium, scattering mechanisms inside the device result in a mixture of the equilibrium distributions.

Now, the constraints to the current density in Eq. (5.13) lead to a linear system of equations for the coefficients c_p instead of a nonlinear system of equations for the virtual chemical potentials μ_p. Here, the advantage of this novel probes is twofold. First, the coefficients c_p can be calculated by solving one linear system of equations. This is due to the fact that the coefficients c_p enter Eq. (5.13) linearly and thus, they can be solved directly without any iterative scheme. Secondly, the transmission coefficients T_{ij} between all probes do not have to be stored which reduces the numerical memory consumption tremendously. Since the coefficients c_p can be calculated directly, the energy integration and the calculation of the transmission coefficients T_{ij} in Eq. (5.13) and Eq. (5.11) can be performed together.

7.3 EXTENSION OF THE PREDICTOR–CORRECTOR SCHEME

In this section, we present the adaption of the multi-scattering Büttiker–Probe method to the predictor–corrector scheme for the calculation of the Hartree potential. The predictor–corrector approach is discussed in Sec. 3. It is vital to use a custom tailored predictor density in order to ensure that the iterative solution of Poisson's equation is fast and robust. Within the MSB method, the carrier density is given by

the following expression

$$n(\mathbf{r}) = \int \frac{\mathrm{d}E}{2\pi} \sum_{\alpha,\beta} \phi_\alpha(\mathbf{r}) \Big(\sum_{\lambda \in L} f_\lambda(E) A^\lambda_{\alpha\beta}(E) + \sum_{\kappa \in P} f_\kappa(E) A^\kappa_{\alpha\beta}(E) \Big) \phi^*_\beta(\mathbf{r}),$$

where L is the set of all leads and P is the set of all probes, A are the spectral functions that are associated with every lead and probe, and f are the distribution functions of the leads and probes. Here, we can directly implement the underlying idea of the predictor–corrector approach. We assume that the spectral function does not depend on small changes of the Hartree potential Φ but only the distribution functions f are shifted locally. Thus, the predictor density within the MSB method reads

$$n[\delta\Phi_i](\mathbf{r}) = \int \frac{\mathrm{d}E}{2\pi} \sum_{\alpha,\beta} \phi_\alpha(\mathbf{r}) \Bigg(\sum_{\lambda \in L} f_\lambda\Big(E + \delta\Phi_i(\mathbf{r})\Big) A^\lambda_{\alpha\beta}(E) + \sum_{\kappa \in P} f_\kappa\Big(E + \delta\Phi_i(\mathbf{r})\Big) A^\kappa_{\alpha\beta}(E) \Bigg) \phi^*_\beta(\mathbf{r}),$$

where $\delta\Phi_i$ is the change of the Hartree potential in the i^{th} predictor iteration step. Consequently, the contributions of the carrier density n to the Jacobian matrix from Eq. (3.2) for the Newton–Raphson iteration scheme are diagonal. The Jacobian matrix for the i^{th} iteration step reads

$$J_i(\mathbf{r}, \mathbf{r}') = \frac{\partial F_i(\mathbf{r})}{\partial \Phi_i(\mathbf{r}')} = \delta(\mathbf{r} - \mathbf{r}') \left(\nabla \varepsilon_0 \varepsilon(\mathbf{r}) \nabla + e \frac{\partial n[\Phi_i](\mathbf{r})}{\partial \Phi_i(\mathbf{r})} \right).$$

7.4 EXTENSION TO LAYERED HETEROSTRUCTURES

In this section, we present the extension of the multi-scattering Büttiker–Probe model to layered heterostructures. Although we want to retain the full flexibility of a real-space basis, we can reduce the numerical effort significantly if we employ an appropriate basis, as discussed in Sec. 1.6. We assume the following single-band effective-mass model Hamiltonian

$$H_0(z, k_\parallel) = H_0(z) + H_0(z, k_\parallel),$$

with

$$H_0(z) = -\frac{\hbar^2}{2} \nabla_z \frac{1}{m^*(z)} \nabla_z + V(z) \qquad \text{and} \qquad H_0(z, k_\parallel) = \frac{\hbar^2 k_\parallel^2}{2 m^*(z)},$$

where m^* is the effective mass of the carriers and V is the electrostatic potential. Thus, Dyson's equation for the case of layered heterostructures reads

$$\int \mathrm{d}z_1 \Big(\big(E_z - H_0(z) - e\Phi(z) \big) \delta(z - z_1) - \Sigma^R(z, z_1, k_\parallel, E) \Big) \times G^R(z_1, z', k_\parallel, E) = \delta(z - z'), \tag{7.7}$$

where we made use of the fact that the energy E can be split into a portion E_z along the growth direction of the structure and the portion $E_\parallel$ inside of the lateral layers. Now, within the MSB method we approximate the scattering self-energies in such a way that they depend on the lateral carrier energy E_z only. With these approximated scattering potentials, Dyson's equation for the case of layered heterostructures from Eq. (7.7) is independent of $k_\parallel$. Therefore, to finally calculate the observables, we can do the necessary $k_\parallel$ integration analytically which leads to a tremendous simplification of the numerical calculations [Ven+03]. A detailed derivation of this $k_\parallel$ integration is given in Appendix B.

In order to derive the scattering potentials for layered heterostructures, we apply again the basic ideas of the MSB method and replace the retarded Green's function G^R with the local density of states ρ, and the lesser Green's function $G^<$ with the carrier density n. However, for layered heterostructures, we assume that the density of states ρ and the carrier density n is constant inside the two-dimensional layers and thus, the Fourier transformation of both quantities yields a δ-distribution in $k_\parallel$. Thus, we assume the following replacement of the Green's functions including the Fourier transformation

$$\begin{aligned} -G^R(\mathbf{r}, \mathbf{r}', E) &\to \pi\rho(z, k_\parallel, E_z + E_\parallel) \overset{k_\parallel = 0}{\longrightarrow} \pi\rho(z, E_z), \\ -G^<(\mathbf{r}, \mathbf{r}', E) &\to 2\pi n(z, k_\parallel, E_z + E_\parallel) \overset{k_\parallel = 0}{\longrightarrow} 2\pi n(z, E_z). \end{aligned} \tag{7.8}$$

We start with the derivation of the scattering potential for the acoustic phonons. The Fourier transformed scattering self-energy from Eq. (1.42) for carrier–acoustic-phonon scattering in the basis for layered heterostructures reads

$$\Sigma^R_{\mathrm{AP}}(z_1, z_2, k_\parallel, E) = \frac{V_D^2 k_B T}{8\pi^2 \rho_M v_s^2 E_{\mathrm{AP}}} \delta(z_1 - z_2) \int_{E - E_{\mathrm{AP}}}^{E + E_{\mathrm{AP}}} \mathrm{d}E' \int \mathrm{d}\mathbf{k}'_\parallel \, G^R(z_1, z_2, k'_\parallel, E').$$

Here, we can directly use Eq. (7.8) and obtain the following scattering potential for carrier–acoustic-phonon scattering within the MSB method

$$B^{R,p}_{\mathrm{AP}}(E_z) = -i \frac{V_D^2 k_B T}{8\pi \rho_M v_s^2 E_{\mathrm{AP}}} \int_{E_z - E_{\mathrm{AP}}}^{E_z + E_{\mathrm{AP}}} \mathrm{d}E' \, \rho(\mathbf{r}_p, E').$$

Next, the Fourier transformed scattering self-energy from Sec. 1.9.2 for carrier–optical-phonon scattering in the basis for layered heterostructures reads

$$\begin{aligned}\Sigma^R_{\mathrm{OP}}(z_1, z_2, \mathbf{k}_\parallel, E) = \\ &\frac{e^2 E_{\mathrm{OP}}}{2\varepsilon_0}\left(\varepsilon_\infty^{-1} - \varepsilon_s^{-1}\right)\frac{1}{4\pi^2}\int \mathrm{d}\mathbf{k}'_\parallel\, I_m(z_1 - z_2, \mathbf{k}_\parallel + \mathbf{k}'_\parallel, \xi) \\ &\times\Bigg(N_{\mathrm{OP}}\, G^R(z_1, z_1, k'_\parallel, E - E_{\mathrm{OP}}) + (1 + N_{\mathrm{OP}})\, G^R(z_1, z_1, k'_\parallel, E + E_{\mathrm{OP}}) \\ &\quad + \frac{1}{2}\Big(G^<(z_1, z_1, k'_\parallel, E - E_{\mathrm{OP}}) - G^<(z_1, z_1, k'_\parallel, E + E_{\mathrm{OP}})\Big)\Bigg),\end{aligned}$$

where we already substituted the phonon momentum $\mathbf{q}_\parallel$ into the final carrier momentum $\mathbf{k}'_\parallel$. The momentum integral I_m is the only term that depends on the phonon momentum q_z and it is given by

$$I_m(z, k_\parallel, \xi) = \frac{1}{2\pi}\int \mathrm{d}q_z \frac{e^{iq_z z}(k_\parallel^2 + q_z^2)}{\left(k_\parallel^2 + q_z^2 + \xi^{-2}\right)^2}.$$

Here, we use the approach of Stephen M. Goodnick and Paolo Lugli in Ref. [GL88] and assume the phonon momentum to be much larger than the carrier momentum [Kub10]. Thus, we can extend the integral over the total real axis. With this approximation, the momentum integral I_m simplifies to the following form

$$I_m(z, k_\parallel, \xi) = \frac{\exp\left(\sqrt{\xi^{-2} + k_\parallel^2}\,|z|\right)}{2\sqrt{1 + k_\parallel^2\xi^{-2}}}\left(\xi - \frac{|z|}{2\sqrt{1 + k_\parallel^2\xi^{-2}}} - \frac{\xi}{2(1 + k_\parallel^2\xi^{-2})}\right).$$

The momentum integral I_m is plotted in Fig. 7.3 as a function of the carrier momentum $k_\parallel$ and the distance $z = |z_1 - z_2|$. It reaches its maximum value in the region where both the distance z and the carrier momentum $k_\parallel$ are small. This justifies the assumption of a δ-distribution in the spatial coordinate z. On the other hand, the typical range of the carrier momentum in layered semiconductor nanostructures is far below 1 nm^{-1}, e. g. the momentum of electrons with the kinetic energy of 150 meV in GaAs is approximately 0.33 nm^{-1}. Within this range, it is justified to approximate the momentum integral I_m as roughly constant, as depicted in Fig. 7.3. Thus, we can approximate the scattering self-energy to be independent of $k_\parallel$. Indeed, it is often found in literature, that momentum-independent scattering matrix elements and diagonal self-energies are utilized to significantly reduce the numerical effort to calculate quantum transport properties [Wac+99; Wac02a; LW02].

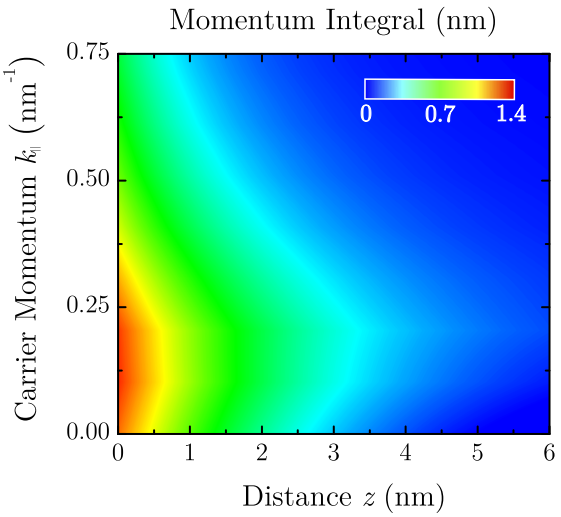

Figure 7.3: Calculated phonon momentum integral I_m as a function of the distance $z = |z_1 - z_2|$ and the carrier momentum $k_\parallel$. Note that the integral is symmetric in z. This calculation is for GaAs with a typical screening length $\xi = 5$ nm.

Hence, by inserting the replacements given by Eq. (7.8) into the self-energy Σ^R_OP, we finally obtain the scattering potential for the carrier–optical-phonon scattering within the MSB method as

$$\begin{aligned} B^{R,p}_\mathrm{OP}(E_z) = -i\frac{e^2\xi E_\mathrm{OP}}{32\pi\varepsilon_0}\left(\varepsilon_\infty^{-1} - \varepsilon_s^{-1}\right) \\ \times\Bigg((1+N_\mathrm{OP})\,\rho(\mathbf{r}_p, E_z - E_\mathrm{OP}) + N_\mathrm{OP}\,\rho(\mathbf{r}_p, E_z + E_\mathrm{OP}) \\ + n(\mathbf{r}_p, E_z - E_\mathrm{OP}) - n(\mathbf{r}_p, E_z + E_\mathrm{OP})\Bigg). \end{aligned} \tag{7.9}$$

As discussed in Sec. 7.1, we can neglect the contributions of the carrier density in Eq. (7.9), i. e. the last line of Eq. (7.9), to enhance the convergence while Pauli's principle is still inherently guaranteed. In the following sections, the approximation where the contributions of the carrier density to the scattering self-energies are neglected is called the density approximation.

Part III

RESULTS AND ASSESSMENT OF THE NOVEL MSB METHOD

8 ASSESSMENT OF THE MSB METHOD

We show that the approximations within the MSB method cause no artifacts. This is an important requirement for any transport calculation. The MSB method reduces the complexity of the coupled equations that are involved in a fully self-consistent NEGF formalism. Thus, the transport equations within the MSB method are numerically more robust and their solution is very stable and less error prone. However, the MSB method is based on the Büttiker–Probe formalism and combines its numerical lightweight with the scattering self-energies from the self-consistent NEGF formalism. To preserve the numerical efficiency of the Büttiker–Probe model, many approximations to the scattering self-energies within the MSB method have to be employed. Although, these approximations are well justified, it is not straightforward to see if they still capture the essential physical effects. Thus, we consider carrier transport in simple and well understood devices to assess the validity of the MSB method. The results of complex quantum cascade laser devices are presented in the next chapter.

In this chapter, we consider a simple *nin* resistor to prove that the MSB method includes the semi-classical limit where quantum effects do not play an important role. Then, we investigate the transport characteristics of a resonant tunneling diode (RTD) to demonstrate that the MSB method also captures inelastic scattering effects. We show that the novel type of Büttiker–Probes for two-contact devices yields the same observable quantities as the standard iterative approach. Finally, we also calculate the current–voltage characteristics of an RTD within the three-dimensional real space MSB method. The results agree with the calculations for layered structures.

8.1 THE SEMI-CLASSICAL LIMIT

In this section, we consider a simple symmetric GaAs *nin* resistor at 300 K. The device has an extent of 50 nm and a central intrinsic region of 12 nm. The n-doped regions are doped with 1×10^{18} cm^{-3}. Such a structure does not have any barriers or wells

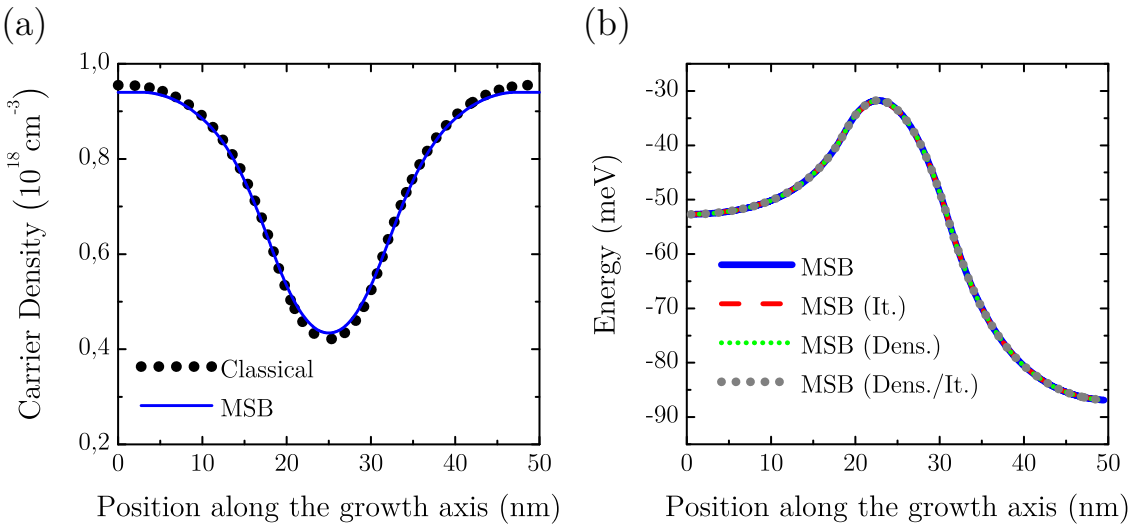

Figure 8.1: (a) Comparison of the calculated carrier density for an MSB calculation (solid blue line) and a semi-classical calculation (dotted black line) for a 50 nm GaAs *nin* resistor at zero bias voltage and 300 K. (b) Calculated conduction band edge profiles for the GaAs resistor for an applied bias voltage of 50 mV. All profiles are calculated with the MSB method but with different approximations and probe types as described in the text. Note that all four profiles almost perfectly match.

and thus, no bound states are present. Hence, we can expect that such a device can be described by the semi-classical Boltzmann equation including phonon scattering and carrier–carrier scattering at least within the Hartree approximation. This semi-classical result is shown in Fig. 8.1 (a) along with a charge self-consistent MSB calculation. The MSB calculation (blue line) matches the semi-classical calculation (black dotted line) very well. For the MSB calculation the novel two-contact probes were used and the contributions of the carrier density were neglected (density approximation). The influence of the novel two-contact probes and the density approximation within the semi-classical limit is investigated in Fig. 8.1 (b). Here, the conduction band edge profiles for the GaAs resistor with an applied bias voltage of 50 mV are plotted for various MSB calculations. The solid blue line corresponds to an MSB calculation with the novel two-contact probe type and the density approximation. The red dashed line was calculated with the standard iterative probe type and the density approximation. The dotted green line corresponds to a calculation with the novel probe type but takes into account the dependency of

the scattering self-energies on the carrier density. Finally, the gray dotted line was calculated with the standard iterative probe type and considering the dependency of the self-energies on the carrier densities. These four conduction band edge profiles that are calculated in charge self-consistent manner match perfectly. This implies that the neglect of the contributions of the carrier density to the self-energy is well justified within the semi-classical limit. The density approximation reduces the numerical load tremendously. This is due to the fact that the carrier density is directly related to the solution of the Büttiker–Probes to ensure current conservation, whilst at the same time the charge density influences the self-energies that determine the Green's function and thus changes the conditions for current conservation. Thus, the numerical stability of the solution of the quantum transport equations can be improved immensely by removing these dependencies. Furthermore, the novel probe type that can be calculated without the iterative solution of a nonlinear system of equations also enhances the numerical efficiency. The calculated results within the semi-classical limit, however, do not depend on those approximations. Thus it is well justified to use the novel probe type as well as the density approximation.

8.2 INELASTIC SCATTERING

In this section, we consider a simple resonant tunneling diode (RTD) to assess the results of the MSB method for quantum devices. We calculate a 48 nm GaAs device where the central region consists of an RTD with two 4 nm AlGaAs barriers that enclose a 4 nm intrinsic region. The regions outside the RTD are doped with 1×10^{17} cm^{-3}. The calculated DC current as a function of the applied bias voltage is shown in Fig. 8.2. The solid gray line shows the result of a purely ballistic calculation. The peak current density is reached at about 90 mV where the chemical potential of the source contact is aligned with the lowest quantum well state. However, this result is physically wrong [Kub10]. This is due to the fact that a ballistic calculation neglects any kind of incoherent scattering. In a realistic device the carriers do not ballistically reach the RTD. Instead, a bound state is formed by the triangular shaped potential in front of the RTD and inelastic scattering processes lead to a capture of carriers within this state. Since the energy of this bound state is lower than the chemical potential of the source contact the alignment with the RTD resonance is realized at higher bias voltages. For the calculated RTD the peak current density is shifted from 90 mV to 130 mV.

The influence of the novel two-contact probes and the density approximation for quantum devices is also investigated in Fig. 8.2. The solid blue line is calculated with the novel two-contact probe type and neglects the dependency of the scattering

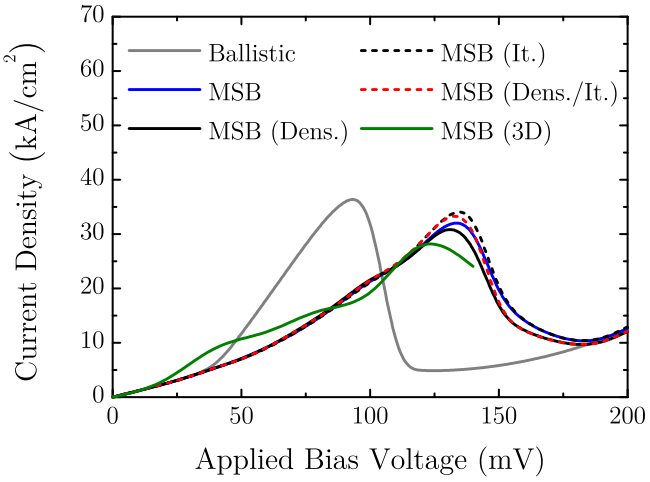

Figure 8.2: Calculated DC current as a function of the applied bias voltage for the resonant tunneling diode described in the text. The gray line corresponds to a ballistic calculation whereas the color lines are calculated with the MSB method. The solid green line results from a 3D calculation and agrees with the other current–voltage calculations that are based on the special quasi-1D basis for layered heterostructures. Note that the 3D calculation consumed huge computational resources and thus bias voltages above 150 mV could not be resolved appropriately. The slight discrepancies compared to the quasi-1D calculations originate from the low numerical resolution. This is explained in the text in detail.

self-energies and the carrier density. The solid black was also calculated with the novel probe type but takes into account the dependency of the scattering self-energies on the carrier density. The dashed black line was calculated with the standard iterative probe type and within the density approximation. The dashed red line also corresponds to a calculation with standard iterative probe type but takes into account the dependency of the scattering self-energies on the carrier density. All aforementioned calculations use the special quasi-one-dimensional basis for layered heterostructures that was introduced in Sec. 1.6. These four current–voltage characteristics that are calculated with a quasi-one-dimensional basis match each other very well. Thus, the novel Büttiker–Probe type as well as the density approximation is well justified in the dissipative quantum regime.

The solid green line was calculated using a fully three-dimensional real space basis. Note that although the MSB method is numerically very efficient, a calculation with a fully three-dimensional real space basis still imposes an extremely high numerical burden. For the actual calculation 75 gigabytes of computational memory were

needed and the calculation of the current–voltage characteristics took more than 900 hours of CPU time. The three-dimensional RTD was modeled as a bar with a cross section of $80 \times 80\ \mathrm{nm}^2$. This size leads to hardly any confinement effects but keeps the numerical effort manageable on our compute servers, although the numerical discretization is already quite coarse. The current–voltage characteristics was calculated only up to an applied bias voltage of 150 mV since the enormous numerical effort limited the numerical discretization of the energy domain. Higher bias voltages imply a larger range within the energy domain and thus, more grid points for the numerical discretization. Due to that reason, bias voltages above 150 mV could not be resolved sufficiently on our computer hardware. However, despite the numerical limitations and the possibility of small confinement artifacts, the results from the fully three-dimensional calculation are in consistency with the other MSB calculations. Thus, the approximations introduced in Chapter 7.4 that are needed to efficiently use the MSB method for layered heterostructures, are in agreement with the results of fully three-dimensional calculations.

In this section, we used the MSB method to calculate an RTD where quantum effects are essential. We showed that the novel and numerical efficient Büttiker–Probe type as well as the decoupling of the scattering self-energies and the carrier density are well justified for quantum devices. Furthermore, the limit of a fully three-dimensional device corresponds to quasi-one-dimensional calculations for layered heterostructures. In the next chapter, we apply the MSB method to realistic quantum devices and compare the calculated results with experimental data.

9 RESULTS FOR QUANTUM CASCADE LASERS

Layered heterostructures were proposed already in the early 1970s by Esaki and Tsu for optoelectronic devices [ET70]. The idea to use inter-subband transitions to build a laser device was published by Rudolf F. Kazarinov and Robert A. Suris in 1971 [KS71]. Since the first experimental demonstration of a quantum cascade laser (QCL) by Faist et al. [Fai+94] in 1994, these devices have been an important source of electromagnetic radiation for specific wavelengths in domains like the infrared (IR) mid-infrared (MIR) and terahertz (THz) spectral ranges [Gma+01].

In contrast to a diode laser, QC lasers are designed to enable transitions from an upper energy state to a lower energy state within one band, typically the conduction band. Thus, electrons do not recombine with holes and the emitted photons have exactly the energy difference of the two aforementioned states. This enables the engineering of the exact energy of the emitted photons. This photon energy is determined by the alignment of the states within the QCL and it can be tailored over a wide range through the variation of the well and barrier thicknesses, barrier heights, doping concentrations, as well as the employed materials.

During the last decade, the performance of QC lasers has been improved remarkably and the emission wavelength ranges from the mid-infrared (MIR) to the far-infrared (FIR) or THz domain. Nowadays, QC lasers have a growing range of applications such as optical transmissions for telecommunications, spectroscopic applications and remote sensing of environmental gases, and the process control in plasma chemistry [Lan+10]. Among the future applications there may be may vehicular cruise control during poor sight conditions, collision detection and avoidance radars, and medical applications such as breath analyzers.

This wide range of applications is only possible due to the customizability of the QC laser emission wavelength. However, to optimize and design QC laser devices an efficient yet accurate calculation of dissipative transport properties is essential. In principle, the fully self-consistent non-equilibrium Green's function framework is very well suited for such a purpose. However, it cannot be used within a rapid design

process due to the implicated numerical workload as discussed in Chapter 4 and Chapter 6. In contrast, the novel MSB method is numerically orders of magnitudes faster than the fully self-consistent NEGF approach, yet reproduces the results of the latter method, and matches experimental data. In particular, the MSB method can handle device geometries that are numerically too demanding for a fully self-consistent NEGF approach.

9.1 FUNDAMENTALS OF QCL DEVICES

A quantum cascade laser is a so-called unipolar device that uses only one carrier species to generate light output. It consists of layers of primarily two different material compositions, one with a larger bandgap and one with a smaller bandgap. Along the growth direction, the smaller bandgap material forms quantum wells, whereas the larger bandgap material imposes barriers for the electrons within the conduction band. The carriers are confined in discrete energy levels within these wells. Due to coupling effects, the energy levels in consecutive quantum wells form so-called minibands. Perpendicular to the growth direction the carriers are not confined which results in a two-dimensional subband dispersion.

A certain layer sequence forms a so-called stage or period. These stages are repeated or cascaded up to several hundred times to maximize the generation of light. In each stage, the alignment of the energy states leads to the formation of an injector region, active region, and a collector region. In an optimized QCL design, the collector region of one stage automatically acts as injector region of the next stage. The purpose of the injector–collector region is to prevent the carriers from tunneling from one injector region to the next injector region without any laser transition within the active region. This is achieved e. g. by the formation of minibands and thus, providing a certain density of states that suppresses a direct tunneling through the active region. This boosts the laser transitions within the active region and enhances the light generation. Note that there are also so-called short-injector or even injector-less QCL designs where the injection and collection mechanisms are incorporated within the active region.

The alignment of the energy states is sensitive to the applied bias voltage. Thus, lasing is typically observed above the so-called threshold-voltage and vanishes again for higher voltages. The threshold-voltage is a characteristic quantity for every QCL design.

The operation principle of a QCL is illustrated in Fig. 9.1. Part (a) shows the calculated conduction band profile and a contour plot of the energy and spatially resolved spectral function $A(z, E_z)$ at vanishing in-plane momentum $k_{\|} = 0$ for

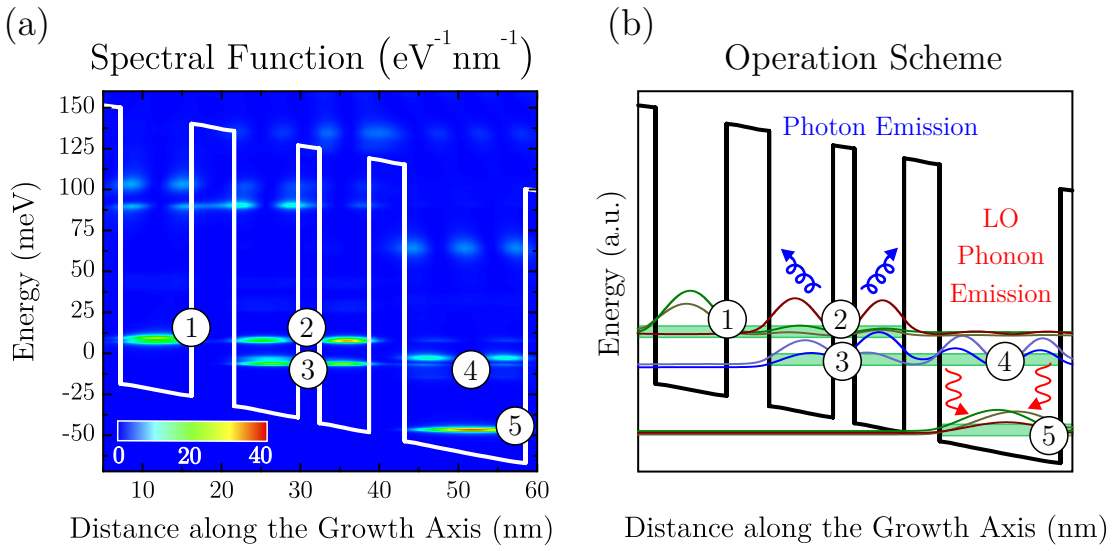

Figure 9.1: (a) Calculated conduction band profile (line) and contour plot of the energy and position resolved spectral function at vanishing in-plane momentum for the THz QCL described in Ref. [Ben+07] at the threshold bias voltage of 50 mV per period and a lattice temperature of 40 K. (b) Schematic QCL operating principle. The blue arrows mark the photon emission and the red arrows show the LO-phonon emissions that depopulate the lower laser level. The squared wave functions of the important states are superimposed.

the QCL described in Ref. [Ben+07]. The QCL is based on 271 identical stages consisting of GaAs wells and $Al_{0.15}Ga_{0.85}As$ barriers.The layer sequence for each period is **3**/9.2/**5.5**/8/**2.7**/6.6/**4.1**/15.5 nm, starting at the leftmost barrier. The $Al_{0.15}Ga_{0.85}As$ barriers are shown in bold and the GaAs wells in normal font. The applied bias voltage is 50 mV per period which is slightly above the threshold voltage. The energy states that contribute to the functional principle are labeled with numbers. Part (b) of Fig. 9.1 shows the operation scheme of this QCL with the squared wave functions of the labeled states. State "1" is the so-called injector state that is shown as green squared wave function in Fig. 9.1(b). It is coherently fed by state "5" from the previous period, depicted with an olive-green squared wave function. The overlap of these wave functions is quite obvious. The injector state is aligned with the upper laser state "2", shown as brown squared wave function. Thus, state "2" can be filled through resonant tunneling. The lower laser state "3" is emptied by two mechanisms. An efficient depopulation of the lower laser states is crucial to build up a population inversion and thus, for the photon generation. The first depopulation mechanism

is the emission of a longitudinal optical (LO) phonon. This is efficiently possible since the energy difference of state “3” and the collector state “5” is approximately the energy of an LO phonon which is 34 meV in GaAs. The second depopulation mechanism of state “3” is a coherent tunneling into state “4” which is aligned with the lower laser state. The collector state “5” coherently feeds the injector state “1” of the next period, as mentioned at the beginning. Thus, any carrier can in principle generate a photon in every period. This shows the fundamental scalability of QC lasers.

However, this previously described mechanism of photon generation is an idealized situation. In reality there are various other scattering paths and so-called carrier escape routes that do not lead to any photon generation. It is a main objective for a successful QCL design to minimize these non-radiative transitions of carriers through the individual periods.

Hence, the understanding of the fundamental carrier relaxation processes is inevitable for the design and successful optimization of QC lasers. Here, the novel MSB method provides an efficient and robust way to e. g. sweep several parameters, barrier thicknesses, or doping concentrations to quickly find an optimized design.

9.2 RESULTS FOR THZ QUANTUM CASCADE LASERS

Radiation around the 1 to 10 terahertz (THz) spectral range, corresponding to an energy of 4 to 40 meV and a wavelength of 300 to 30 µm, has recently attracted attention for imaging techniques due to its unique spectral properties [Beh+08]. Terahertz waves are just short enough to enable resolutions within the micrometer domain, yet long enough so that most non-metallic materials appear translucent. This makes them ideal candidates for the analysis of human body tissue, especially for the detection of cancerous growth. Furthermore, complex molecules and solids often have their spectral signature within the THz domain. This promotes THz QC lasers for atmospheric and environmental monitoring, spectroscopy, and sensing for explosives or drugs [Kum+11]. Among the common features of all QC laser based optical methods are a high frequency selectivity which enables high detection accuracies and the possibility for real-time applications.

In this section we present the results of our novel MSB method for THz QCL devices. We compare the results with a fully self-consistent NEGF implementation and with experimental data. First, we show the results on the QCL presented in Ref. [Ben+07]. Then, we compare our MSB method with a fully self-consistent NEGF calculation based on the device published in Ref. [KMK10] and to the experimental data published in Ref. [Juk+09].

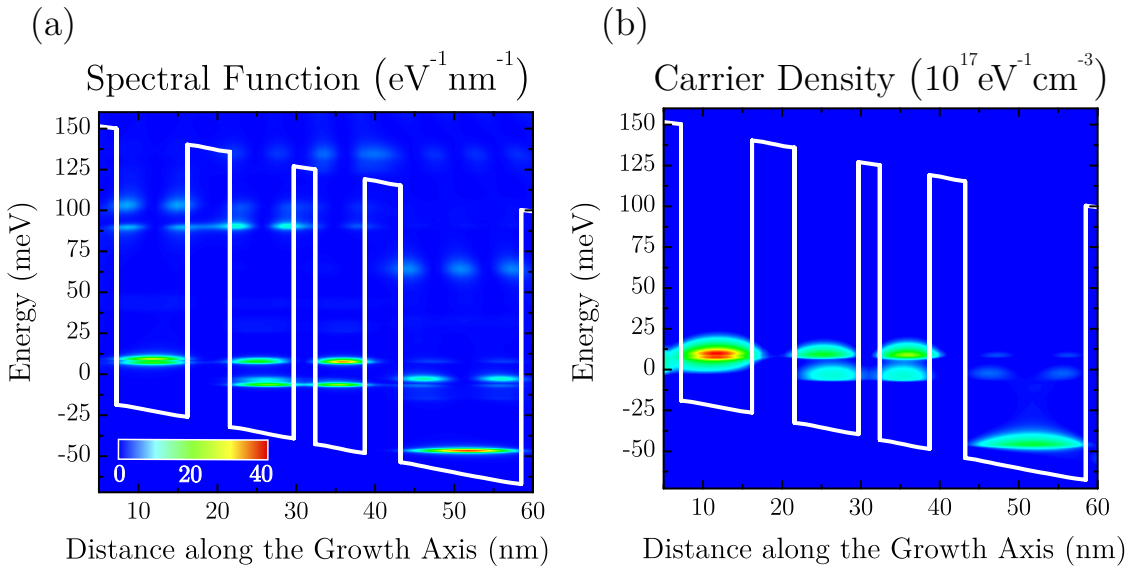

Figure 9.2: (a) Calculated conduction band profile (line) and contour plot of the energy and position resolved spectral function at vanishing in-plane momentum for the THz QCL described in Ref. [Ben+07] at a bias voltage of 50 mV per period, a lattice temperature of 40 K, and a doping density of 1.25×10^{16} cm^{-3}. (b) Calculated contour plot of the corresponding energy and position resolved carrier density. Here, the occupation inversion within the active region can be clearly seen.

9.2.1 *Comparison of MSB with NEGF and experiment*

In this section, we first investigate a THz quantum cascade laser emitting around 2.8 THz ($E_\gamma = 11.4$ meV) presented in Ref. [Ben+07]. The individual lasers are based on the identical structure regrown with varying doping densities. The structure layout is based on the longitudinal optical (LO) phonon depopulation of the lower laser level. The operation scheme and the layer sequence of this QCL is described in the previous section and depicted in Fig. 9.1. The calculated conduction band profile and the position resolved spectral function is shown in Fig. 9.2 (a) for a bias voltage of 50 mV per period which is slightly above the threshold voltage. The corresponding calculated energy and position resolved carrier density is depicted in Fig. 9.2 (b). Here, the occupation inversion of the upper and lower laser states that were labeled "3" and "4" in Fig. 9.1 can be seen clearly. This occupation inversion is a requirement to yield optical gain and thus, to enable laser activity.

The analysis of the position resolved optical gain introduced by Tillmann Kubis in Ref. [Kub10] is very useful to investigate where photon absorption and more

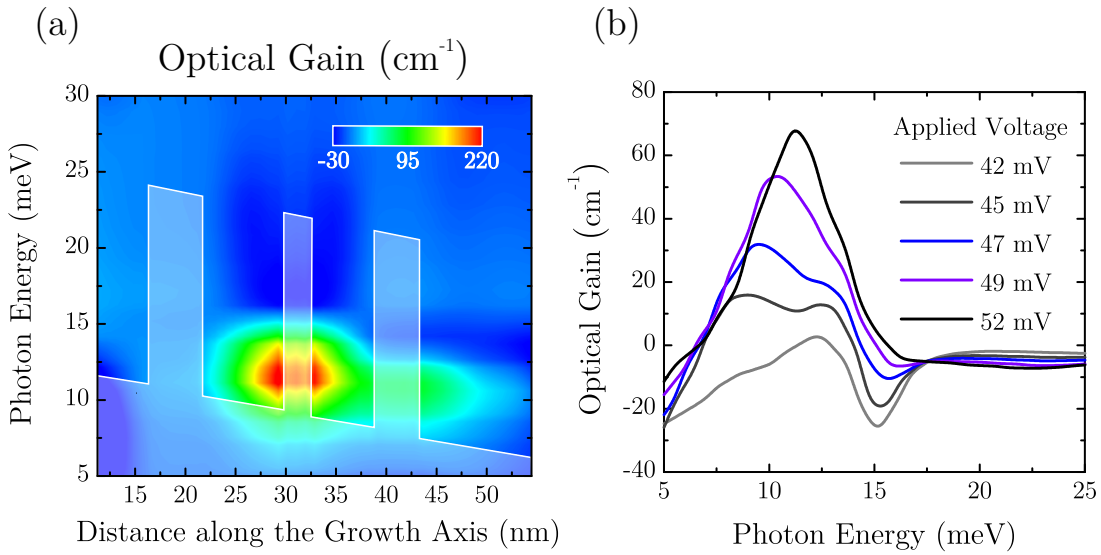

Figure 9.3: (a) Calculated optical gain as a function of the photon energy and the distance along the growth axis for the GaAs/AlGaAs THz QCL described in Ref. [Ben+07]. The conduction band profile is superimposed and only meant to guide the eye. The applied bias voltage is 50 mV, the temperature is 40 K, and the doping density is 1.25×10^{16} cm^{-3}. The peak optical gain originates from the two quantum wells from $z = 25$ nm to $z = 35$ nm. (b) Calculated optical gain as a function of the photon energy. The optical gain was calculated for various bias voltages near the threshold voltage. The optical losses are estimated to be 13 cm^{-1} and thus, the threshold voltage can be estimated to lie between 45 mV and 47 mV whereas experimental data for the threshold voltage is 45 mV.

interestingly photon emission takes place inside a QCL. Since the photon wave function spreads over several QCL stages only the spatially averaged optical gain can be observed experimentally. However, it is often instructive to also investigate the position resolved optical gain [Kub10]. The position resolved optical gain corresponding to Fig. 9.2 is shown in Fig. 9.3 (a). Here, it can be seen that the optical gain originates from the active region ranging from $z = 25$ nm to $z = 35$ nm. Note that the superimposed conduction band profile is only meant to guide the eye and thus, it is not in scale with the photon energy. In Fig. 9.3 (a), we also see that the energy of the emitted photons is $E_\gamma \approx 12$ meV. This corresponds to a frequency of 2.9 THz. This value agrees very nicely with the experimental data of 2.7 THz and the value of 2.8 THz calculated within the fully self-consistent NEGF framework [Kub10].

	Exp.	NEGF	MSB
Threshold voltage (mV)	43	48	45
Emission frequency (THz)	2.8	2.7	2.9

Table 9.1: Comparison of the calculated threshold voltage and the emission frequency with experimental data for the THz QCL described in Ref. [Ben+07].

The threshold voltage, i. e. the applied bias voltage for which the optical gain compensates for all optical losses and thus, the QCL starts to emit photons, can be estimated with Fig. 9.3 (b). There, the optical gain as a function of the photon energy is plotted for various bias voltages. Note, that the calculations do not include interactions with the photon field. Thus, the calculated optical gain does not include any losses due to photon interactions nor any other losses like waveguide losses. For a doping density of 1.25×10^{16} cm^{-3} the expected waveguide losses are 13 cm^{-1} [Ben+07]. Thus, for an applied bias voltage of 45 mV per period the calculated optical gain in Fig. 9.3 (b) exceeds the aforementioned losses. A further increase of the applied bias voltage beyond the threshold voltage leads to a further increase of the calculated optical gain.

These results are summarized in Table 9.1 for a concise overview. The results calculated with our novel MSB method accurately match the results from a fully self-consistent non-equilibrium Green's function calculation as well as the experimental data.

Finally, the current–voltage characteristics, especially the threshold current that corresponds to the threshold voltage is of great interest. In Fig. 9.4 the calculated DC current density is plotted as a function of the applied bias voltage per period. The solid blue line was calculated with our novel MSB method, the solid gray line was calculated with a fully self-consistent NEGF model within a self-consistent Born approximation (SCBA), and the dotted line shows the experimental data. The calculated current density within our novel MSB method matches with the results of the fully self-consistent NEGF model and both agree very well with experimental data. However, the computational costs differ dramatically. The fully self-consistent NEGF model consumed up to 30 gigabytes of memory and the computation time for the current–voltage characteristics depicted in Fig. 9.4 was more than 5 days. Note that a typical workstation nowadays provides 4 to 8 gigabytes of memory and thus a special compute server had to be used. On the other hand, the MSB method required less than 1 gigabyte of memory and the computation time to calculate the current–voltage characteristics was less than 1 hour on the same machine.

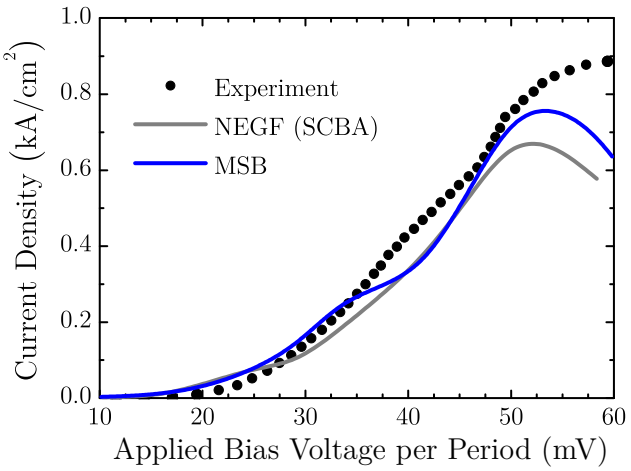

Figure 9.4: Calculated DC current as a function of the applied bias voltage for the GaAs/AlGaAs THz QCL described in Ref. [Ben+07] for a lattice temperature of 40 K and a doping density of 1.25×10^{16} cm^{-3}. The solid blue line was calculated with our novel MSB method, the solid gray line was calculated with an NEGF model within the self-consistent Born approximation (SCBA), and the dotted line shows the experimental data.

The negative differential resistance above the threshold voltage for an applied bias voltage per period of about 50 mV is due to the misalignment of the injector and collector states. The experimental data also shows the effects of misaligned states, however, at higher voltages and not as pronounced as the calculated results. This can be explained by the fact that the calculations neglect any couplings to the photon field. Due to this approximation, the current density above the threshold voltage is underestimated [Kub10].

In Table 9.2, we have put together the calculated and experimentally observed threshold currents for the various doping densities of Ref. [Ben+07]. Identically to the aforementioned observables the threshold current calculated within the MSB method closely resembles the results obtained from a NEGF model and both reasonably agree with the experimental data.

Next, we investigate the THz quantum cascade laser emitting at 3.1 THz ($E_\gamma =$ 12.8 meV) presented in Ref. [Juk+09]. The design of this laser is very similar to the previously discussed QCL. However, instead of coherently filling the upper laser state this design uses a longitudinal optical (LO) phonon transition from the collector state of one period to the injector state of the next period. This QCL consists of 226 identical stages. Each stage is made up of GaAs/$Al_{0.15}Ga_{0.85}$As layers and the

Doping	Threshold current (A/cm^2)		
($10^{15}/cm^3$)	Exp.	NEGF	MSB
12.5	510	503	505
8.0	305	368	331
5.3	216	220	217
3.5	142	132	143

Table 9.2: Comparison of the calculated threshold current with experimental data for the THz QCL described in Ref. [Ben+07].

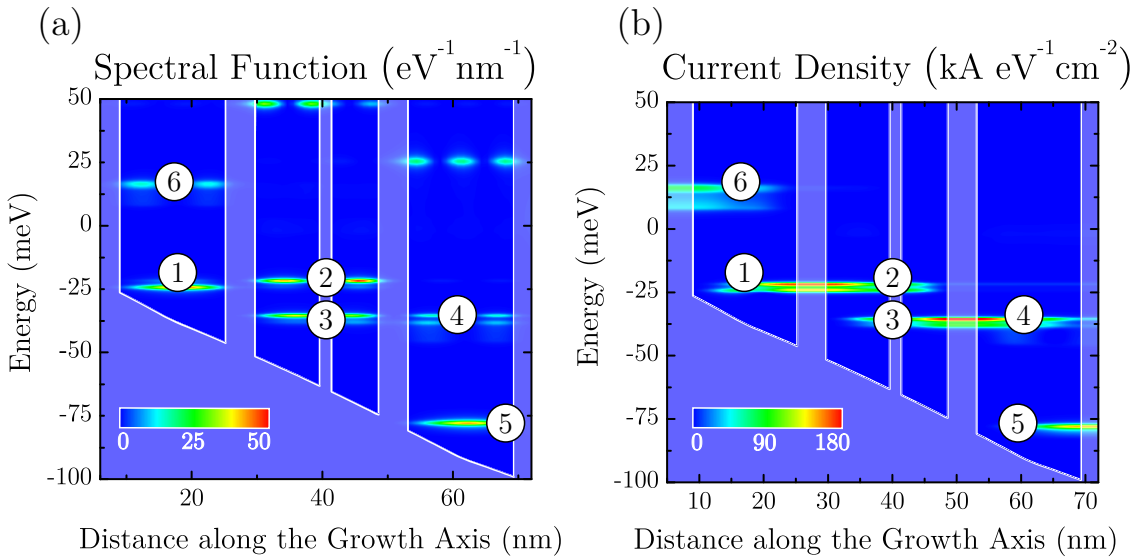

Figure 9.5: (a) Calculated conduction band profile (line) and contour plot of the energy and position resolved spectral function at vanishing in-plane momentum for the THz QCL described in Ref. [Juk+09] at the threshold bias voltage of 44 mV per period and a lattice temperature of 40 K. (b) Corresponding contour plot of the energy and position resolved current density. The shaded area indicates the conduction band profile.

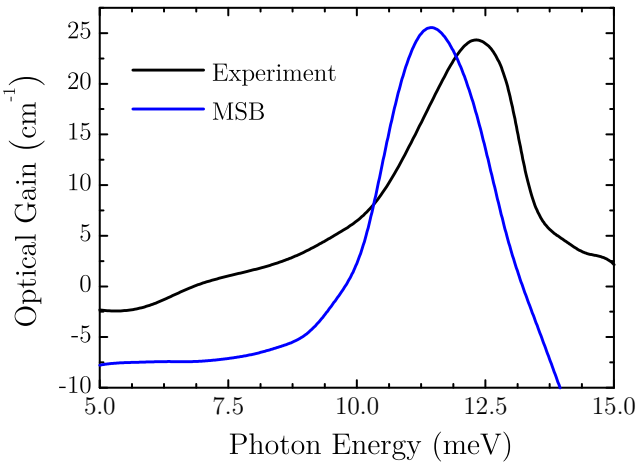

Figure 9.6: Optical gain as a function of the photon energy for the QCL structure described in Ref. [Juk+09]. The solid blue line is calculated with the MSB method whereas the solid black line shows the experimental data.

layer sequence is **4.8**/9.6/**2**/7.4/**4.2**/16.1 nm, starting with the leftmost barrier. The $Al_{0.15}Ga_{0.85}As$ barriers are shown in bold and the GaAs wells in normal font. Only the widest well is doped. The calculated conduction band profile and the contour plot of the energy and position resolved spectral function at vanishing in-plane momentum is shown in Fig. 9.5 (a) The corresponding contour plot of the energy and position resolved current density is shown in Fig. 9.5 (b). This QCL works as follows. Carriers are coherently filled from the collector state labeled “5” in Fig. 9.5 into the injector state “6” of the next period. Then the injector state “1” which is coherently aligned with the upper laser state “2” is populated via resonant phonon emission. The lower laser state “3” is efficiently emptied through coherent tunneling into state “4” and through resonant phonon emission into the collector state “5”.

The optical gain of this QCL was investigated by Jukam et al. using time domain spectroscopy in Ref. [Juk+09]. The experimental results and our calculation with the MSB method is shown in Fig. 9.6. The optical gain as function of the photon energy is plotted. We find an excellent agreement of the peak optical gain of 27 cm^{-1} compared to the experimental value of 25 cm^{-1}. Also, the energy of the emitted photons is nicely reproduced. We calculate the photon emission energy within the MSB method to be 11.8 meV whereas the experiment yields 12.5 meV.

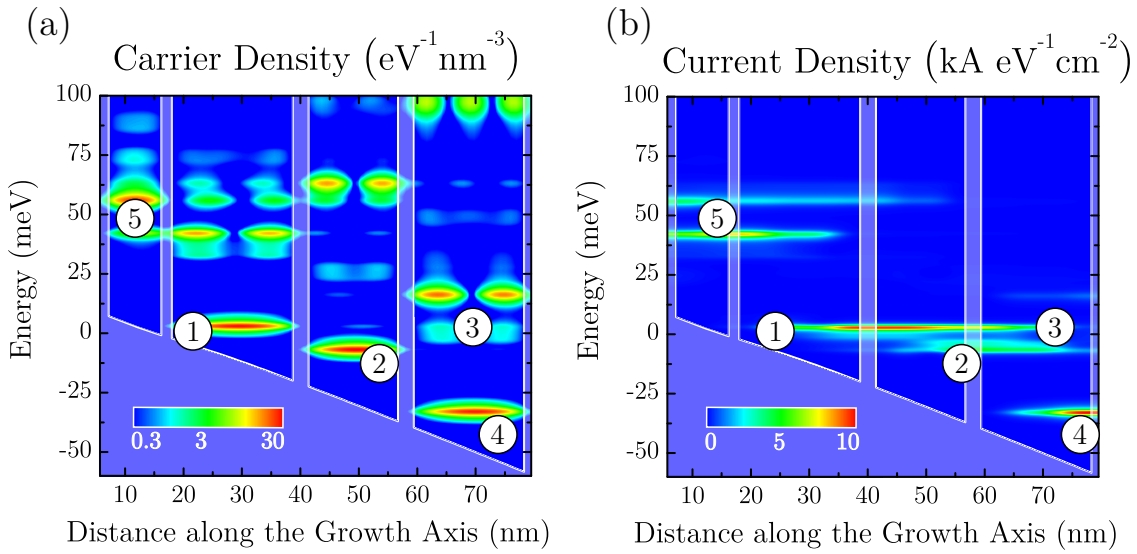

Figure 9.7: (a) Calculated conduction band profile (line) and contour plot of the energy and position resolved carrier density for the THz QCL described in Ref. [KMK10] at the threshold bias voltage of 68 mV per period and a lattice temperature of 100 K. (b) Calculated conduction band profile (line) and contour plot of the energy and position resolved current density. The shaded area indicates the conduction band profile.

9.2.2 *Calculation of an InGaAs/GaAsSb THz QCL*

In this section, we investigate the $In_{0.53}Ga_{0.47}As/GaAs_{0.51}Sb_{0.49}$ THz QCL design proposed in Ref. [KMK10] with a designed photon emission energy of $E_\gamma = 10$ meV. This material system was chosen since the optical gain is proportional to $(m^*)^{-3/2}$, where m^* is the effective electron mass [Ben+08]. Thus, material systems with low electron masses can enhance the laser performance [KMK10]. The calculated conduction band profile is shown in Fig. 9.7. The layer sequence for one period is **2.7**/9/**1.8**/20.7/**2.7**/15.3/**2.7**/18.9 nm, starting with the leftmost barrier. The $GaAs_{0.51}Sb_{0.49}$ barriers are shown in bold and the $In_{0.53}Ga_{0.47}As$ wells in normal font. Only the leftmost well is doped with 2.04×10^{16} cm^{-3}. This doped well contains the injector state that is labeled with "5" in Fig. 9.7. In Fig. 9.7 (a) the contour plot of the calculated position resolved carrier density as a function energy is shown. In Fig. 9.7 (b) the corresponding contour plot of the position resolved current density as a function of energy is shown. These figures illustrate the operation scheme and design improvements of this QCL. The upper laser state "1" is filled via indirect

pumping from the injector state “5”. Their energy difference is designed to be just the longitudinal optical (LO) phonon energy of about 34 meV. The laser transition from state “1” to “2” is diagonal and thus suppresses non-radiative transitions. Also, diagonal transitions are less sensitive to scattering at rough interfaces [Kub10; KMK10]. The carriers that did not undergo an optical transition within the active region can be extracted via state “3” and thermalized into state “4”. This is shown in Fig. 9.7 (b) where the energy and position resolved current density shows that the majority of carriers is resonantly thermalized from the states “1” and “3” into state “4”. The energy difference between state “3” and “4” is again designed to be the energy of an LO phonon. Finally, the collector state “4” coherently fills the injector state “5” of the next period. Thus, the threshold bias voltage per period is two times the LO phonon energy since the indirect pumping and the carrier thermalization are designed to completely thermalize each carrier in each period.

This QCL was designed using the fully self-consistent non-equilibrium Green’s function method including incoherent scattering of electrons on optical and acoustic phonons, charged impurities, rough interfaces, and random alloy disorder [KMK10]. However, the MSB method reproduces the major observable quantities very well, although, rough interfaces and alloy disorder are neglected. Therefore, it is possible to design a QCL with the MSB method. Since it is orders of magnitudes faster than a fully self-consistent NEGF calculation, it enables to efficiently and quickly sweep parameters to optimize the device design.

9.3 RESULTS FOR MID-INFRARED QC LASERS

Many important yet toxic gaseous molecular species have their spectral finger-print within the mid-infrared (MIR) spectral domain. Among these are organochlorides, organochlorines, nitrogen oxides, and most importantly carbon monoxide which is the most common cause of fatal air poisoning in many countries [Oma02]. Since a stable operation of MIR QC lasers at room temperature is possible no sophisticated cooling techniques are required and thus, those QC lasers find widespread applications as sensor and analyzer devices.

The fundamental difference of MIR QCL devices compared to THz QCL devices is the larger photon energy of about 150 meV. This implies that the applied bias voltage per period also increases to that order of magnitude. Hence, in a numerical calculation the energy domain has to be discretized with a respectively larger amount of nodes. Furthermore, typical MIR QCL designs consist of many thin barriers per period. This fact has to be addressed numerically with a higher spatial resolution compared to THz QCL calculations. Together, these numerical implications make

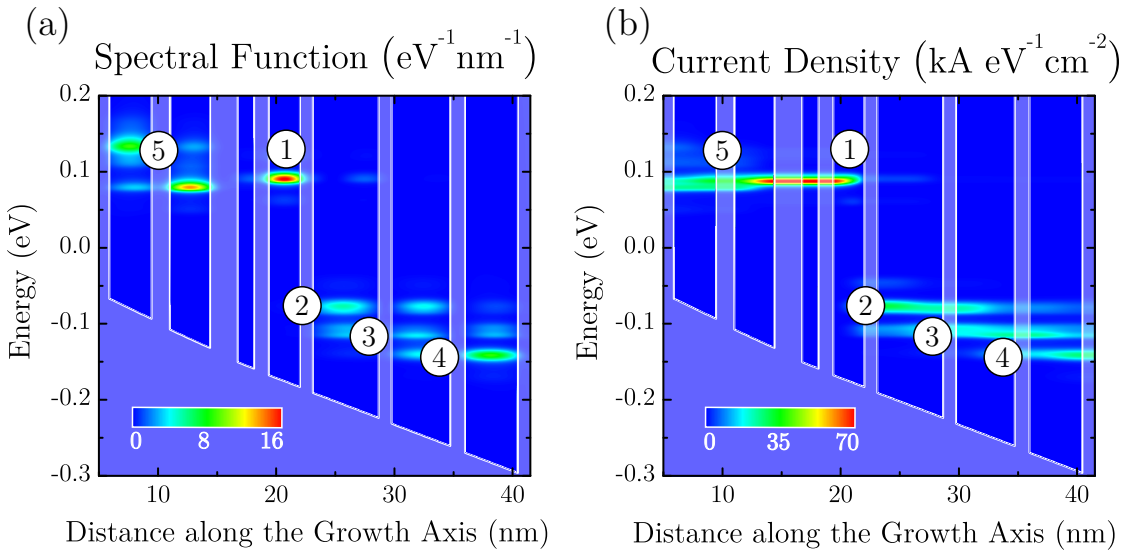

Figure 9.8: (a) Calculated conduction band profile (line) and contour plot of the energy and position resolved spectral function at vanishing in-plane momentum for the GaInAs/AlInAs mid-infrared QCL described in Ref. [Viz+09] at the threshold bias voltage of 237 mV per period and a lattice temperature of 300 K. (b) Calculated conduction band profile (line) and corresponding contour plot of the energy and position resolved current density.

it impossible to calculate MIR QCL devices within the fully self-consistent NEGF formalism even on our latest compute servers with 128 gigabytes of memory. However, our novel MSB method can calculate MIR QCL devices easily since it is very efficient in terms of computational costs.

In this section, we present the results of our novel MSB method for MIR QCL devices and compare these results with experimental data. First, we investigate the three-alloy-based short-injector MIR QCL described in Ref. [Viz+09]. This QCL is based on the strain-balanced AlInAs/GaInAs system. The calculated conduction band profile and the contour plots of the position and energy resolved spectral function and current density are shown in Fig. 9.8. The layer sequence is **1.4**/3.5/**1.6**/3.4/**0.6**/**0.45**/**1.2**/1.4/**1.3**/2.7/**1.05**/5.6/**1.1**/4.9/**1.3**/4.5 nm, starting with leftmost barrier in Fig. 9.8. The $Al_{0.635}In_{0.365}As$ barriers are shown in bold and the $Ga_{0.4}In_{0.6}As$ wells in normal font. The underlined layers are doped with 2×10^{17} cm^{-3} and the single AlAs barrier within the doped region has a width of 0.45 nm. This AlAs barrier improves the high temperature performance since it suppresses the leakage of carriers into the continuum. The optical transition is

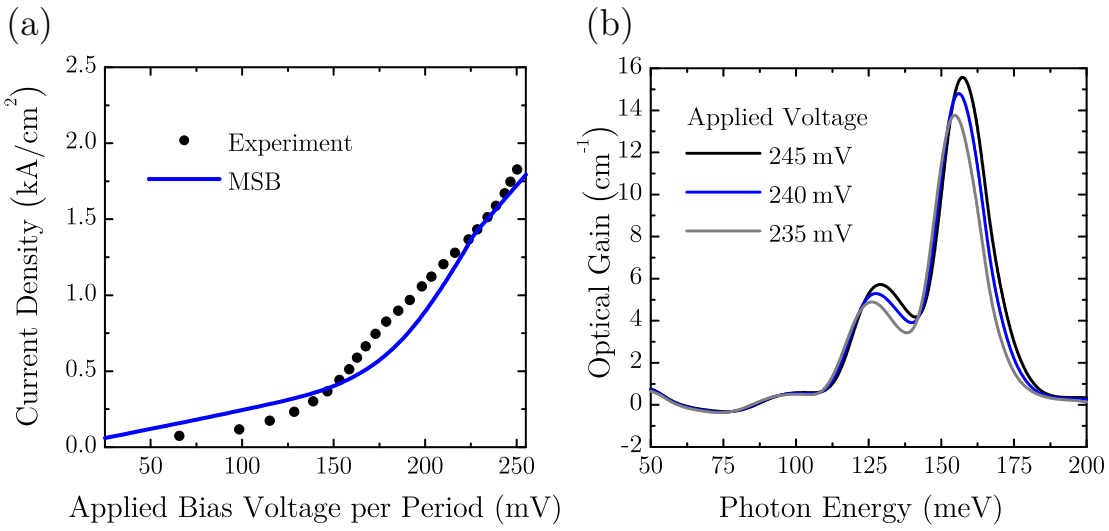

Figure 9.9: (a) Calculated DC current as a function of the applied bias voltage for the GaInAs/AlInAs MIR QCL described in Ref. [Viz+09] for a lattice temperature of 300 K. The solid blue line was calculated with our novel MSB method and the dotted line shows the experimental data. (b) Calculated optical gain as a function of the photon energy. The gain was calculated for various bias voltages near the threshold voltage. The threshold voltage can be estimated to be around 240 mV since the expected optical losses are 15.6 cm^{-1}. The experimental data for the threshold voltage is 237 mV.

slightly diagonal due to the 1.05 nm barrier inside the transition well which improves the carrier lifetime of the upper laser state. The emission wavelength of this MIR QCL is around 8.2 µm ($E_\gamma = 151$ meV). One period of this short-injector MIR QCL is only 36 nm whereas typical injector-based devices have period lengths of more than 50 nm.

The operation principle of this device is shown in Fig. 9.8 where the important states are labeled with numbers. The first layers of each period form a miniband that is labeled with “5” and “1”. It acts as injector state and upper laser state. The optical transition is between state “1” and the lower laser state labeled “2”. This lower laser level is efficiently emptied by an LO phonon cascade from state “2” to “3” and from state “3” to “4”. These three states form the ejector. The lowest state “4” resonantly fills the injector miniband “5” of the next period.

The threshold voltage, i. e. the applied bias voltage for which the optical gain compensates for all optical losses and thus, the QCL starts to emit photons, can be

estimated with Fig. 9.9 (b). This figure shows the optical gain as a function of the photon energy for various bias voltages. Note, that the calculations do not include interactions with the photon field. Thus, the calculated optical gain does not include any losses due to photon interactions nor any other losses like waveguide losses. The waveguide losses are assumed to be 15.6 cm^{-1} at 300 K [Viz+09]. Hence, for an applied bias voltage of 240 mV per period the calculated optical gain in Fig. 9.9 (b) exceeds the aforementioned losses. A further increase of the applied bias voltage beyond the threshold voltage leads to a further increase of the calculated optical gain. Therefore, we estimate the threshold voltage to be 240 mV. This is in agreement with the experimental value of 237 mV. Furthermore, Fig. 9.9 (b) shows the calculated peak gain for the threshold voltage at a photon energy of 155 meV and therefore, we estimate the emission wavelength to be 8.4 µm. This also nicely agrees with the experimental value of 8.2 µm ($E_\gamma = 151$ meV).

We also calculated the current–voltage characteristics for this MIR QCL. The calculated DC current as a function of the applied bias voltage per period is shown in Fig. 9.9 (a). The solid blue line was calculated with the MSB method and the dotted black line corresponds to the experimental data. The calculated current agrees very well with the experimental data, especially the range near the threshold voltage between 200 mV and 250 mV.

Next, we compare our calculated results obtained with the MSB method to the experimental data of the MIR QCL presented in Ref. [Fri+05]. This QCL is based on an injector-less design and employs the $Ga_{0.4}In_{0.6}As/Al_{0.56}In_{0.44}As$ material system. The calculated conduction band profile and the contour plot of the position and energy resolved spectral function is plotted in Fig. 9.10 (a). The layer sequence is **3.4**/3.2/**1.9**/2.6/**0.9**/5.2/**1.3**/4.0 nm, starting at the leftmost barrier. The $Al_{0.56}In_{0.44}As$ barriers are shown in bold and the $Ga_{0.4}In_{0.6}As$ wells in normal font. The underlined layers are doped with 1×10^{17} cm^{-3}.

The peculiarity of this device is that the energy of the emitted photons shifts according to the applied bias voltage [Fri+05]. For an applied field of 80 kV/cm the photon energy is 123 meV whereas for an applied field of 110 kV/cm the photon energy is 147 meV, i. e. two lasing frequencies.

The operation principle of this MIR QCL is shown in Fig. 9.10 (a) where the important states are labeled with numbers. The first two wells form the upper laser level that is labeled with “4” and “1”. The state labeled with “5” is about 80 meV above the upper laser level and is not occupied significantly and thus, it does not contribute to the current. The laser transition takes place between the states “1” and “2”. The lower laser level “2” is emptied via a resonant longitudinal optical (LO) phonon emission into state “3”. This ejector state “3” resonantly fills the upper laser

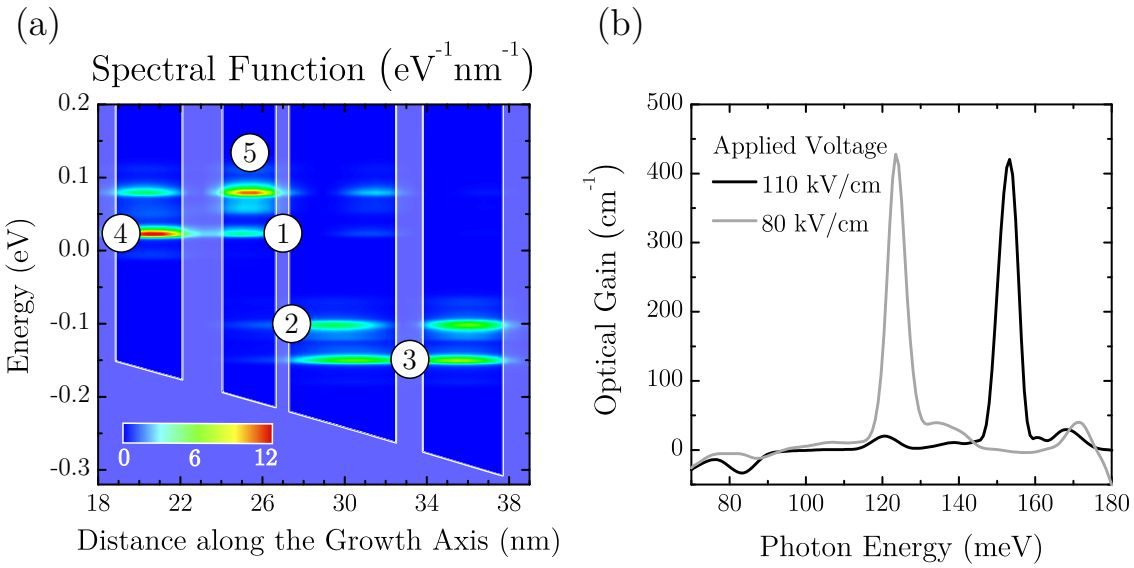

Figure 9.10: (a) Calculated conduction band profile (line) and contour plot of the energy and position resolved spectral function at vanishing in-plane momentum for the GaInAs/AlInAs MIR QCL described in Ref. [Fri+05] at the threshold bias voltage of 176 mV per period and a lattice temperature of 300 K. (b) Calculated optical gain as a function of the photon energy for the QCL structure described in Ref. [Fri+05]. The solid black line is calculated with the MSB method for an applied bias voltage of 176 mV whereas the solid gray line is calculated with the MSB method for an applied bias voltage of 242 mV. The experimentally observed photon energies are 123 mV and 151 mV, respectively.

level "4" of the next period.

In Fig. 9.10 (b) the calculated optical gain as a function of the photon energy is shown for two applied electric fields. These calculated gain spectra nicely agree with experimental data. The calculated photon emission energy for an applied electric field of 80 kV/cm is 122 meV whereas the experimental value is 123 meV. For an applied electric field of 110 kV/cm, we calculate the photon emission energy to be 153 meV which is in good agreement with corresponding experimental value of 147 meV.

In this section, we presented the calculated results for mid-infrared quantum cascade lasers obtained with the novel MSB method and compared them to experimental data. We showed that the MSB method is capable of accurately calculating the major observable quantities of MIR QC lasers. All results were calculated with the MSB method on a standard desktop computer with 2 gigabytes of computational memory.

This shows the computational efficiency of the novel MSB method. In contrast, a fully self-consistent NEGF calculation for the MIR QC lasers was not possible even on our most advanced compute server which is equipped with 128 gigabytes of memory.

9.4 PROPOSAL OF A NOVEL THZ QCL DESIGN

In this section, we propose a novel two-well injectorless THz quantum cascade laser design with a photon emission frequency of 2.85 THz which corresponds to a photon energy of $E_\gamma = 11.8\,\mathrm{meV}$. The design is based on the following principles. First, the device is based on the GaAs/AlGaAs material system. Although, devices based on InAs or AlSb intrinsically achieve better gain performances due to their lower effective masses [Ben+08], GaAs-based technology offers several advantages, e. g. the GaAs material system is well understood and mature processing technologies are available [SPB01; Gar+03]. Secondly, we use an injectorless design which has the advantage of high gain [Kat+10] since the device is shorter and the intermediate injector–collector states are neither needed to fill the upper laser states nor to empty the lower laser states. Thus, in an injectorless two-well QCL the active region extends over almost the whole period and consequently the ratio of gain to non-gain regions is much higher [Sca+10]. Thirdly, the design is based on narrow wells and barriers. This pushes the bound states to higher energies and thus, so-called parasitic leakage currents from one period to the next are suppressed. Additionally, we do not impose the restrictions of uniform barrier heights, i. e. we use different aluminum contents for the barriers. This additional degree of freedom for the QCL design can be used to improve temperature performance [Mat+12] and to find a design that is robust against fluctuations of material compositions. Finally, the design is based on the complete thermalization of carriers [KMK10]. Hence, for the energy balance of one period, the photon energy is neglected since only a minority of carriers emit a photon. Consequently, the majority of carriers is efficiently thermalized and non-periodic effects are remedied [Kub+09; KV09].

Our concrete suggestion of a novel THz quantum cascade laser consists of GaAs wells and alternating $Al_{0.10}Ga_{0.90}As$ and $Al_{0.26}Ga_{0.73}As$ barriers. Thus, the concrete barrier heights for our calculation are 107 meV and 237 meV. The layer sequence for one period is **2.1**/<u>7.35</u>/**2.1**/7.35 nm, starting with the lower $Al_{0.10}Ga_{0.90}As$ barrier. The AlGaAs barriers are shown in bold and the GaAs wells in normal font. Only the underlined layer of each period is doped with $3 \times 10^{16}\ \mathrm{cm}^{-3}$. The widths of the layers and the heights of the barriers and thus, the alloy compositions were optimized with a genetic algorithm based on the MSB method. Since the MSB method is very efficient in terms of computational memory and time, various alloy concentrations,

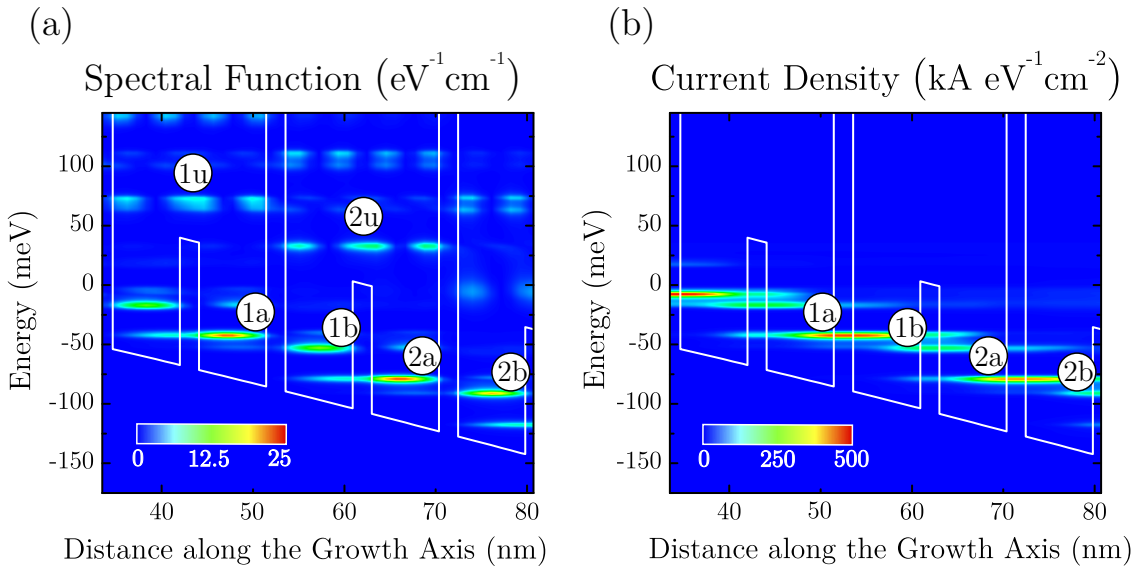

Figure 9.11: (a) Calculated conduction band profile (line) and contour plot of the energy and position resolved spectral function at vanishing in-plane momentum for the suggested QCL at the threshold bias voltage of 36 mV per period and a lattice temperature of 100 K. (b) Corresponding contour plot of the energy and position resolved current density.

barrier thicknesses, and further parameters can be calculated in parallel and an optimal QCL layout can be found quickly.

The operation scheme of this QCL is shown in Fig. 9.11 and Fig. 9.12 (a). In principle, this QCL design consists of alternating upper and lower laser states only. The upper laser states are labeled “1a” and “2a” in Fig. 9.11 and are located in the wells labeled “A” in Fig. 9.12 (a). From this upper laser level a photon transition into the states “1b” and “2b”, respectively, is possible. This laser transition between these states is diagonal and thus suppresses non-radiative transitions. However, the majority of carriers will be efficiently thermalized from state “1a” into the upper laser state “2a” of the next period because their energy difference is designed to be the energy of a longitudinal optical (LO) phonon. For the GaAs material system, the energy of an LO phonon is assumed to be $E_{\mathrm{OP}} \approx 34$ meV and thus, the threshold voltage of our novel QCL design is expected to be slightly below 34 mV where the states are aligned correctly for the LO phonon cascade.

The effects of the narrow wells and high barriers are also shown in Fig. 9.11. The upper states labeled “1u” and “2u” are pushed about 175 meV away from the

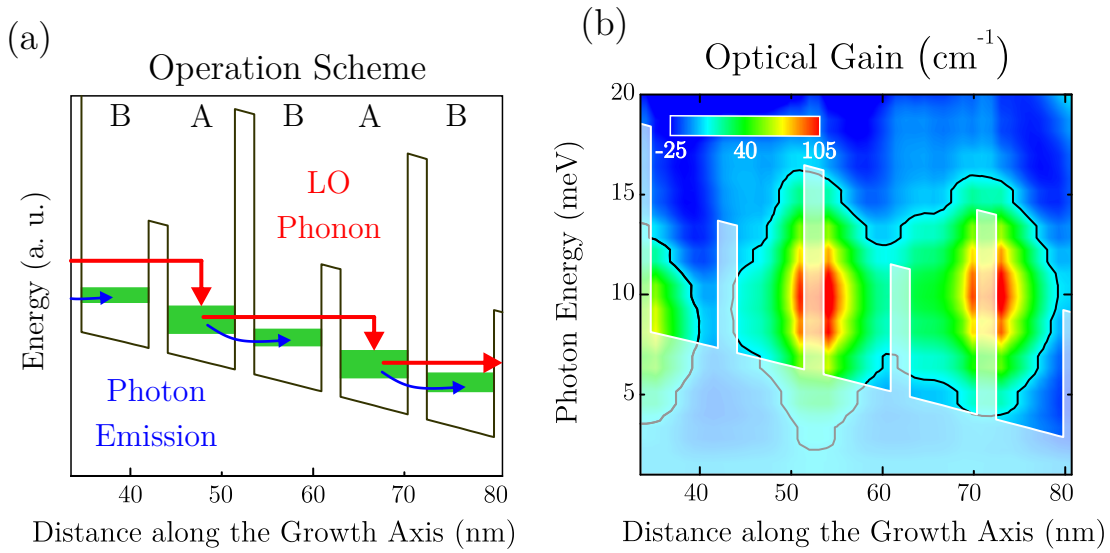

Figure 9.12: (a) Operation scheme of the novel QCL design. The red arrows indicate LO phonon emissions and the blue arrows indicate photon emissions. The two wells are labeled with "A" and "B" and only well "A" is doped. (b) Calculated contour plot of the position resolved optical gain as a function of the photon energy. The black solid contour line encloses the area of positive optical gain. The white solid line indicates the conduction band profile and is only meant to guide the eye. The applied bias voltage is 36 mV and the temperature is 100 K.

conduction band edge. Thus, they do not interact and interfere with other states of previous periods. Consequently, they do not carry any significant current, as shown in Fig. 9.11 (b).

We also calculated the position resolved optical gain as a function of the photon energy which is shown in Fig. 9.12 (b). Here, the black solid line encloses the area where the optical gain is positive. We find that almost the complete period contributes to the optical gain. The calculated optical gain as a function of the lattice temperature is shown in Fig. 9.13 (a). The corresponding calculated optical gain as a function of the photon energy is plotted for various temperatures in Fig. 9.13 (b). We find significantly higher optical gain than for the four-well QCL published in Ref. [KMK10]. Furthermore, we calculate gain even up to temperatures of 250 K which would be a new temperature record for THz QC lasers. In experiments, efficient cooling down to 230 K can be achieved easily with simple Peltier coolers in contrast to more sophisticated and more expensive cooling mechanisms which are required for

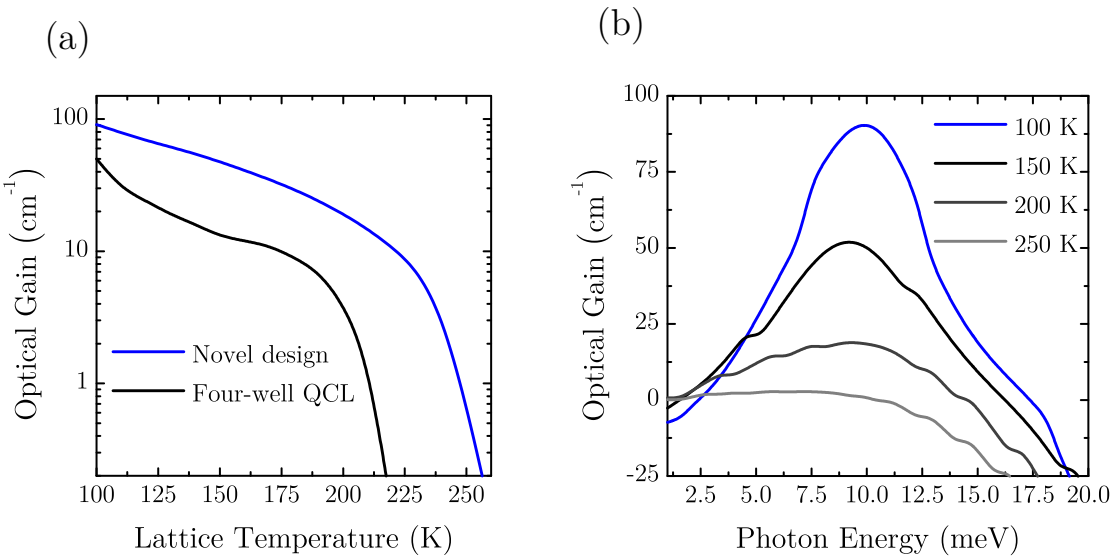

Figure 9.13: (a) Calculated optical gain as a function of the lattice temperature. The solid black line was calculated for the QCL proposed in Ref. [KMK10] whereas the solid blue line is calculated for the novel QCL design. (b) Calculated optical gain as a function of the photon energy for the novel QCL design for various temperatures.

lower temperatures [Ael+03; Bel+09]. The present temperature performance record of 199.5 K is achieved by a resonant phonon based three-well design [Fat+12].

Finally, we also calculated the DC current as a function of the applied bias voltage for our proposed QCL design. The current–voltage characteristics are plotted in Fig. 9.14. We calculated I-V curves for various temperatures from 100 K to 250 K. Our calculations do not show any negative differential resistance below the threshold voltage. This indicates an electrically stable operation of our novel QCL design. Note that usually a negative differential resistance can be observed above the threshold voltage in NEGF as well as in MSB calculations. This is caused by state misalignment and originates mainly from the fact that the coupling of the photon field is not included within the calculations.

In conclusion, we presented a novel concrete THz QCL design based on a two-well design with alternating barrier heights. The threshold voltage is designed to match the energy of an LO phonon and thus, complete carrier thermalization is achieved for the majority of the carriers within each period. We predict THz laser operation for temperatures up to 250 K.

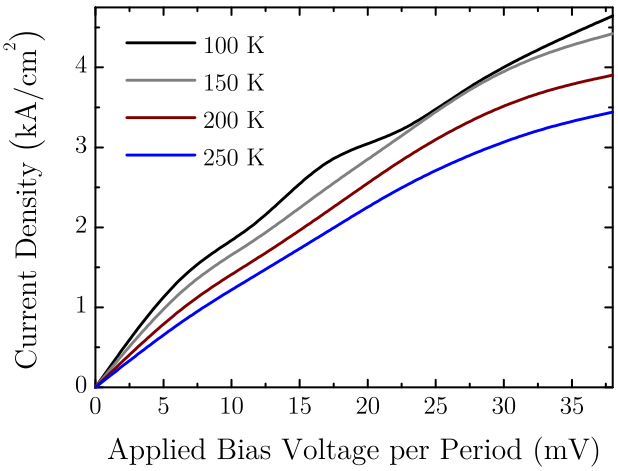

Figure 9.14: Calculated DC current as a function of the applied bias voltage for the novel QCL design for various temperatures. The current–voltage characteristics do not show any negative differential resistance and thus, indicate an electrically stable design.

10 SUMMARY AND ACHIEVEMENTS

In this thesis we presented a novel method based on the non-equilibrium Green's function (NEGF) formalism for the calculation of inelastic electron transport in semiconductor nanostructures. We applied the novel MSB method to quantum cascade laser (QCL) structures and we found very good consistency between the calculated results and the experimental data. Finally, we used the MSB method within a genetic algorithm to find an optimized high temperature THz QCL design. Our concrete proposal of a novel THz QCL design yields a calculated optical gain up to temperatures of 250 K which would be a new record within the THz domain.

We presented in detail the fundamentals of the non-equilibrium Green's function (NEGF) formalism for quantum transport calculations. The NEGF method is especially well suited to capture all relevant effects ranging from incoherent relaxation processes to quantum interference. However, a numerical implementation of the NEGF method for quantum transport calculations is complex, mathematically tough, and still highly challenging for modern computer hardware. On the other hand, the so-called Büttiker–Probe model is a numerically simple approach that is based on phenomenological scattering parameters. Hence, we developed the MSB method as a novel quantum transport approach that combines the rigorous implementation of scattering effects of the NEGF formalism with the numerical ease of the Büttiker–Probe model. We also developed approximations to the scattering self-energies to take full advantage of the low numerical demand of the Büttiker–Probe model especially for layered heterostructures. Furthermore, we simplified the solution of the Büttiker–Probes within the MSB method for devices that comprise only two current-carrying contacts. For such devices, we reduced the numerical effort to the solution of one linear system of equations instead of a nonlinear system of equations of the same size. Finally, we integrated the MSB method into a predictor–corrector approach to efficiently solve Poisson's equations along with the quantum transport equations.

During the work on this thesis, a software calculation package was developed within the framework of the next**nano** software suite. In particular, a very flexible,

high performance, multi-purpose input file reader was developed. It is capable of reading the extensive, well-kept next**nano** material database as well as a freely designable input file format based on the XML standard. The MSB algorithms were implemented with the high-level programming language C# that is part of the .NET Framework 4.0 from Microsoft. Most numerical tasks such as matrix multiplications were transferred to the Math Kernel Library (MKL) from Intel.

Part IV

APPENDIX

A

FOURIER TRANSFORMATIONS

In this chapter we briefly review the Fourier transformation that is useful to study spatially homogenous systems and to rewrite differential equations into algebraic equations. We assume a periodic function f with

$$f(\mathbf{r}) = f(\mathbf{r} + \mathbf{L} \cdot \mathbf{n}),$$

where $\mathbf{L} = (L_x, L_y, L_z)^T$ is the extent of a rectangular box and $\mathbf{n} = (n_x, n_y, n_z)^T$ with $n_i = 0, \pm 1, \pm 2, \ldots$ is the index of a box, where $i \in \{x, y, z\}$. The Fourier theorem states that f can be written as Fourier series that reads

$$f(\mathbf{r}) = \frac{1}{V} \sum_{\mathbf{k}} f(\mathbf{k})\, e^{i\mathbf{kr}},$$

where $\mathbf{k} = (k_x, k_y, k_z)^T$ with $k_i = 2\pi \frac{n_i}{L_i}$ with $i \in \{x, y, z\}$, $V = L_x L_y L_z$ is the volume of a periodic cell, and the Fourier components $f(\mathbf{k})$ read

$$f(\mathbf{k}) = \int_V \mathrm{d}\mathbf{r}\, f(\mathbf{r})\, e^{-i\mathbf{kr}}.$$

With the following two very useful identities it is straightforward to show that the Fourier transformation from $\mathbf{r}$ to $\mathbf{k}$ and back yields the original function

$$\int_V \mathrm{d}\mathbf{r}\, e^{i\mathbf{kr}} = V\, \delta(\mathbf{k}), \qquad \frac{1}{V} \sum_{\mathbf{k}} e^{i\mathbf{kr}} = \delta(\mathbf{r}). \tag{A.1}$$

The variable $\mathbf{k}$ becomes quasi-continuous if we consider an infinitely large volume V. Thus, the sum over $\mathbf{k}$ can be converted into an integral and the Fourier transformation reads

$$f(\mathbf{r}) = \frac{1}{V} \sum_{\mathbf{k}} f(\mathbf{k})\, e^{i\mathbf{kr}} \to \frac{1}{V} \frac{V}{(2\pi)^3} \int \mathrm{d}\mathbf{k}\, f(\mathbf{k})\, e^{i\mathbf{kr}} = \frac{1}{(2\pi)^3} \int \mathrm{d}\mathbf{k}\, f(\mathbf{k})\, e^{i\mathbf{kr}}.$$

Now, the identities from Eq. (A.1) read

$$\int\limits_V \mathrm{d}\mathbf{r}\, e^{i\mathbf{k}\mathbf{r}} = (2\pi)^3\, \delta(\mathbf{k}), \qquad \frac{1}{(2\pi)^3} \int \mathrm{d}\mathbf{k}\, e^{i\mathbf{k}\mathbf{r}} = \delta(\mathbf{r}).$$

For a translationally invariant system any observable $f(\mathbf{r}, \mathbf{r}')$ of two spatial coordinates depends only on the spatial difference coordinate $\mathbf{r} - \mathbf{r}'$. For such a system it is straightforward to show that the Fourier components $f(\mathbf{k}, \mathbf{k}')$ are proportional to $\delta(\mathbf{k} + \mathbf{k}')$

$$f(\mathbf{r}, \mathbf{r}') \equiv f(\mathbf{r} - \mathbf{r}') \qquad \Longleftrightarrow \qquad f(\mathbf{k}, \mathbf{k}') \propto \delta(\mathbf{k} + \mathbf{k}').$$

B

ANALYTIC K-SPACE INTEGRATION

In this chapter, we give a detailed derivation of the analytic k-space integration. This technique is used to calculate observables within the MSB method for layered heterostructures.

For heterostructures consisting of homogeneous layers any Green's function depends despite of the spatial coordinates on the energy E and the absolute value $k_\parallel$ of the momentum perpendicular to the propagation direction. In the following, we omit the spatial coordinates to keep the notation clean and compact. In general, the energy integrated quantity I can be calculated from the energy resolved Green's function $G(E, k_\parallel)$ as follows

$$\begin{aligned} I &= \frac{1}{2\pi} \int_0^\infty \mathrm{d}E \int_0^E \mathrm{d}\mathbf{k}_\parallel \, f(E)\, G(E, k_\parallel) \\ &= \frac{1}{2\pi} \int_0^\infty \mathrm{d}E \int_0^E 2\pi k_\parallel \mathrm{d}k_\parallel \, f(E)\, G(E, k_\parallel), \end{aligned} \tag{B.1}$$

where f is the distribution function. Note that the structure of Eq. (B.1) is equivalent to e. g. the calculation of the energy and momentum integrated carrier density in Eq. (5.10) and current density in Eq. (5.12).

The total energy E consists of the energy E_z along the direction of propagation and energy $E(k_\parallel)$ within a layer

$$E = E_z + E(k_\parallel) = E_z + \frac{\hbar^2 k_\parallel^2}{2m^*},$$

where m^* is the effective mass. Thus, we can transform the $k_\parallel$ integral into a E_z integral and express $k_\parallel$ and $\mathrm{d}k_\parallel$ as follows

$$k_\parallel = \sqrt{\frac{2m^*(E - E_z)}{\hbar^2}} \;\Leftrightarrow\; \mathrm{d}k_\parallel = -\sqrt{\frac{m^*}{2(E - E_z)}} \frac{\mathrm{d}E_z}{\hbar}. \tag{B.2}$$

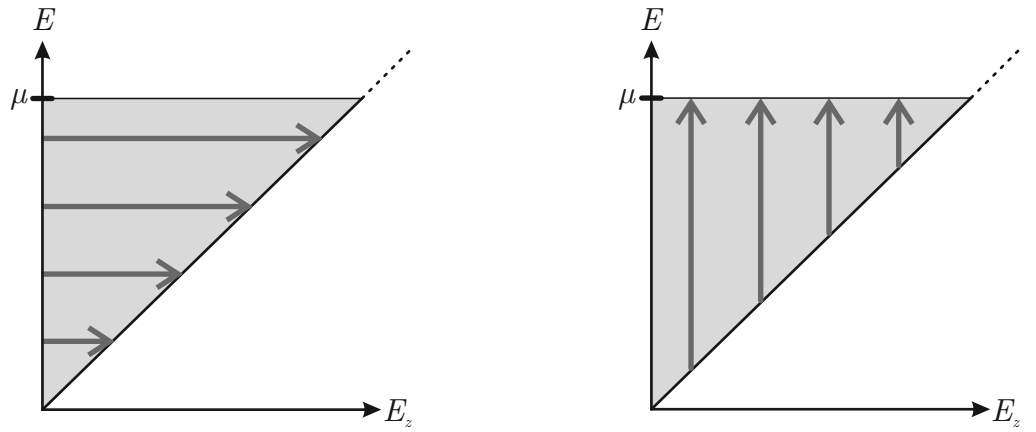

(a) Integral $\int_0^\infty \mathrm{d}E \int_0^E \mathrm{d}E_z\, f(E)\, G(E_z)$. (b) Integral $\int_0^\infty \mathrm{d}E_z\, G(E_z) \int_{E_z}^\infty \mathrm{d}E\, f(E)$.

Figure B.1: (a) Schematic drawing of the energy integration of the variable E and E_z. The gray shaded area corresponds to the integration domain for the zero temperature distribution function $f(E) = \Theta(E - \mu)$. (b) Since the distribution function $f(E) \to 0$ for $E \to \infty$ also for finite temperatures, we can reorder the integrals and analytically evaluate $\mathcal{F}_0(E_z) = \int_{E_z}^\infty \mathrm{d}E\, f(E)$.

Now, the crucial step is that the Green's function G for layered heterostructures within the MSB method does not independently depend on E and $k_\parallel$ but only on their difference, as discussed in Chapter 7.4

$$G(E, k_\parallel) \equiv G\Big(E - E(k_\parallel)\Big) \equiv G(E_z).$$

thus, the energy integrated quantity I can be expressed as follows

$$\begin{aligned} I &= \frac{m^*}{2\pi\hbar^2} \int_0^\infty \mathrm{d}E \int_0^E \mathrm{d}E_z\, f(E)\, G(E_z) \\ &= \frac{m^*}{2\pi\hbar^2} \int_0^\infty \mathrm{d}E_z\, G(E_z) \int_{E_z}^\infty \mathrm{d}E\, f(E), \end{aligned} \tag{B.3}$$

where in the last step the integration sequence was reordered and the resulting factor of minus one from Eq. (B.2) was merged with the limits of the E_z integral, as shown in Fig. B.1.

Finally, we can evaluate the E integral in Eq. (B.3) analytically since the distribution function goes to zero for large energies and thus the E integral is finite. We introduce the incomplete Fermi–Dirac integral of order j as follows

$$\mathcal{F}_j(x,b) = \frac{1}{\Gamma(j+1)} \int_b^\infty \mathrm{d}t \, \frac{t^j}{\exp(t-x)+1},$$

where Γ is the so-called gamma function. The Fermi distribution requires the incomplete zero-order Fermi–Dirac integral for which the following closed form exists

$$\begin{aligned}\mathcal{F}_0(\mu, E_z) &= \frac{1}{\Gamma(1)} \int_{E_z}^\infty \frac{\mathrm{d}t}{\exp\left(\frac{t-\mu}{k_B T}\right)+1} \\ &= k_B T \, \ln\left(\exp\left(\frac{\mu - E_z}{k_B T}\right)+1\right),\end{aligned}$$

where $\Gamma(1) = 1$, μ is the chemical potential, k_B is Boltzmann's constant, and T is the temperature.

Altogether, the energy integrated quantity I can be calculated from the Green's function G within the MSB method for layered heterostructures as follows

$$I = \frac{m^*}{2\pi\hbar^2} \int_0^\infty \mathrm{d}E_z \, \mathcal{F}_0(\mu, E_z) \, G(E_z).$$

IDIOTICON

In this chapter we present a brief overview and summary of common concepts and techniques in the field of non-equilibrium Green's functions and quantum transport calculations.

Born Approximation This perturbation method is used in scattering theory to find an approximated solution. The first-order Born approximation contains already an infinite series of Feynman's graphs or diagrams. Within the self-consistent Born approximation a certain class of Feynman'S diagrams for the self-energies is used. Thus, Dyson's equation becomes a nonlinear functional of the Green's function and requires a self-consistent solution. The selection of certain classes of Feynman's diagrams implies the summation of some classes up to infinite order whereas other classes are included within a lower order and some classes are even neglected. However, it is not straightforward to choose the subsets for each order.

Dyson's Equation Dyson's equation is a particularly compact way to summarize the Feynman–Dyson perturbation theory. With Wick's theorem the exact Green's function G can be written as a non-interacting or free one-particle Green's function G_0 and perturbations due to self-energies Σ as follows

$$G(\mathbf{1},\mathbf{2}) = G_0(\mathbf{1},\mathbf{2}) + \int \mathrm{d}\mathbf{1}' \int \mathrm{d}\mathbf{2}'\, G_0(\mathbf{1},\mathbf{1}')\Sigma(\mathbf{1}',\mathbf{2}')G(\mathbf{2}',\mathbf{2}),$$

where the abbreviations from Chapter 1 are used. This definition of the Green's function G is exactly the same as given in Eq. (1.4) since the non-interacting Green's function G_0 is defined as

$$\left(i\hbar\frac{\mathrm{d}}{\mathrm{d}t_1} - H_0(\mathbf{r}_1)\right) G_0(\mathbf{1},\mathbf{1}') = \delta(\mathbf{1}\mathbf{1}').$$

Feynman's Rules By means of Wick's theorem the exact Green's function can be evaluated through a perturbation expansion. Richard P. Feynman introduced

the idea of representing different contributions obtained from Wick's decomposition by diagrams. They are very useful to get insight into the physical processes that are described by the individual terms. Thus, Feynman's graphs or diagrams are an illustrative method to solve many-particle problems and the perturbation expansion of Green's functions.

Fluctuation–Dissipation Theorem The fluctuation-dissipation theorem can be derived from statistical thermodynamics in a general way. It relates the fluctuations in a system at thermal equilibrium to the response of the system to perturbations. Within the non-equilibrium Green's function formalism the fluctuation–dissipation theorem connects the state occupation and thus the fluctuations to the spectral function which give the retarded correlations and response function.

Hartree Potential Carrier–carrier interactions induce an infinite hierarchy of Green's functions. The first term of this series is called Hartree term. It is instantaneous and can be written as the so-called Hartree potential that is the solution of Poisson's equation. A detailed description is given in Sec. 1.9.1 and Chapter 3.

Keldysh–Contour The Keldysh–contour is used for the perturbation expansion of the time-ordered Green's functions. Within the interaction representation the unitary operator for the time evolution between times t_0 and t involves the integration along the Keldysh–contour from an arbitrary reference time t_0 to time t and back to time t_0. The initial time t_0 has to be chosen earlier than any interaction time. Neglecting any initial correlations, the reference time t_0 can be set to $t_0 = -\infty$.

Keldysh's Equation Keldysh's equation is obtained by applying Langreth's theorem to Dyson's equation. The result for a system that was in a non-interacting state in the infinite past is

$$G^<(\mathbf{1},\mathbf{1}') = \int \mathrm{d}\mathbf{2} \int \mathrm{d}\mathbf{3}\, G^R(\mathbf{1},\mathbf{2})\, \Sigma^<(\mathbf{2},\mathbf{3})\, G^A(\mathbf{3},\mathbf{1}'),$$

which is equivalent to Keldysh's original result [HJ89]. A detailed derivation is given in Sec. 1.3.

Landauer Formula The Landauer formula is a general approach to near-equilibrium transport. It relates the conductance of a system at zero temperature to the quantum mechanical transmission coefficients and has become the standard

theoretical model by which the results of experiments on e. g. ballistic magneto-transport are interpreted. A generalization of this approach is the so-called Landauer–Büttiker formalism. It describes current transport in finite systems and an arbitrary number of contacts.

Langreth's Theorem Langreth's theorem provides rules to handle products of two or more piecewise defined Green's functions. The rules for convolutions of Green's functions A, B, and C read

$$\begin{aligned} D = \int A\,B \qquad & D^R = \int A^R\,B^R \\ & D^{\lessgtr} = \int \left(A^R\,B^{\lessgtr} + A^{\lessgtr}B^A\right) \\ D = \int A\,B\,C \qquad & D^R = \int A^R\,B^R\,C^R \\ & D^{\lessgtr} = \int \left(A^R\,B^R\,C^{\lessgtr} + A^R\,B^{\lessgtr}C^A + A^{\lessgtr}\,B^A\,C^A\right), \end{aligned}$$

where the left-hand side is formally defined on the a contour whereas the right-hand side corresponds to the piecewise defined Green's function formalism.

Linear Response Linear response theory is a first order perturbation theory. The basic idea of linear response theory is that the response to a weak, external perturbation is proportional to the perturbation itself. Thus, only the proportionality factor has to be investigated.

Predictor–Corrector Scheme The predictor–corrector scheme is a general method to enhance the convergence of the iterative solution of coupled equations. Predictor–corrector methods use an extrapolation of previous iteration steps (the predictor step) to calculate a new solution (the corrector step). Within the non-equilibrium Green's function formalism this technique can be used to improve the convergence of the coupled system of Poisson's equation and the quantum transport equations. A detailed description of the predictor–corrector scheme for quantum transport calculations is given in Chapter 3.

Wick's Decomposition This is also called Wick's theorem. It states that higher order Green's functions can be factorized into single-particle Green's functions for quadratic Hamiltonians [BF04]. Thus, many-particle Green's functions can be effectively reduced to products of single-particle Green's functions. For instance this property can be used to introduce the self-energies in Eq. (1.4).

BIBLIOGRAPHY

[AG98] M. P. Anantram and T. R. Govindan. *Conductance of carbon nanotubes with disorder: A numerical study*. Phys. Rev. B **58**, 8 (1998), pp. 4882–4887 (cit. on pp. 21, 57).

[Ael+03] T. Aellen, S. Blaser, M. Beck, D. Hofstetter, J. Faist, and E. Gini. *Continuous-wave distributed-feedback quantum-cascade lasers on a Peltier cooler*. Applied Physics Letters **83**, 10 (2003), pp. 1929–1931 (cit. on p. 116).

[And04] T. Andlauer. *Discretization of multiband-$k\cdot p$-Schrödinger equations for multidimensional semiconductor nanostructures*. Technische Universität München, 2004 (cit. on pp. 33, 34).

[And09] T. Andlauer. *Optoelectronic and spin-related properties of semiconductor nanostructures in magnetic fields*. Walter Schottky Insitut, 2009 (cit. on p. 33).

[Asa08] Y. Asai. *Nonequilibrium phonon effects on transport properties through atomic and molecular bridge junctions*. Phys. Rev. B **78**, 4 (2008), p. 045434 (cit. on p. 42).

[BF04] H. Bruus and K. Flensberg. *Many-Body Quantum Theory in Condensed Matter Physics*. Oxford University Press, 2004 (cit. on pp. 21, 131).

[BK95] R. Binder and S. Koch. *Nonequilibrium semiconductor dynamics*. Progress in Quantum Electronics **19**, 4-5 (1995), pp. 307–462 (cit. on pp. 15, 21, 25, 41).

[BS50] J. Bardeen and W. Shockley. *Deformation Potentials and Mobilities in Non-Polar Crystals*. Phys. Rev. **80**, 1 (1950), pp. 72–80 (cit. on p. 44).

[Beh+08] B. N. Behnken, G. Karunasiri, D. R. Chamberlin, P. R. Robrish, and J. Faist. *Real-time imaging using a 2.8 THz quantum cascade laser and uncooled infrared microbolometer camera*. Opt. Lett. **33**, 5 (2008), pp. 440–442 (cit. on p. 100).

[Bel+09] M. Belkin, Q. J. Wang, C. Pflugl, A. Belyanin, S. Khanna, A. Davies, E. Linfield, and F. Capasso. *High-Temperature Operation of Terahertz Quantum Cascade Laser Sources*. Selected Topics in Quantum Electronics, IEEE Journal of **15**, 3 (2009), pp. 952 –967 (cit. on p. 116).

[Ben+07] A. Benz, G. Fasching, A. M. Andrews, M. Martl, K. Unterrainer, T. Roch, W. Schrenk, S. Golka, and G. Strasser. *Influence of doping on the performance of terahertz quantum-cascade lasers*. Appl. Phys. Lett. **90**, 10 (2007), p. 101107 (cit. on pp. 99–105).

[Ben+08] E. Benveniste, A. Vasanelli, A. Delteil, J. Devenson, R. Teissier, A. Baranov, A. M. Andrews, G. Strasser, I. Sagnes, and C. Sirtori. *Influence of the material parameters on quantum cascade devices*. Applied Physics Letters **93**, 13 (2008), p. 131108 (cit. on pp. 107, 113).

[Bir+07] S. Birner, T. Zibold, T. Andlauer, T. Kubis, M. Sabathil, A. Trellakis, and P. Vogl. *nextnano: General Purpose 3-D Simulations*. IEEE Transactions on Electron Devices **54**, 9 (2007), pp. 2137–2142 (cit. on p. 74).

[Bir+09] S. Birner, C. Schindler, P. Greck, M. Sabathil, and P. Vogl. *Ballistic quantum transport using the contact block reduction (CBR) method*. Journal of Computational Electronics **8**, 3–4 (2009), pp. 267–286 (cit. on pp. 21, 63).

[Bir11] S. Birner. *Modeling of semiconductor nanostructures and semiconductor–electrolyte interfaces*. Selected Topics of Semiconductor Physics and Technology, Vol. 135. Walter Schottky Insitut, 2011 (cit. on p. 53).

[Bur92] M. G. Burt. *The justification for applying the effective-mass approximation to microstructures*. Journal of Physics: Condensed Matter **4**, 32 (1992), p. 6651 (cit. on p. 46).

[Büt86a] M. Büttiker. *Four-Terminal Phase-Coherent Conductance*. Phys. Rev. Lett. **57**, 14 (1986), pp. 1761–1764 (cit. on p. 62).

[Büt86b] M. Büttiker. *Role of quantum coherence in series resistors*. Phys. Rev. B **33**, 5 (1986), pp. 3020–3026 (cit. on p. 61).

[Büt88a] M. Büttiker. *Coherent and sequential tunneling in series barriers*. IBM J. Res. Develop. **32**, 1 (1988), pp. 63–75 (cit. on p. 61).

[Büt88b] M. Büttiker. *Symmetry of electrical conductance*. IBM J. Res. Develop. **32**, 3 (1988), pp. 317–334 (cit. on pp. 15, 62).

[Cau+11] S. Cauley, M. Luisier, V. Balakrishnan, G. Klimeck, and C.-K. Koh. *Distributed non-equilibrium Green's function algorithms for the simulation of nanoelectronic devices with scattering*. J. Appl. Phys. **110**, 4 (2011), p. 043713 (cit. on pp. 15, 57).

[DCVP94] A. Di Carlo, P. Vogl, and W. Pötz. *Theory of Zener tunneling and Wannier-Stark states in semiconductors*. Phys. Rev. B **50**, 12 (1994), pp. 8358–8377 (cit. on p. 64).

[DWS79] K. S. Dy, S.-Y. Wu, and T. Spratlin. *Exact solution for the resolvent matrix of a generalized tridiagonal Hamiltonian*. Phys. Rev. B **20**, 10 (1979), pp. 4237–4243 (cit. on p. 49).

[Dan84] P. Danielewicz. *Quantum theory of nonequilibrium processes, I*. Annals of Physics **152**, 2 (1984), pp. 239–304 (cit. on pp. 15, 21, 22, 25, 27, 29, 30, 40).

[Dat00] S. Datta. *Nanoscale device modeling: the Green's function method*. Superlattice. Microst. **28**, 4 (2000), pp. 253–278 (cit. on p. 61).

[Dat05] S. Datta. *Quantum Transport: Atom to Transistor*. Cambridge University Press, 2005 (cit. on p. 63).

[Dat95] S. Datta. *Electronic Transport in Mesoscopic Systems*. Ed. by H. Ahmed, M. Pepper, and A. Broers. Cambridge Studies in Semiconductor Physics and Microelectronic Engineering 3. Cambridge University Press, 1995 (cit. on pp. 21, 30, 36, 37, 47, 57, 62–65).

[ET70] L. Esaki and R. Tsu. *Superlattice and Negative Differential Conductivity in Semiconductors*. IBM Journal of Research and Development **14**, 1 (1970), pp. 61–65 (cit. on p. 97).

[Eiß12] T. Eißfeller. *Theory of the Electronic Structure of Quantum Dots in External Fields*. PhD thesis. Technische Universität München, 2012 (cit. on p. 34).

[FJ92] D. K. Ferry and C. Jacoboni. *Quantum Transport in Semiconductors*. New York: Plenum Press, 1992 (cit. on pp. 21, 22, 36, 57).

[FW71] A. L. . Fetter and J. D. Walecka. *Quantum Theory of Many-Particle Systems*. McGraw-Hill, New York, 1971 (cit. on pp. 25, 42).

[Fai+94] J. Faist, F. Capasso, D. L. Sivco, C. Sirtori, A. L. Hutchinson, and A. Y. Cho. *Quantum Cascade Laser*. Science **264**, 5158 (1994), pp. 553–556 (cit. on p. 97).

[Fat+12] S. Fathololoumi, E. Dupont, C. Chan, Z. Wasilewski, S. Laframboise, D. Ban, A. Mátyás, C. Jirauschek, Q. Hu, and H. C. Liu. *Terahertz quantum cascade lasers operating up to ∼ 200 K with optimized oscillator strength and improved injection tunneling*. Opt. Express **20**, 4 (2012), pp. 3866–3876 (cit. on p. 116).

[Fre10] M. Frey. *Scattering in Nanoscale Devices*. Ed. by W. Fichtner, Q. Huang, H. Jäckel, G. Tröster, and B. Witzigmann. Vol. 211. Series in Microelectronics. Hartung-Gorre Verlag Konstanz, 2010 (cit. on p. 43).

[Fre90] W. R. Frensley. *Boundary conditions for open quantum systems driven far from equilibrium*. Rev. Mod. Phys. **62**, 3 (1990), pp. 745–791 (cit. on p. 73).

[Fri+05] A. Friedrich, G. Boehm, M. C. Amann, and G. Scarpa. *Quantum-cascade lasers without injector regions operating above room temperature*. Applied Physics Letters **86**, 16 (2005), p. 161114 (cit. on pp. 111, 112).

[Frö54] H. Fröhlich. *Electrons in lattice Fields*. Adv. Phys. **3** (1954), pp. 325–361 (cit. on p. 43).

[GBK08] X. Gao, D. Botez, and I. Knezevic. *Phonon confinement and electron transport in GaAs-based quantum cascade structures*. Journal of Applied Physics **103**, 7 (2008), p. 073101 (cit. on p. 44).

[GL88] S. M. Goodnick and P. Lugli. *Effect of electron-electron scattering on nonequilibrium transport in quantum-well systems*. Phys. Rev. B **37**, 5 (1988), pp. 2578–2588 (cit. on p. 86).

[GS04] A. Gehring and S. Selberherr. *Evolution of Current Transport Models for Engineering Applications*. Journal of Computational Electronics **3**, 3 (2004), pp. 149–155 (cit. on pp. 73, 75).

[Gar+03] M. Garcia, E. Normand, C. Stanley, C. Ironside, C. Farmer, G. Duxbury, and N. Langford. *An AlGaAs-GaAs quantum cascade laser operating with a thermoelectric cooler for spectroscopy of NH3*. Optics Communications **226**, 1–6 (2003), pp. 39–43 (cit. on p. 113).

[Gma+01] C. Gmachl, F. Capasso, D. L. Sivco, and A. Y. Cho. *Recent progress in quantum cascade lasers and applications*. Reports on Progress in Physics **64**, 11 (2001), p. 1533 (cit. on p. 97).

[Gre08] P. Greck. *Dissipative Quantum Transport in Semiconductor Nanostructures*. Walter-Schottky-Institut, 2008 (cit. on p. 49).

[HJ89] H. Haug and A.-P. Jauho. *Quantum Kinetics in Transport and Optics of Semiconductors*. Springer Berlin, 1989 (cit. on pp. 21, 22, 28, 130).

[Hal75] A. G. Hall. *Non-equilibrium Green functions: generalized Wick's theorem and diagrammatic perturbation with initial correlations*. Journal of Physics A: Mathematical and General **8**, 2 (1975), p. 214 (cit. on p. 26).

[IMO07] H. Iwata, T. Matsuda, and T. Ohzone. *Computationally efficient method for scattering device simulation in nanoscale MOSFETs*. Solid-State Electronics **51**, 5 (2007), pp. 708 –713 (cit. on p. 61).

[JH92] C. Johnson and P. Hansbo. *Adaptive finite element methods in computational mechanics*. Computer Methods in Applied Mechanics and Engineering **101** (1992), pp. 143–181 (cit. on p. 34).

[JL89] C. Jacoboni and P. Lugli. *The Monte Carlo Method for Semiconductor Device Simulations*. Springe, Wien, 1989 (cit. on p. 44).

[JPM06] S. Jin, Y. J. Park, and H. S. Min. *A three-dimensional simulation of quantum transport in silicon nanowire transistor in the presence of electron-phonon interactions*. Journal of Applied Physics **99**, 12 (2006), p. 123719 (cit. on p. 80).

[JR83] C. Jacoboni and L. Reggiani. *The Monte Carlo method for the solution of charge transport in semiconductors with applications to covalent materials*. Rev. Mod. Phys. **55**, 3 (1983), pp. 645–705 (cit. on p. 45).

[Jac98] J. D. Jackson. *Classical Electrodynamics*. 3rd ed. Wiley, New York, 1998 (cit. on p. 38).

[Juk+09] N. Jukam, S. S. Dhillon, D. Oustinov, J. Madeo, J. Tignon, R. Colombelli, P. Dean, M. Salih, S. P. Khanna, E. H. Linfield, and A. G. Davies. *Terahertz time domain spectroscopy of phonon-depopulation based quantum cascade lasers*. Applied Physics Letters **94**, 25 (2009), p. 251108 (cit. on pp. 100, 104–106).

[KB62] L. P. Kadanoff and G. A. Baym. *Quantum Statistical Mechanics*. Ed. by D. Pines. W. A. Benjamin, Inc., 1962 (cit. on pp. 21, 36, 37, 40).

[KMK10] T. Kubis, S. R. Mehrotra, and G. Klimeck. *Design concepts of terahertz quantum cascade lasers: Proposal for terahertz laser efficiency improvements*. Appl. Phys. Lett. **97**, 26 (2010), p. 261106 (cit. on pp. 100, 107, 108, 113, 115, 116).

[KS71] R. F. Kazarinov and R. A. Suris. *Possibility of the amplification of electromagnetic waves in a semiconductor with a superlattice*. Sov. Phys. Semicond. **5**, 4 (1971), pp. 707–709 (cit. on p. 97).

[KT82] Y. A. Kukharenkov and S. G. Tikhodeev. *A Diagram Technique in the Theory of Relaxation Processes*. Soviet Phys. JETP **56**, 4 (1982), pp. 831–838 (cit. on p. 26).

[KV09] T. Kubis and P. Vogl. *Predictive quantum theory of current and optical emission in quantum cascade lasers*. *Novel In-Plane Semiconductor Lasers VIII*. Ed. by A. A. Belyanin and P. M. Smowton. Vol. 7230. 1. San Jose, CA, USA: SPIE, 2009, p. 723019 (cit. on p. 113).

[KV11] T. Kubis and P. Vogl. *Assessment of approximations in nonequilibrium Green's function theory*. Phys. Rev. B **83**, 19 (2011), p. 195304 (cit. on pp. 15, 37, 57, 59).

[Kat+10] S. Katz, A. Vizbaras, G. Boehm, and M.-C. Amann. *Nonlinear gain behavior in injectorless quantum cascade lasers*. Optical Engineering **49**, 11 (2010), p. 111107 (cit. on p. 113).

[Kel65] L. V. Keldysh. *Diagram technique for non-equilibrium processes*. Sov. Phys. JETP **20** (1965), pp. 1018–1026 (cit. on pp. 21, 26).

[Kub+09] T. Kubis, C. Yeh, P. Vogl, A. Benz, G. Fasching, and C. Deutsch. *Theory of nonequilibrium quantum transport and energy dissipation in terahertz quantum cascade lasers*. Phys. Rev. B **79**, 19 (2009), p. 195323 (cit. on pp. 15, 21, 57, 113).

[Kub10] T. C. Kubis. *Quantum transport in semiconductor nanostructures*. Selected Topics of Semiconductor Physics and Technology, Vol. 114. Walter Schottky Insitut, 2010 (cit. on pp. 35, 37, 40–45, 57, 75, 79, 86, 93, 101, 102, 104, 108).

[Kum+11] S. Kumar, C. W. I. Chan, Q. Hu, and J. L. Reno. *A 1.8-THz quantum cascade laser operating significantly above the temperature of $\hbar\omega/k_B$*. Nat. Phys. **7**, 3 (2011), pp. 166–171 (cit. on p. 100).

[LD12] S. Li and E. Darve. *Extension and optimization of the FIND algorithm: Computing Green's and less-than Green's functions*. Journal of Computational Physics **231**, 4 (2012), pp. 1121–1139 (cit. on p. 82).

[LD92] R. Lake and S. Datta. *Nonequilibrium Green's function method applied to double-barrier resonant-tunneling diodes*. Phys. Rev. B **45**, 12 (1992), pp. 6670–6685 (cit. on pp. 42, 43, 79).

[LJ81a] D. H. Lee and J. D. Joannopoulos. *Simple scheme for surface-band calculations. I*. Phys. Rev. B **23**, 10 (1981), pp. 4988–4996 (cit. on p. 49).

[LJ81b] D. H. Lee and J. D. Joannopoulos. *Simple scheme for surface-band calculations. II. The Green's function*. Phys. Rev. B **23**, 10 (1981), pp. 4997–5004 (cit. on p. 49).

[LK55] J. M. Luttinger and W. Kohn. *Motion of Electrons and Holes in Perturbed Periodic Fields*. Phys. Rev. **97**, 4 (1955), pp. 869–883 (cit. on p. 46).

[LK90] C. S. Lent and D. J. Kirkner. *The quantum transmitting boundary method*. Journal of Applied Physics **67**, 10 (1990), pp. 6353–6359 (cit. on pp. 73, 74).

[LW02] S.-C. Lee and A. Wacker. *Nonequilibrium Green's function theory for transport and gain properties of quantum cascade structures*. Phys. Rev. B **66**, 24 (2002), p. 245314 (cit. on pp. 43, 79, 86).

[Lak+97] R. Lake, G. Klimeck, R. C. Bowen, and D. Jovanovic. *Single and multiband modeling of quantum electron transport through layered semiconductor devices*. J. Appl. Phys. **81**, 12 (1997), pp. 7845–7869 (cit. on pp. 21, 44, 45, 54, 57).

[Lan+10] N. Lang, J. Röpcke, S. Wege, and A. Steinbach. *In situ diagnostic of etch plasmas for process control using quantum cascade laser absorption spectroscopy*. The European Physical Journal - Applied Physics **49**, 01 (2010), pp. 13110–13113 (cit. on p. 97).

[Lan88] R. Landauer. *Spatial variation of currents and fields due to localized scatterers in metallic conduction*. IBM J. Res. Develop. **32** (1988), p. 306 (cit. on p. 62).

[Lan92] R. Landauer. *Conductance from transmission: common sense points*. Phys. Scr. **T42** (1992), p. 110 (cit. on p. 62).

[Laz+05] M. Lazzeri, S. Piscanec, F. Mauri, A. C. Ferrari, and J. Robertson. *Electron Transport and Hot Phonons in Carbon Nanotubes*. Phys. Rev. Lett. **95**, 23 (2005), p. 236802 (cit. on p. 42).

[Lee+06] S.-C. Lee, F. Banit, M. Woerner, and A. Wacker. *Quantum mechanical wavepacket transport in quantum cascade laser structures*. Phys. Rev. B **73**, 24 (2006), p. 245320 (cit. on pp. 32, 34).

[Li+08] S. Li, S. Ahmed, G. Klimeck, and E. Darve. *Computing entries of the inverse of a sparse matrix using the FIND algorithm*. J. Comput. Phys. **227**, 22 (2008), pp. 9408–9427 (cit. on p. 82).

[Lug+87] P. Lugli, C. Jacoboni, L. Reggiani, and P. Kocevar. *Monte Carlo algorithm for hot phonons in polar semiconductors*. Applied Physics Letters **50**, 18 (1987), pp. 1251–1253 (cit. on p. 42).

[Lui07] M. Luisier. *Quantum Transport Beyond the Effective Mass Approxirnation*. PhD thesis. Swiss Federal Insitute of Technology ZÃŒrich, 2007 (cit. on pp. 22, 28, 30, 41).

[MA89] N. Mori and T. Ando. *Electron–optical-phonon interaction in single and double heterostructures*. Phys. Rev. B **40**, 9 (1989), pp. 6175–6188 (cit. on p. 44).

[MMV04] D. Mamaluy, A. Mannargudi, and D. Vasileska. *Electron Density Calculation Using the Contact Block Reduction Method*. Journal of Computational Electronics **3**, 1 (2004), pp. 45–50 (cit. on p. 62).

[MSV03] D. Mamaluy, M. Sabathil, and P. Vogl. *Efficient method for the calculation of ballistic quantum transport*. J. Appl. Phys. **93**, 8 (2003), pp. 4628–4633 (cit. on p. 62).

[Mah90] G. D. . Mahan. *Many-Particle Physics*. Plenium, New York, 1990 (cit. on pp. 25, 38, 41–43).

[Mam+05] D. Mamaluy, D. Vasileska, M. Sabathil, T. Zibold, and P. Vogl. *Contact block reduction method for ballistic transport and carrier densities of open nanostructures*. Phys. Rev. B **71**, 24 (2005), p. 245321 (cit. on pp. 15, 62).

[Mar+07] A. Martinez, M. Bescond, J. Barker, A. Svizhenko, M. Anantram, C. Millar, and A. Asenov. *A Self-Consistent Full 3-D Real-Space NEGF Simulator for Studying Nonperturbative Effects in Nano-MOSFETs*. Electron Devices, IEEE Transactions on **54**, 9 (2007), pp. 2213 –2222 (cit. on p. 21).

[Mat+12] A. Matyas, R. Chashmahcharagh, I. Kovacs, P. Lugli, K. Vijayraghavan, M. A. Belkin, and C. Jirauschek. *Improved terahertz quantum cascade laser with variable height barriers*. Journal of Applied Physics **111**, 10 (2012), p. 103106 (cit. on p. 113).

[Mat67] R. D. Mattuck. *A Guide to Feynmann Diagrams in the Many-Body Problem*. McGraw-Hill, New York, 1967 (cit. on pp. 25, 41).

[Oma02] S. T. Omaye. *Metabolic modulation of carbon monoxide toxicity*. Toxicology **180**, 2 (2002), pp. 139 –150 (cit. on p. 108).

[Pou07] M. Pourfath. *Numerical Study of Quantum Transport in Carbon Nanotube Based Transistors*. PhD thesis. Technischen Universität Wien, Fakultät für Elektrotechnik und Informationstechnik, 2007 (cit. on p. 42).

[Pre89] P. M. Prenter. *Splines and Variational Methods*. John Wiley & Sons, 1989 (cit. on p. 34).

[Pul80] P. Pulay. *Convergence acceleration of iterative sequences. the case of scf iteration*. Chemical Physics Letters **73**, 2 (1980), pp. 393–398 (cit. on p. 54).

[RSE04] B. K. Ridley, W. J. Schaff, and L. F. Eastman. *Hot-phonon-induced velocity saturation in GaN*. Journal of Applied Physics **96**, 3 (2004), pp. 1499–1502 (cit. on p. 42).

[Ren+03] Z. Ren, R. Venugopal, S. Goasguen, S. Datta, and M. Lundstrom. *nanoMOS 2.5: A two-dimensional simulator for quantum transport in double-gate MOSFETs*. Electron Devices, IEEE Transactions on **50**, 9 (2003), pp. 1914–1925 (cit. on p. 61).

[Rid82] B. K. Ridley. *Quantum Processes in Semiconductors*. Oxford Science Publications, 1982 (cit. on pp. 43, 45).

[SC83] J. N. Schulman and Y.-C. Chang. *Reduced Hamiltonian method for solving the tight-binding model of interfaces*. Phys. Rev. B **27**, 4 (1983), pp. 2346–2354 (cit. on p. 73).

[SG69] D. Scharfetter and H. Gummel. *Large-signal analysis of a silicon Read diode oscillator*. Electron Devices, IEEE Transactions on **16**, 1 (1969), pp. 64 –77 (cit. on p. 73).

[SPB01] C. Sirtori, H. Page, and C. Becker. *GaAs-based quantum cascade lasers*. Philosophical Transactions of the Royal Society of London. Series A: Mathematical, Physical and Engineering Sciences **359**, 1780 (2001), pp. 505–522 (cit. on p. 113).

[SSR84] M. P. L. Sancho, J. M. L. Sancho, and J. Rubio. *Quick iterative scheme for the calculation of transfer matrices: Application to Mo (100)*. J. Phys. F: Met. Phys. **14**, 5 (1984), p. 1205 (cit. on pp. 49, 50).

[SSR85] M. P. L. Sancho, J. M. L. Sancho, and J. Rubio. *Highly convergent schemes for the calculation of bulk and surface Green functions*. J. Phys. F: Met. Phys. **15**, 4 (1985), p. 851 (cit. on pp. 49, 50).

[SW02] W. Schäfer and M. Wegener. *Semiconductor Optics and Transport Phenomena*. Springer, Berlin, 2002 (cit. on p. 42).

[Sab+02] M. Sabathil, S. Hackenbuchner, J. Majewski, G. Zandler, and P. Vogl. *Towards Fully Quantum Mechanical 3D Device Simulations*. Journal of Computational Electronics **1**, 1 (2002). 10.1023/A:1020719928653, pp. 81–85 (cit. on p. 73).

[Sca+10] G. Scalari, M. I. Amanti, C. Walther, R. Terazzi, M. Beck, and J. Faist. *Broadband THz lasing from a photon-phonon quantum cascade structure*. Opt. Express **18**, 8 (2010), pp. 8043–8052 (cit. on p. 113).

[Sch61] J. Schwinger. *Brownian Motion of a Quantum Oscillator*. J. Math. Phys. **2**, 3 (1961), pp. 407–432 (cit. on p. 21).

[Seg84] L. J. Segerlind. *Applied Finite Element Analysis*. John Wiley & Sons, Inc., 1984 (cit. on p. 34).

[TYM92] D. Z. Y. Ting, E. T. Yu, and T. C. McGill. *Multiband treatment of quantum transport in interband tunnel devices*. Phys. Rev. B **45**, 7 (1992), pp. 3583–3592 (cit. on p. 73).

[Thy06] K. S. Thygesen. *Electron transport through an interacting region: The case of a nonorthogonal basis set*. Phys. Rev. B **73**, 3 (2006), p. 035309 (cit. on p. 31).

[Tre+06] A. Trellakis, T. Zibold, T. Andlauer, S. Birner, R. Smith, R. Morschl, and P. Vogl. *The 3D nanometer device project <i>nextnano</i> : Concepts, methods, results*. Journal of Computational Electronics **5**, 4 (2006). 10.1007/s10825-006-0005-x, pp. 285–289 (cit. on pp. 73, 74).

[Tre+97] A. Trellakis, A. T. Galick, A. Pacelli, and U. Ravaioli. *Iteration scheme for the solution of the two-dimensional Schrödinger-Poisson equations in quantum structures*. Journal of Applied Physics **81**, 12 (1997), pp. 7880–7884 (cit. on p. 54).

[Ven+02] R. Venugopal, Z. Ren, S. Datta, M. S. Lundstrom, and D. Jovanovic. *Simulating quantum transport in nanoscale transistors: Real versus mode-space approaches*. Journal of Applied Physics **92**, 7 (2002), pp. 3730–3739 (cit. on pp. 49, 61).

[Ven+03] R. Venugopal, M. Paulsson, S. Goasguen, S. Datta, and M. S. Lundstrom. *A simple quantum mechanical treatment of scattering in nanoscale transistors*. J. Appl. Phys. **93**, 9 (2003), pp. 5613–5625 (cit. on pp. 61, 85).

[Vit+05] M. S. Vitiello, G. Scamarcio, V. Spagnolo, B. S. Williams, S. Kumar, Q. Hu, and J. L. Reno. *Measurement of subband electronic temperatures and population inversion in THz quantum-cascade lasers*. Applied Physics Letters **86**, 11 (2005), p. 111115 (cit. on p. 42).

[Viz+09] A. Vizbaras, S. Katz, G. Boehm, and M.-C. Amann. *Short-Injector Quantum Cascade Laser Emitting at 8-μm Wavelength With High Slope Efficiency*. Photonics Technology Letters, IEEE **21**, 19 (2009), pp. 1384–1386 (cit. on pp. 109–111).

[Wac+99] A. Wacker, A.-P. Jauho, S. Rott, A. Markus, P. Binder, and G. H. Döhler. *Inelastic Quantum Transport in Superlattices: Success and Failure of the Boltzmann Equation*. Phys. Rev. Lett. **83**, 4 (1999), pp. 836–839 (cit. on p. 86).

[Wac02a] A. Wacker. *Gain in quantum cascade lasers and superlattices: A quantum transport theory*. Phys. Rev. B **66**, 8 (2002), p. 085326 (cit. on pp. 21, 38–40, 57, 86).

[Wac02b] A. Wacker. *Semiconductor superlattices: a model system for nonlinear transport*. Physics Reports **357**, 1 (2002), pp. 1–111 (cit. on pp. 34, 42).

[Wil+03] B. S. Williams, S. Kumar, H. Callebaut, Q. Hu, and J. L. Reno. *Terahertz quantum-cascade laser at lambda ≈ 100μm using metal waveguide for mode confinement*. Applied Physics Letters **83**, 11 (2003), pp. 2124–2126 (cit. on p. 42).

[YC01] P. Y. Yu and M. Cardona. *Fundamentals of Semiconductors*. Springer Berlin, 2001 (cit. on p. 33).

[YKD07] A. A. Yanik, G. Klimeck, and S. Datta. *Quantum transport with spin dephasing: A nonequlibrium Green's function approach*. Phys. Rev. B **76**, 4 (2007), p. 045213 (cit. on p. 80).

[Zah+04] F. Zahid, A. W. Ghosh, M. Paulsson, E. Polizzi, and S. Datta. *Charging-induced asymmetry in molecular conductors*. Phys. Rev. B **70**, 24 (2004), p. 245317 (cit. on p. 53).

[Zhe+06] X. Zheng, W. Chen, M. Stroscio, and L. F. Register. *Nonequillibrium Green's function analysis of interwell transport and scattering in monopolar lasers*. Phys. Rev. B **73**, 24 (2006), p. 245304 (cit. on pp. 15, 57).

[Zib07] T. Zibold. *Semiconductor based quantum information devices: Theory and simulations*. Selected Topics of Semiconductor Physics and Technology, Vol. 87. Walter Schottky Insitut, 2007 (cit. on p. 53).

DANKSAGUNG

An diese Stelle bedanke ich mich bei allen, die mich bei dieser Arbeit unterstützt haben. Zu aller erst gilt mein Dank Herrn Prof. Dr. Peter Vogl, der mir diese Doktorarbeit ermöglicht hat, für seine Betreuung und Förderung, sowie für die gewährte Freiheit bei der Interpretation des Themas.

Weiterhin gilt mein Dank meinem Kollegen Thomas Eißfeller, für das gute Arbeitsklima in unserem gemeinsamen Büro, sowie allen anderen Kollegen vom Lehrstuhl T33, namentlich Stefan Birner, Thomas Grange, Tillmann Kubis, Christoph Schindler und Reinhard Scholz für die gute Zusammenarbeit und die vielen fachlichen und persönlichen Diskussionen.

Insbesondere gilt mein Dank auch meinen Eltern, die mir meine Ausbildung ermöglicht haben und mich immer unterstützt haben.

Ganz besonderer Dank gilt auch meiner Frau Nadine, die mir immer den Rücken freigehalten hat, und meiner Tochter Gertrud, die immer für reichlich Abwechslung gesorgt hat.